The flow topology around anisotropic particles in planar shearing flows and Discretization of stochastic partial differential equations

Mahan Raj Banerjee

Engineering Mechanics Unit
Jawaharlal Nehru Centre for Advanced Scientific Research

This dissertation is submitted for the degree of
Doctor of Philosophy

JNCASR January 2021

I would like to dedicate this thesis to my family . . .

Certificate

It is certified that the work contained in the thesis entitled **"The flow topology around anisotropic particles in planar shearing flows and Discretization of stochastic partial differential equations"**, by **"Mahan Raj Banerjee"**, has been carried out for the partial fulfilment of his PhD under our supervision and that this work has not been submitted elsewhere for a degree.

Prof. Ganesh Subramanian

Prof. Santosh Ansumali
January 2021

Declaration

I hereby declare that except where specific reference is made to the work of others, the contents of this dissertation are original and have not been submitted in whole or in part for consideration for any other degree or qualification in this, or any other university. This dissertation is my own work and contains nothing which is the outcome of work done in collaboration with others, except as specified in the text and Acknowledgements.

Mahan Raj Banerjee
January 2021

Acknowledgements

Foremost, I wish to express my gratitude to my advisors Prof. Ganesh Subramanian and Prof. Santosh Ansumali for their continuous guidance and support.

I would like to thank all my collaborators Prof. Ronojoy Adhikari, Prof. Sauro Succi, Mr. Akshay Chandran and Ms. Rashmi Ramadugu. I would also like to thank other faculties of EMU, Prof K. R. Sreenivas, Prof Meheboob Alam and Prof Diwakar S. Venkatesan. I want to thank all my friends and colleagues in EMU/JNCASR for making my time at JNCASR a pleasant one. The financial support extended by Jawaharlal Nehru Centre for Advanced Scientific Research is also acknowledged.

Last but not the least I thank my wife Dr. Shazia Janwari and my parents for their support and encouragement.

Abstract

The flow topology around anisotropic particles in planar linear shearing flows

In the Stokesian limit, the streamline topology around a single neutrally buoyant sphere is identical to the topology of pair-sphere pathlines, both in an ambient simple shear flow. In both cases there are fore-aft symmetric open and closed trajectories spatially demarcated by an axisymmetric separatrix surface. This topology has crucial implications for both scalar transport from a single sphere, and for the rheology of a dilute suspension of spheres. The first part of the thesis examines the topology of the fluid pathlines around a neutrally buoyant freely rotating spheroid in simple shear flow, and shows it to be profoundly different from that for a sphere. This will have a crucial bearing on transport from such particles in shearing flows. To the extent that fluid pathlines in the single-spheroid problem and pair-trajectories in the two-spheroid problem, are expected to bear a qualitative resemblance to each other, the non-trivial trajectory topology identified here will also have significant consequences for the rheology of dilute suspensions of anisotropic particles.

An inertialess non-Brownian spheroid in a simple shear flow rotates indefinitely in any one of a one-parameter family of Jeffery orbits. The parameter is the orbit constant C, with $C = 0$ and $C = \infty$ denoting the limiting cases of a spinning(log-rolling) spheroid, and a spheroid tumbling in the flow-gradient plane, respectively. The streamline pattern around a spinning spheroid is qualitatively identical to that around a sphere regardless of its aspect ratio. For a spheroid in any orbit other than the spinning one ($C > 0$), the velocity field being time dependent in all such cases, the fluid pathlines may be divided into two categories. Pathlines in the first category extend from upstream to downstream infinity without ever crossing the flow axis; unlike the spinning case, these pathlines are fore-aft asymmetric, suffering a net displacement in both the gradient and vorticity directions. The second category includes primarily those pathlines that loop around the spheroid, and to a lesser extent those that cross the flow axis, without looping around the spheroid, reversing direction in the process. The residence time, in the neighbourhood of the spheroid, is a smooth function of upstream conditions for pathlines belonging to the first category. In sharp contrast, the number of loops, and thence the residence time associated with the pathlines in the second category, is extremely sensitive to upstream conditions. Plots of the residence time as a function of the upstream co-ordinates of these pathlines reveal a fractal structure with singularities distributed on a Cantor-like set, suggesting the existence of a chaotic saddle in the vicinity of the spheroid.

After establishing the pathline topology for simple shear, the first part ends with the implications of the findings for transport in disperse multiphase systems. There is also a brief description of the pathline topology for a neutrally buoyant spheroid in the more general one-parameter family of planar hyperbolic linear flows.

Discretization of stochastic partial differential equations

The dynamics of thermally fluctuating conserved order parameters are described by stochastic conservation laws. Thermal equilibrium in such systems requires the dissipative and stochastic components of the flux to be related by detailed balance. Preserving this relation in spatial and temporal discretization is necessary to obtain solutions that have fidelity to the continuum. Here, we propose a finite-difference discretization that preserves the detailed balance on the lattice, has a spatial error that is isotropic to leading order in lattice spacing, and can be integrated accurately in time using a delayed difference method. We benchmark the method for model B dynamics with a ϕ^4 Landau free energy and obtain excellent agreement with the analytical results. Here, we also present the idea of discrete lattice operators derived on a Body-Centered-Cubic(BCC) lattice, which preserve key properties of their analytical counterpart, such as isotropy and fundamental vector identities at the leading order due to the symmetries of the BCC lattice. These operators show quite a high degree of accuracy and isotropy as compared to those defined on a simple cubic(SC) lattice, while maintaining a relatively smaller stencil. To illustrate the usefulness of these schemes, we have considered a couple of examples, such as passive scalar transport and fluctuating hydrodynamics. We have also considered the flow over a circular cylinder at different Reynolds numbers to illustrate the effectiveness and the accuracy of the BCC grid and schemes in handling complex geometries in the flow field.

Table of contents

I The flow topology around anisotropic particles in planar shearing flows 1

II Discretization of stochastic partial differential equations 61

List of figures

List of tables

Part I

The flow topology around anisotropic particles in planar shearing flows

Chapter 1

Introduction

Characterizing the rheological behaviour of a dilute Stokesian suspension of hydrodynamically interacting particles requires the solution of the two-body problem at the microscale. Einstein(1906) first obtained the effective viscosity(μ_e) of a dilute suspension of non-interacting rigid spherical particles(the one-body problem) in terms of the viscosity of the suspending fluid(μ) as $\mu_e = \mu\left(1 + \frac{5}{2}\phi\right)$, ϕ being the volume fraction of the suspended spheres; the factor 5/2 is referred to as the Einstein coefficient. Much later, Batchelor and Green [13, 14] investigated the effect of pair-interactions between spherical particles, in an ambient linear flow, in an attempt to calculate the $O(\phi^2)$ correction to the effective viscosity. In obtaining this correction, they examined the pair-sphere pathlines in simple shear flow, and showed that these pathlines had the same character as the streamlines around a single sphere in a simple shear flow [27]. In both instances, the trajectories may be classified into two groups. The first group consists of fore-aft symmetric open trajectories that extend to upstream and downstream infinity. The second group consists of closed orbits around the test sphere. The two groups are demarcated by a separatrix surface consisting of open trajectories that asymptote to the flow axis infinitely far away in both the upstream and downstream directions. The surface itself is axisymmetric, the axis of symmetry being the gradient direction of the ambient simple shear. Both the fore-aft symmetry of open trajectories, and the existence of closed ones, arise from the reversibility of the Stokes equations. Closed streamlines in the single-sphere problem are known to profoundly affect heat and mass transfer, leading to diffusion-limited transport at large Peclet numbers [1, 102, 104, 58, 59]. Likewise, for the pair-sphere problem, Batchelor and Green [14] showed that the pair-distribution function is rendered indeterminate, in the region of closed pathlines, in the pure hydrodynamic limit. This in turn leads to an indeterminate $O(\phi^2)$ coefficient for the suspension stress in all linear flows with regions of closed pair-pathlines, simple shear flow being a special case [56].

Here, we analyze the fluid pathlines around a torque-free neutrally buoyant spheroid of an arbitrary aspect ratio (regarded as a canonical anisotropic particle) in simple shear flow. Keeping in mind the scenario for suspensions of spherical particles detailed above, we expect our findings to, on one hand, shed some light on the transport of heat or mass from a single spheroid immersed in a shearing flow. On the other hand, our findings will also be relevant to the nature of pair-spheroid interactions, and thence, to the pair-level microstructure of Stokesian suspensions of interacting anisotropic particles. In any event, analyzing the fluid motion around a single spheroid is a natural first step towards an understanding of the more complicated two-body problem. The results reported here suggest that the diffusion-limited scalar transport at $O(\phi)$, and the indeterminate rheology at $O(\phi^2)$, encountered for the case of spherical particles above, are both likely to be resolved, to a significant extent, by the effects of shape anisotropy.

We characterize the topology of the fluid pathlines around a single prolate or oblate spheroid in an ambient simple shear flow. The exact disturbance velocity field required for this purpose is available in closed form from earlier efforts [29, 30, 77] that have used a spheroidal harmonics formalism for this purpose. As is well known, a neutrally buoyant torque-free spheroid in simple shear rotates along Jeffery orbits, and the disturbance velocity field is therefore time dependent in all cases except when the spheroid axis is aligned with the ambient vorticity (the log-rolling or spinning mode). Our results show that the departure from sphericity has a profound effect on the nature of the fluid pathlines around a spheroid in a precessional (non-spinning) orbit. The obvious changes happen for the open pathlines which are still open, but unlike the case of a sphere, are no longer fore-aft symmetric. Such pathlines undergo a lateral displacement in both the gradient and vorticity directions as they proceed from upstream to downstream infinity. The unexpected aspect concerns the originally closed pathlines. A fraction of these pathlines opens up, but unlike the pathlines above, the resulting open pathlines do not head directly downstream. Instead, these pathlines loop around the rotating spheroid with the number of loops being extremely (indeed, infinitely) sensitive to the upstream coordinates of the particular pathline. The sensitivity with regard to the upstream coordinates has the signatures of chaotic scattering [15, 7–9, 6]. The presence of a chaotic saddle suggested by the aforementioned scattering pattern implies that both closed (periodic) and bounded pathlines continue to exist for a spheroid in a generic precessional orbit, but only constitute a set of vanishingly small measure, and one that is therefore numerically inaccessible.

The first part of this thesis is organized as follows. In the remainder of this chapter, we discuss the problem formulation. Calculation of the fluid pathlines requires an expression for the disturbance velocity field due to a torque-free spheroid in simple shear flow, and as mentioned above, this is obtained in terms of the appropriate vector spheroidal harmonics [61–63], after resolving the ambient simple shear into simpler canonical components in body-fixed coordinates [29, 30, 77]. In Chapter 2 we analyse the regular fluid pathlines for the spheroid in a simple shear flow. Section 2.1 presents the streamlines for the simpler steady case of a spinning spheroid. In this case, the topology of the streamline pattern is shown to be identical to that around a torque-free sphere and a circular cylinder [56, 108, 88], with fore-aft symmetric open and closed streamlines being demarcated by a (non-axisymmetric) separatrix surface. For a prolate spheroid, the streamline pattern (including the separatrix in particular) transitions from that for a sphere to a cylinder, with increasing spheroid aspect ratio. In section 2.2.1 we investigate the topology of the fluid pathlines for the general time dependent case of a spheroid in a general precessional orbit (with particular focus on the in-plane tumbling orbit); the focus here is on the regular open pathlines that do not loop around the spheroid, while heading from upstream to downstream infinity. Unlike both a sphere and a spinning spheroid, these pathlines are fore-aft asymmetric. This asymmetry is best characterized in terms of the net gradient and vorticity displacements suffered by the pathline [100]. The numerically determined displacements are then compared to the far-field analytical predictions, as a function of the upstream pathline coordinates, for the spheroid rotating over a range of Jeffery orbits. In Chapter 3 we analyze the second category of pathlines which includes the singular open pathlines that, although open, loop around the spheroid before heading off to downstream infinity. For this case, we first show that the number of loops around the spheroid, and therefore, the residence time of the pathline in a sufficiently large neighborhood of the spheroid, are sensitively dependent on the initial pathline coordinates(chosen to lie on the negative flow axis). Plots of the residence time reveal an extremely fine-scaled fractal-like structure, suggesting the existence of a chaotic saddle in the vicinity of

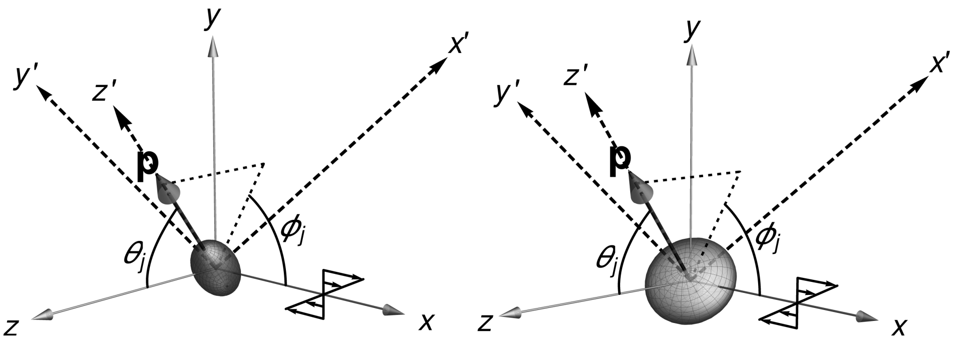

Fig. 1.1 A prolate and an oblate spheroid in simple shear flow. The primed(X', Y', Z') and unprimed (X, Y, Z) coordinates denote the body and the space fixed axes, respectively. θ_j and ϕ_j are polar and azimuthal Jeffery angles, respectively.

the spheroid. We examine the nature of this sensitive dependence as a function of the spheroid aspect ratio, and more importantly, as a function of the orbit constant for a given aspect ratio; the latter reveals the singular nature of the approach to the integrable limit ($C = 0$) of a log-rolling or a spinning spheroid. In section 3.2, we analyze the fluid pathlines from the chaotic scattering perspective that has been gainfully used in other scenarios [15, 41, 52, 6], by focussing on the nature of the pathlines as a function of their upstream coordinates. Herein, we examine the transition from regular to chaotic scattering with varying spheroid aspect ratio, and again, as a function of the Jeffery orbit constant. There exists a critical upstream offset corresponding to the onset of chaotic scattering, and for offsets less than this value, intervals of regular and chaotic scattering appear interlaced down to the smallest scales; the interlaced pattern is strongly dependent on aspect ratio. The extent of chaotic scattering is nevertheless shown to decrease for the largest aspect ratios, with the relevant signatures being eventually undetectable (numerically). We present the fractal nature of the stable and the unstable manifold of the chaotic saddle along with the uncertainty dimension plots for spheroids of varying aspect ratios, which shows the necessary power law scaling for the underlying saddle. We also examine the probability density of residence times, the emphasis being on the functional form of the tail, which are determined by the large residence times associated with the singular pathlines; rather unexpectedly, the tails appear to be algebraic, suggesting that the underlying (chaotic) invariant set has a non-hyperbolic character. Chapter 4 presents a summary of our findings, a discussion of the implications of these findings in the context of transport in multiphase systems, and expected nature of the fluid pathlines in a more general setting - the one-parameter family of hyperbolic linear flows.

1.1 Single spheroid in a simple shear flow

1.1.1 Jeffery orbits

The motion of spheroidal particles in linear flows in the absence of inertia is known since the work of [53]. A single torque-free spheroid rotates in any one of a single parameter family of closed trajectories now known as Jeffery orbits. The motion along a Jeffery orbit may be characterized in terms of the polar (θ_j) and azimuthal (ϕ_j) angles of the spheroid axis (see Figure 1.1), and these are given by the

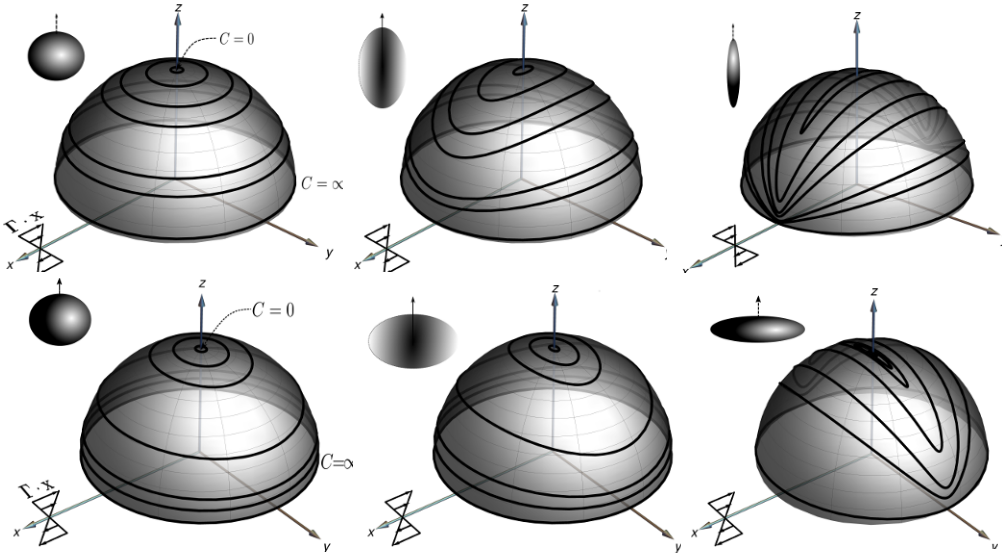

Fig. 1.2 Jeffery orbits for prolate(top)($\kappa = 1.25$, 2, 4) and oblate spheroids($\kappa = 0.8$, 0.5, 0.25)

following functions of time:

$$\phi_j = \cot^{-1}\left[\kappa \tan\left(\frac{\kappa\dot{\gamma}t}{1+\kappa^2}\right)\right], \ \theta_j = \tan^{-1}\left[\frac{C\kappa}{\sqrt{\kappa^2 \sin^2\phi_j + \cos^2\phi_j}}\right]. \tag{1.1}$$

Here, $\dot{\gamma}$ is the shear rate, κ is the spheroid aspect ratio and C is the orbit constant, ranging from 0 to ∞, that parameterizes the Jeffery orbits; $\kappa > 1 (< 1)$ for prolate(oblate) spheroids. The generic orbit is a spherical ellipse, with its major axis along the flow (gradient) direction for a prolate(an oblate) spheroid. The limiting cases $C = 0$ and $C = \infty$ correspond to a log-rolling motion of the prolate spheroid (spinning for the oblate one) about the vorticity axis, and a tumbling motion in the flow-gradient plane, respectively. The period of rotation is independent of C, being equal to $T_j = 2\pi/\dot{\gamma}(\kappa + \kappa^{-1})$. Figure 1.2 shows the Jeffery orbits for prolate and oblate spheroids of different aspect ratios. The eccentricity of the orbits can be seen to increase with increasing (decreasing) aspect ratio of the prolate (oblate) spheroid. For slender fibers ($\kappa = \infty$) and flat disks ($\kappa = 0$), the Jeffery orbits have a meridional character with the end points of the meridians, the poles, corresponding to the intersections of the flow and gradient axes with the unit sphere, respectively.

1.1.2 The spheroid velocity field in simple shear flow

The determination of the velocity field due to an inertialess torque-free spheroid in an ambient simple shear flow involves solving the Stokes equations in spheroidal coordinates [61–63]:

$$\mu\nabla^2\boldsymbol{u} = \boldsymbol{\nabla}p, \tag{1.2}$$

with the following boundary conditions in place

$$\boldsymbol{u}(\xi = \xi_0, \eta, \phi) = \boldsymbol{\omega} \times \boldsymbol{x} \quad \textit{and} \quad \boldsymbol{u}(\xi \to \infty, \eta, \phi) = \boldsymbol{\Gamma} \cdot \boldsymbol{x}. \tag{1.3}$$

Here, μ is the fluid viscosity, p is the hydrodynamic pressure, $\boldsymbol{x} \equiv (x, y, z)$ is the position vector, and $\boldsymbol{\Gamma}$ is the (transpose of the) velocity gradient tensor; $\boldsymbol{\Gamma} = \mathbf{1}_x \mathbf{1}_y$ in the space-fixed coordinate system (X, Y, Z) shown in Figure 1.1, with $\mathbf{1}_x$, $\mathbf{1}_y$ and $\mathbf{1}_z$ denoting the unit vectors along the flow, gradient and vorticity directions, respectively. The spheroid angular velocity, $\boldsymbol{\omega}$, in (1.3) is determined from a torque-free constraint. The component of $\boldsymbol{\omega}$ normal to the spheroid axis, is obtained from the Jeffery relations (1.1), while that along the axis is just half the projected ambient vorticity. In (1.2) and (1.3), (ξ, η, ϕ) are prolate spheroidal coordinates which, for a prolate spheroid, are related to the Cartesian ones as: $x' = d\bar{\xi}\bar{\eta}\cos\phi$, $y' = d\bar{\xi}\bar{\eta}\sin\phi$, $z' = d\xi\eta$, where $\bar{\xi} = \sqrt{\xi^2 - 1}$, and $\bar{\eta} = \sqrt{1 - \eta^2}$ (for an oblate spheroid, the corresponding relations are obtained by setting $d \to -id$ and $\xi \to i\bar{\xi}$). Here, the constant-ξ surfaces represent a family of confocal prolate(oblate) spheroids with the interfoci distance(diameter of the focal circle) being $2d$; $\xi = \xi_0$ denotes the surface of the spheroidal particle. The constant-η surfaces denote a family of confocal two-sheeted(single-sheeted) hyperboloids, and the constant-ϕ surfaces are planes passing though the axis of symmetry.

The total velocity field $\boldsymbol{u}$ may be written as $\boldsymbol{u} = \boldsymbol{\Gamma} \cdot \boldsymbol{x} + \boldsymbol{u'}$ where $\boldsymbol{u'}$ is the disturbance velocity field that is a function of the instantaneous spheroid orientation and vanishes in the far-field. The solution for $\boldsymbol{u'}$ is best accomplished in a body-fixed coordinate system. Defining (X', Y', Z') as the body-fixed coordinate system (see Figure 1.1), the polar angle θ_j denoting the angle between the Z and Z' axes, and the azimuthal angle ϕ_j denoting the dihedral angle between $X - Z$ and $X' - Z'$ planes, with the Y' axis constrained to lie in the flow gradient $(X - Y)$ plane, the rate of strain tensor, $\boldsymbol{E} = (\boldsymbol{\Gamma} + \boldsymbol{\Gamma}^T)/2$, is given by:

$$\boldsymbol{E'} = \begin{bmatrix} \frac{\cos^2\theta_j \sin 2\phi_j}{2} & \frac{\cos\theta_j \cos 2\phi_j}{2} & \frac{\sin 2\theta_j \sin 2\phi_j}{4} \\ \frac{\cos\theta_j \cos 2\phi_j}{2} & -\frac{\sin 2\phi_j}{2} & \frac{\sin\theta_j \cos 2\phi_j}{2} \\ \frac{\sin 2\theta_j \sin 2\phi_j}{4} & \frac{\sin\theta_j \cos 2\phi_j}{2} & \frac{\sin^2\theta_j \sin 2\phi_j}{2} \end{bmatrix} \tag{1.4}$$

in body-fixed coordinates. As shown by [103] in the context of a nearly spherical particle, the rate of strain tensor above can be resolved into five elementary components, each corresponding to a canonical linear flow and may be written as,

$$\boldsymbol{E} = \boldsymbol{E}_1 + \boldsymbol{E}_2^{(i)} + \boldsymbol{E}_2^{(ii)} + \boldsymbol{E}_3^{(i)} + \boldsymbol{E}_3^{(ii)}, \tag{1.5}$$

with the component strain rates being:

$$\boldsymbol{E}_1 = \begin{bmatrix} -\frac{\sin^2\theta_j \sin 2\phi_j}{4} & 0 & 0 \\ 0 & -\frac{\sin^2\theta_j \sin 2\phi_j}{4} & 0 \\ 0 & 0 & \frac{\sin^2\theta_j \sin 2\phi_j}{2} \end{bmatrix},$$

$$\boldsymbol{E}_2^{(i)} = \begin{bmatrix} \frac{(\cos^2\theta_j + 1)\sin 2\phi_j}{4} & 0 & 0 \\ 0 & -\frac{-(\cos^2\theta_j + 1)\sin 2\phi_j}{4} & 0 \\ 0 & 0 & 0 \end{bmatrix}, \boldsymbol{E}_2^{(ii)} = \begin{bmatrix} 0 & \frac{\cos\theta_j \cos 2\phi_j}{2} & 0 \\ \frac{\cos\theta_j \cos 2\phi_j}{2} & 0 & 0 \\ 0 & 0 & 0 \end{bmatrix},$$

$$\boldsymbol{E}_3^{(i)} = \begin{bmatrix} 0 & 0 & \frac{\sin 2\theta_j \sin 2\phi_j}{4} \\ 0 & 0 & 0 \\ \frac{\sin 2\theta_j \sin 2\phi_j}{4} & 0 & 0 \end{bmatrix}, \boldsymbol{E}_3^{(ii)} = \begin{bmatrix} 0 & 0 & 0 \\ 0 & 0 & \frac{\sin\theta_j \cos 2\phi_j}{2} \\ 0 & \frac{\sin\theta_j \cos 2\phi_j}{2} & 0 \end{bmatrix}.$$

Axisymmetric Extension	$\boldsymbol{u}_{1s} = -\frac{d\bar{\xi}_0}{2(Q_1^1(\xi_0)-\xi_0 Q_2^1(\xi_0))} \sin^2\theta_j \sin 2\phi_j \boldsymbol{S}_{20}^{(3)}$
Transverse planar extension	$\boldsymbol{u}_{2s} = -\frac{d\bar{\xi}_0}{2(3Q_1^1(\xi_0)-\xi_0 Q_2^1(\xi_0))} \sin 2\phi_j \left(1+\cos^2\theta_j\right) \left[\boldsymbol{S}_{22}^{(3)} + \boldsymbol{S}_{2,-2}^{(3)}\right]$ $\boldsymbol{u}_{3s} = \frac{\mathrm{i}\, d\bar{\xi}_0}{3Q_1^1(\xi_0)-\xi_0 Q_2^1(\xi_0)} \cos\theta_j \cos 2\phi_j \left[\boldsymbol{S}_{22}^{(3)} - \boldsymbol{S}_{2,-2}^{(3)}\right]$
Longitudinal planar extension	$\boldsymbol{u}_{4s} = \frac{d\xi_0\bar{\xi}_0}{2Q_2^1(\xi_0)(2\xi_0^2-1)} \sin 2\theta_j \sin 2\phi_j \left[\boldsymbol{S}_{21}^{(3)} - \boldsymbol{S}_{2,-1}^{(3)}\right]$ $\boldsymbol{u}_{5s} = -\frac{\mathrm{i}\, d\xi_0\bar{\xi}_0}{2Q_2^1(\xi_0)(\xi_0^2-1)} \sin\theta_j \cos 2\phi_j \left[\boldsymbol{S}_{21}^{(3)} + \boldsymbol{S}_{2,-1}^{(3)}\right]$

Table 1.1 The five component disturbance velocity fields in a body-fixed coordinate system

The corresponding disturbance velocity fields may be expressed in terms of the appropriate decaying vector spheroidal biharmonics. Following [29, 30], the disturbance velocity field for an arbitrary aspect ratio spheroid may similarly be written as:

$$\boldsymbol{u'}(\boldsymbol{x'}) = \sum_{i=1}^{5} \boldsymbol{u}_{is}(\boldsymbol{x'}), \tag{1.6}$$

where the $\boldsymbol{u}_{is}(\boldsymbol{x'})$'s refer to the component disturbance fields, and are defined in Table 1.1. $\boldsymbol{u}_{1s}$ corresponds to an axisymmetric extension with the axis of symmetry coincident with the spheroid axis; $\boldsymbol{u}_{2s}$ and $\boldsymbol{u}_{3s}$ correspond to a pair of planar extensions in the plane orthogonal to the spheroid axis, with their principal axes rotated by an angle of $\pi/4$ relative to each other, and $\boldsymbol{u}_{4s}$ and $\boldsymbol{u}_{5s}$ correspond to planar extensions in a pair of orthogonal planes containing the spheroid axis. The decaying spheroidal biharmonics in the expressions for the disturbance velocity fields in Table 1.1 are of the general form $\boldsymbol{S}_{ts}^{(3)}$, and are defined as:

$$\begin{aligned}\boldsymbol{S}_{ts}^{(3)} \quad = \quad & \boldsymbol{e}_1 \left\{-(x'-\mathrm{i}y')D_2 F_{t-1}^{s-1} - \bar{\xi}_0^2 d D_1 F_t^s + (t+s-1)(t+s)\beta_{-(t+1)} F_{t-1}^{s-1}\right\} + \\ & \boldsymbol{e}_2 \left\{(x'+\mathrm{i}y')D_1 F_{t-1}^{s+1} - \bar{\xi}_0^2 d D_2 F_t^s - (t-s-1)(t-s)\beta_{-(t+1)} F_{t-1}^{s+1}\right\} + \\ & \mathbf{1}_{z'} \left\{z' D_3 F_{t-1}^s - \xi_0^2 d D_3 F_t^s - C_{-(t+1),s} F_{t-1}^s\right\},\end{aligned} \tag{1.7}$$

where,

$$F_t^s(\boldsymbol{r}, d) = Q_t^s(\xi) Y_t^s(\eta,\phi), \quad Y_t^s(\eta,\phi) = \frac{(t-s)!}{(t+s)!} P_t^s(\eta)\exp(\mathrm{i}\, s\phi) \tag{1.8}$$

$$\beta_t = \frac{t+3}{(t+1)(2t+3)}, \quad C_{t,s} = (t+s+1)(t-s+1)\beta_t, \quad |s| \le t \tag{1.9}$$

$$\boldsymbol{e}_1 = \frac{\mathbf{1}_{x'} + \mathrm{i}\,\mathbf{1}_{y'}}{2}, \quad \boldsymbol{e}_2 = \frac{\mathbf{1}_{x'} - \mathrm{i}\,\mathbf{1}_{y'}}{2} \tag{1.10}$$

$$D_1 = (\partial_{x'} - i\,\partial_{y'}), \quad D_2 = (\partial_{x'} + i\,\partial_{y'}), \quad D_3 = \partial_{z'}. \tag{1.11}$$

Here, Y_t^s are the scalar surface harmonics, with P_t^s and Q_t^s being the associated Legendre functions of the first and second kind, respectively; the index t in $\boldsymbol{S}_{ts}^{(3)}$ denotes the rapidity of the decay for large ξ(or r), with $\lim_{r\to\infty} \boldsymbol{S}_{ts}^{(3)} \propto r^{-t}$. Thus, all of the $\boldsymbol{S}_{2s}^{(3)}$'s appearing in the disturbance velocity fields (Table 1.1) decay as $1/r^2$, as is appropriate since the force-free freely rotating spheroid appears as a fluctuating force-dipole in the far-field.

The complete dynamical system governing the evolution of the fluid pathlines in terms of the position vector($\boldsymbol{x}$) and Jeffery angles(θ_j, ϕ_j) may now be written as:

$$\frac{d\boldsymbol{x}}{dt} = \boldsymbol{\Gamma} \boldsymbol{\cdot} \boldsymbol{x} + \boldsymbol{\mathcal{R}}^T(\theta_j, \phi_j) \cdot \sum_{i=1}^{5} \boldsymbol{u}_{is}(\boldsymbol{x'}), \tag{1.12}$$

$$\frac{d\phi_j}{dt} = -\frac{1}{\kappa^2+1}\left(\kappa^2 \sin^2\phi_j + \cos^2\phi_j\right), \tag{1.13}$$

$$\frac{d\theta_j}{dt} = \frac{1}{4}\left(\frac{\kappa^2-1}{\kappa^2+1}\right)\sin 2\theta_j \sin 2\phi_j. \tag{1.14}$$

Here, $\boldsymbol{\mathcal{R}}(\theta_j, \phi_j)$ is the rotation tensor relating the space and body-fixed coordinates.

Chapter 2

Spheroid in a simple shear flow: The regular pathlines

2.1 A spheroid in the spinning orbit($C = 0$)

To begin with, we analyze the simpler case of a spheroid in its spinning(log-rolling) orbit. The results for the streamlines around an arbitrary aspect ratio spheroid, aligned with the vorticity axis, haven't been reported before. This simple case also serves as a partial validation for our numerical integration, based on prior knowledge of the streamline patterns for the limiting cases of a cylinder and a sphere. The spinning (log-rolling) orbit corresponds to $\theta_j = 0$, and is obtained from (1.1) by setting the orbit constant $C = 0$. For this configuration, the only non-zero component in the general disturbance field is $\boldsymbol{u}_{3s}$, corresponding to a transverse planar extension with the extensional axis at 45 degrees to the flow and gradient axes.

2.1.1 The streamline pattern for the spinning spheroid

Numerically integrating (1.12) with only the disturbance velocity field $\boldsymbol{u}_{3s}$ one may obtain the streamlines around a spinning spheroid. Figures 2.1 and 2.2 show the topology of the streamlines both within and outside of the flow gradient plane. Figure 2.1 depicts the in-plane streamline patterns for a sphere, a cylinder and a prolate spheroid with $\xi_0 = 1.05(\kappa = 3.28)$. The qualitative resemblance between the patterns is readily evident, the streamline topology being identical in all three cases. The only perceptible difference is an increase in the size of the closed streamline region as one moves from the sphere to the cylinder, this being consistent with the increasing strength of the velocity disturbance, as is also evident from the far-field behavior of the disturbance field in the two cases - the $O(1/r^2)$ decay for the sphere as opposed to the $O(1/r)$ decay for the circular cylinder. Figure 2.2 shows the off-plane streamlines, which intersect the gradient-vorticity plane at $z = 0.5$. The three-dimensional view (Figure 2.2c), and the projections of these streamlines on the flow-gradient (Figure 2.2a) and gradient-vorticity (Figure 2.2b) planes are included. The separatrix surface is non-axisymmetric for all cases except that of a sphere, and this is evident from the differing projections of the separatrix envelope in the aforementioned planes; note that the envelope in the flow-gradient plane is a single streamline, but that in the gradient-vorticity plane is constructed from multiple separatrix streamlines (also shown

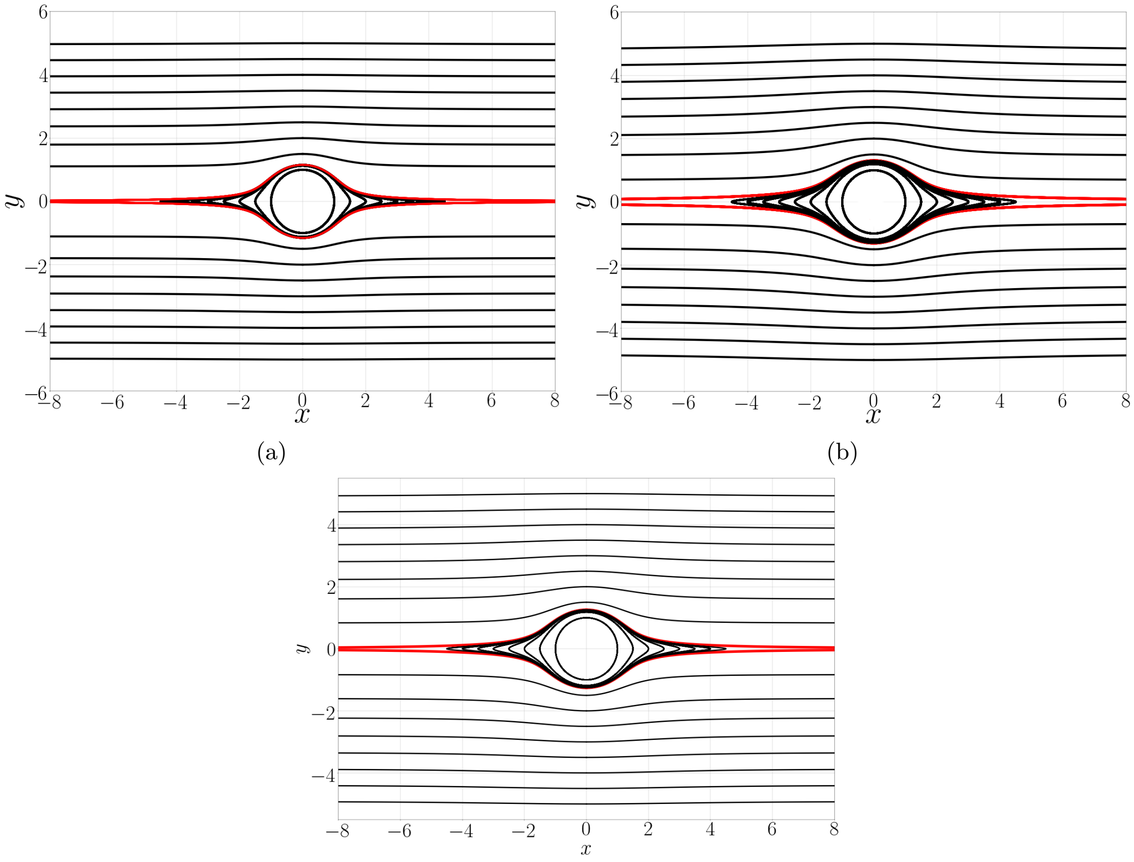

(a)

(b)

(c)

Fig. 2.1 The in-plane fore-aft symmetric streamline pattern for (a) a sphere, (b) a cylinder and (c) a prolate spheroid with $\kappa = 3.28 (\xi_0 = 1.05)$. In each case, fore-aft open streamlines are separated from the closed ones by separatrices(shown in red).

in red in Figure 2.2b). Figures 2.3a and 2.3b show the shapes of both an open and a closed streamline around log-rolling prolate spheroids with different aspect ratios ($\kappa = 10.04, 3.25, 1.67, 1.15$); also included are limiting cases of a sphere ($\kappa = 1$) and a cylinder ($\kappa = \infty$). The open streamline deviates the most (least) from the corresponding ambient streamline, and the closed streamline is largest (smallest) in size, for $\kappa = \infty(1)$. Figure 2.3c shows the time periods for closed streamlines, starting from a given location on the flow axis, increasing monotonically as one goes from a cylinder to a sphere. The limiting values for a sphere and cylinder are available for earlier efforts[108, 88]. All of these features are again consistent with the larger disturbance field associated with longer prolate spheroids (the cross-sectional diameter is fixed as κ varies), with the largest disturbance corresponding to a cylinder. In summary, the streamline topology associated with a spinning spheroid is identical to that around a sphere and a circular cylinder, with the various measures associated with the streamline pattern around a log-rolling prolate spheroid, including the time periods of the closed streamlines, the width of the closed streamline region etc, bounded between those for a sphere and a cylinder.

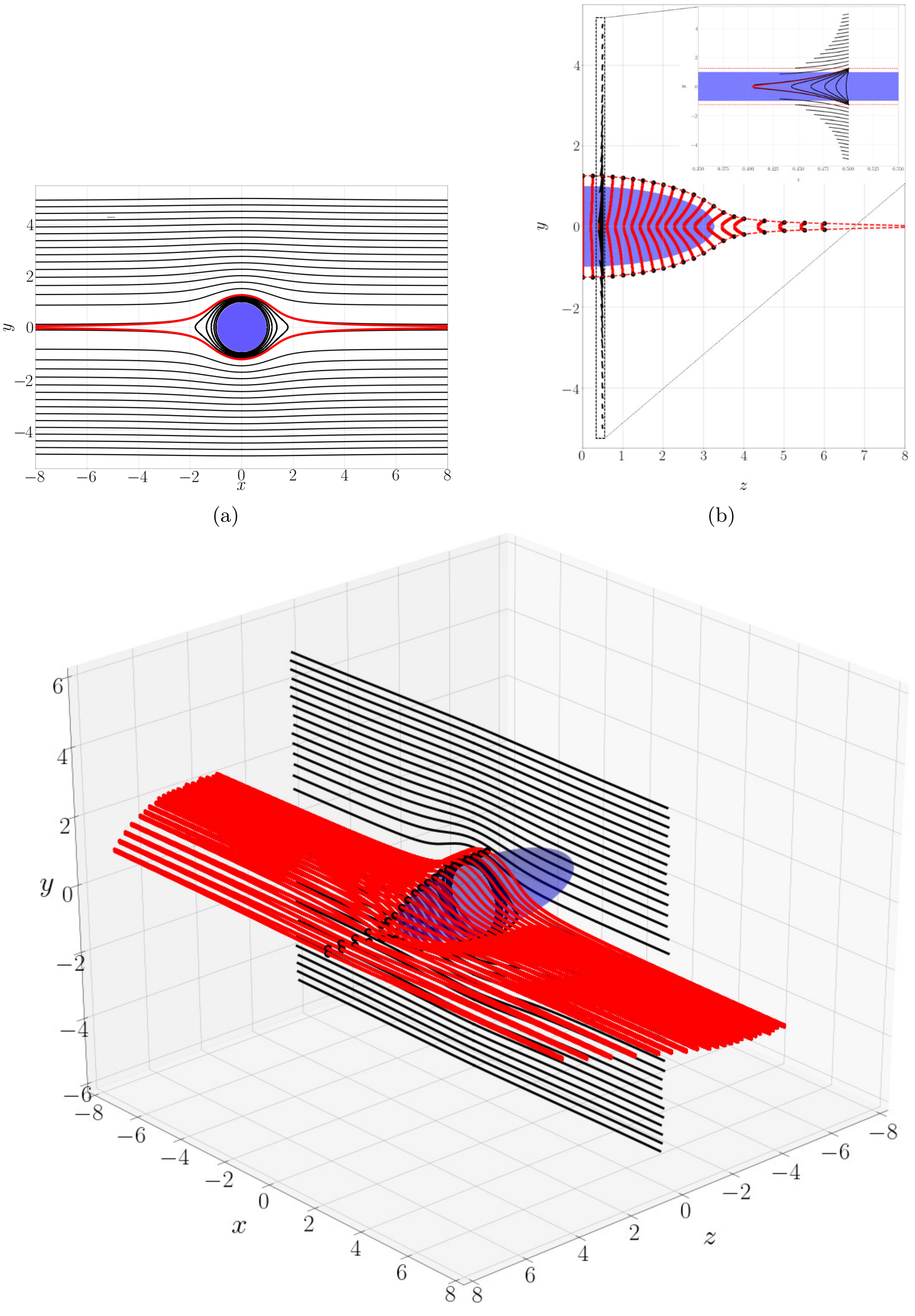

(a)

(b)

(c)

Fig. 2.2 The three-dimensional streamline pattern around a log-rolling prolate spheroid with $\kappa = 3.28(\xi_0 = 1.05)$ corresponding to $z = 0.5$(on the gradient-vorticity plane). The subfigures include projections on the flow-gradient plane (a), the gradient-vorticity plane (b), and a three dimensional view (c). The projection of the separatrix surface, and the constituent separatrix streamlines, in each of these figures are shown in red. In figure 4c, black dots denote the intersection of the separatrix envelope with the gradient-vorticity plane.

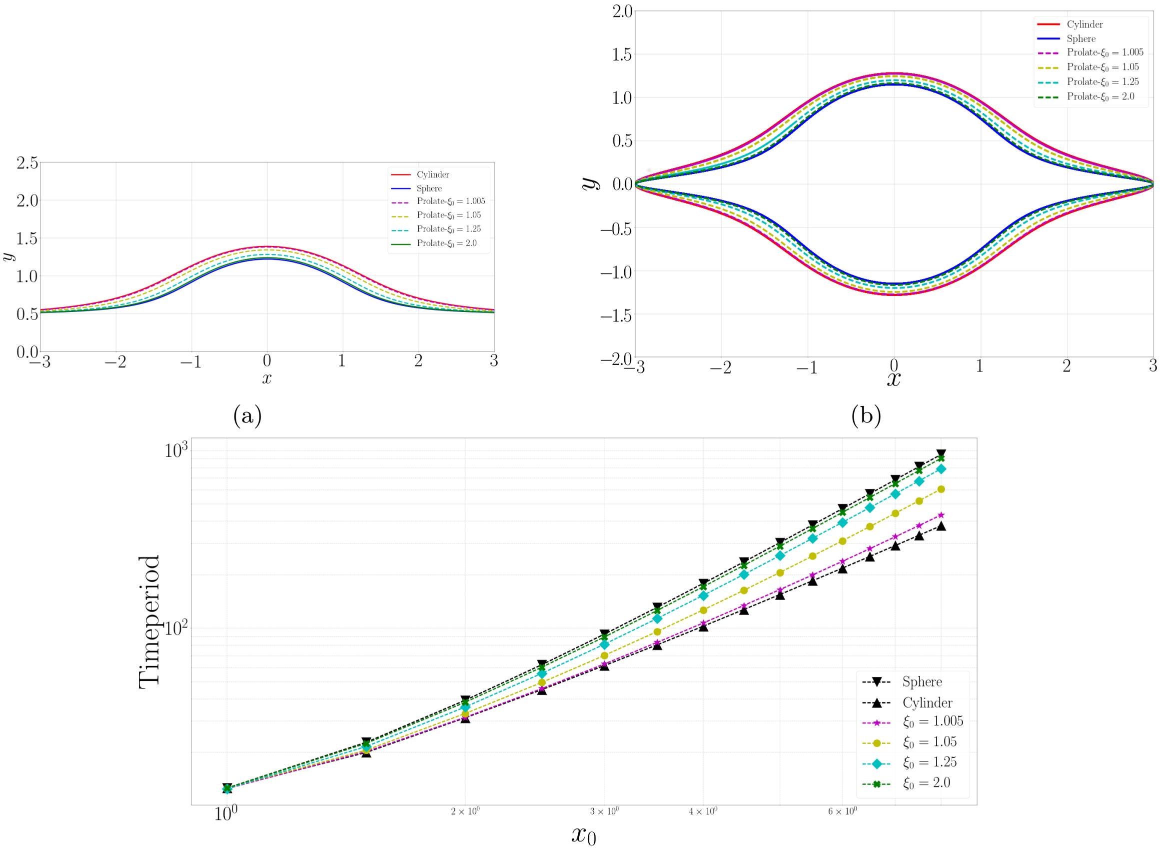

(a) (b)

(c)

Fig. 2.3 The shapes of the open (a) and closed (b) streamlines for prolate spheroids with $\kappa(\xi_0) = 10.04(1.005), 3.25(1.05), 1.67(1.25), 1.15(2)$; the limiting cases of a sphere($\kappa = 1$) and a cylinder($\kappa = \infty$) are shown. The open streamlines coincide at upstream and downstream infinity, while the closed streamlines start from the same location on the flow axis $(-3.0, 0)$; (c) A comparison of closed-streamline time periods for the aforementioned aspect ratios, including the limiting sphere and cylinder cases.

2.1.2 The far-field separatrix for a spinning spheroid

The analytical form of the separatrix for a sphere is known[14], and is given by $y = \sqrt{1/3}x^{-3/2}$; an implication of the rather slow approach of the separatrix towards the flow axis is that an infinite volume of fluid is contained within the axisymmetric separatrix envelope. To derive the far-field separatrix for an arbitrary aspect ratio spheroid, we start from the multipole expansion for the velocity field induced by a spheroid in an ambient linear flow, given by[20–22]:

$$\begin{aligned} \boldsymbol{u}(\boldsymbol{x}) &= \boldsymbol{\Gamma}\cdot\boldsymbol{x} + \mathsf{S}\cdot\boldsymbol{\nabla}\frac{3}{D}\frac{\partial}{\partial D}\left[\frac{\sinh D}{D}\right]\frac{\boldsymbol{\mathcal{G}}(\boldsymbol{x})}{8\pi\mu} \\ &= \boldsymbol{\Gamma}\cdot\boldsymbol{x} + \mathsf{S}\cdot\boldsymbol{\nabla}\left[1 + \frac{3.4}{5!}D^2 + \frac{3.6}{7!}D^4 + \cdots\right]\frac{\boldsymbol{\mathcal{G}}(\boldsymbol{x})}{8\pi\mu}, \end{aligned} \tag{2.1}$$

where $D^2 = d^2\xi_0^{-2}\left[\nabla^2 + (\kappa^2 - 1)\boldsymbol{pp}\colon\boldsymbol{\nabla\nabla}\right]$ ($D^2 = d^2\xi_0^2\left[\nabla^2 + (\kappa^2 - 1)\boldsymbol{pp}\colon\boldsymbol{\nabla\nabla}\right]$) for a prolate(an oblate) spheroid. In (2.1), $\boldsymbol{p} = \mathbf{1}_z$, $\boldsymbol{\mathcal{G}}$ is the Oseen-Burger's tensor given by $\mathcal{G}_{ij} = \delta_{ij}/r + x_i x_j/r^3$, and S is the stresslet induced by a force and torque-free spinning spheroid in an ambient shear flow, and may be written as:

$$\mathsf{S} = \frac{20\pi\mu d^3\xi_0^3}{3} K_{tp/o}\,(\delta_{il} - p_i p_l)E_{lk}(\delta_{kj} - p_k p_j) + \frac{1}{2}(E_{kl}p_k p_l)(\delta_{ij} - p_i p_j). \tag{2.2}$$

In (2.2), the stresslet coefficient $K_{tp/o}$ is a different function of aspect ratio for prolate and oblate spheroids(see Table 2.1), and characterizes the magnitude of the stresslet response for a tranverse planar extensional flow.

The dipole($\boldsymbol{u}^d$) and octupole($\boldsymbol{u}^o$) contributions correspond to the first and second terms in (2.1) and, for a prolate spheroid, are given by:

$$\begin{aligned} u_i^d &= \frac{1}{8\pi\mu} S_{jk}\partial_k \mathcal{G}_{ij} = -\frac{3}{8\pi\mu}\frac{S_{jk}n_j n_k}{r^2} n_i, && (2.3)\\ u_i^o &= \frac{d^2\bar{\xi}_0^2}{80\pi\mu\, r^4}\left[-12S_{ij}n_j + 30n_i(S_{jk}n_j n_k) + (\kappa^2 - 1)\left\{-3\left(4p_i(S_{jk}n_j p_k) + 2n_i(S_{jk}p_k p_k)\right)\right.\right. \\ &\quad +15\left(4n_i(p_l n_l S_{jk}n_j p_k) + 2p_i(p_l n_l S_{jk} n_j n_k) + n_i(S_{jk}n_j n_k)\right) \\ &\quad \left.\left.-105n_i(p_l n_l)^2(S_{jk}n_j n_k)\right\}\right], && (2.4) \end{aligned}$$

where the unit radial vector $\boldsymbol{n} = \boldsymbol{x}/r$. To derive the asymptotic form of the separatrix, one needs to account for the higher-order octupole contribution, owing to the dipole field being purely radial, and thereby, lacking a transverse (y) component along the flow axis. Using the above velocity field in $d\boldsymbol{x}/dt = \boldsymbol{\Gamma}.\boldsymbol{x} + \boldsymbol{u}^d + \boldsymbol{u}^o$, and considering the limit $y \to 0$, $x \to \infty$, one obtains the following equations at leading order:

$$\frac{dx}{dt} = \lim_{y\to 0} u_x = y, \tag{2.5}$$

$$\frac{dy}{dt} = \lim_{y\to 0} u_y = -\frac{5y^2 d^3\xi_0^3\, K_p}{2x^4} - \frac{d^5\xi_0^3\bar{\xi_0}^2}{2x^4}K_p. \tag{2.6}$$

It is evident that the x-component of the velocity in (2.5) is just the ambient flow (y) at leading order, while the dominant contribution in (2.6) is the octupolar contribution; that this term of $O(1/x^4)$ is dominant over the dipole contribution of $O(y^2/x^4)$ is easily seen since y for the separatrix is asymptotically small in the far-field. With the far-field forms in place above, the form of the separatrix may be obtained by taking the ratio of (2.5) and (2.6), and integrating the resulting differential equation. One obtains $y = 1/\sqrt{3}\, d^{5/2}\xi_0^{3/2}\bar{\xi}_0 K_p^{1/2} x^{-3/2}$ which exhibits the same far-field decay as the sphere separatrix. Figure 2.4 shows the separatrices for log-rolling prolate spheroids of different aspect ratios, and compares their far-field forms with the analytical prediction above (shown in dotted lines). For sufficiently large aspect ratios ($\kappa \to \infty$ or $\xi_0 \to 1$), the separatrix exhibits an intermediate asymptotic form, $(1/\sqrt{2})x^{-1}$, in the interval $1 \ll x \ll \kappa$, corresponding to that of a circular cylinder, before eventually transitioning to the more rapid $O(x^{-3/2})$ decay for $x \gg \kappa$.

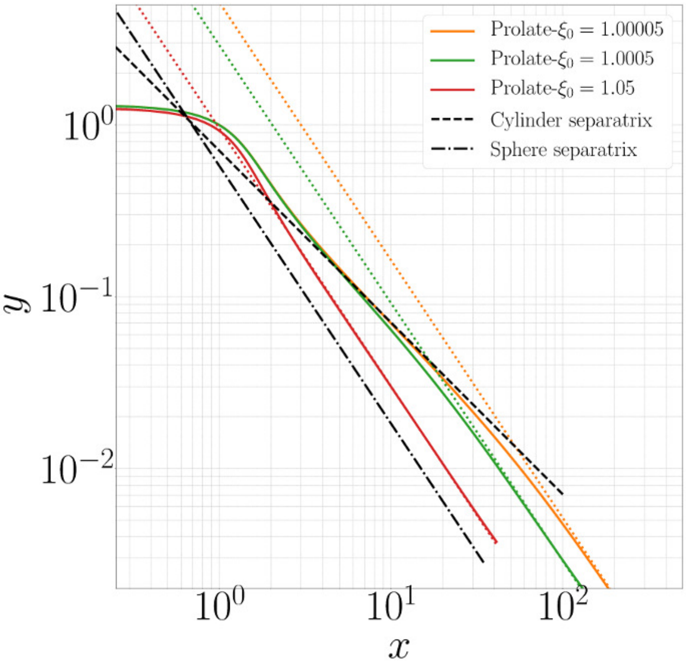

Fig. 2.4 Separatrices in the flow-gradient plane, for spinning prolate spheroids($\kappa = 100.04, 31.63, 10.04, 3.28$) in a simple shear flow. The dashed lines represent the predictions of the asymptotic analysis in the text.

2.2 A spheroid in non-spinning orbits($C > 0$)

2.2.1 Regular open pathlines

The results presented thus far show that the streamline pattern around spinning spheroids is steady, and analogous to that around a sphere. In this section, we consider spheroids in orbits other than the spinning one ($C > 0$). For all such cases, the velocity field is time dependent. The focus from hereon will therefore be on the fluid pathlines rather than the (time periodic) sequence of instantaneous streamline patterns associated with the rotating spheroid. In our examination of fluid pathlines, it is natural to start from a spheroid tumbling in the flow-gradient plane. The polar Jeffery angle is now a constant ($\theta_j = \pi/2$), with the time dependence of the velocity field arising only due to ϕ_j varying with time. Thus, one only needs to integrate (2.11) and (2.12) in order to characterize the pathlines. Further, the disturbance velocity field only involves three of the five canonical components in the disturbance velocity fields in Table 1.1 viz. the axisymmetric extension($\boldsymbol{u}_{1s}$), the first transverse extension($\boldsymbol{u}_{2s}$) and the second longitudinal extension($\boldsymbol{u}_{5s}$). An additional simplification, owing to reasons of symmetry, is that fluid elements in the flow-gradient plane are confined to this plane for all times, despite the time dependence of the flow field. This makes it easier to visualize the changes in the pathline topology relative to the case of a spheroid rotating in a generic precessional orbit.

The changing orientation of the tumbling spheroid implies that, unlike the spinning case, one needs to specify an ‘initial’ orientation in order to fix the fluid pathlines. A convenient choice is the spheroid orientation at the instant that the fluid element crosses the gradient-vorticity plane ($x = 0$); the coordinates of the element at this instant may be taken as (y_0, z_0). This orientation is fixed by the azimuthal Jeffery angle ϕ_{j0}. The fore-aft symmetry of the spheroid implies that ϕ_{j0} may be restricted to the interval $(0, \pi)$. Further, from reversibility considerations, one only need consider ϕ_{j0}'s in the interval $(0, \pi/2)$, since the pathline configuration for $\pi - \phi_{j0}$ may be obtained from that for ϕ_{j0} via a reflection transformation with respect to the gradient-vorticity plane. Each ϕ_{j0} in $(0, \pi/2)$ leads to a distinct configuration of pathlines, an individual pathline being obtained by integrating forward and backward in time starting from the initial position of the fluid element in the gradient-vorticity plane. The pathline configurations for fluid elements in the flow-gradient plane, and for five different values of ϕ_{j0} in $(0, \pi/2)$, are shown in figure 2.5. While the pathlines for the cases $\phi_{j0} = 0$ and $\pi/2$ are evidently fore-aft symmetric, all other values of ϕ_{j0} lead to fore-aft asymmetric open pathlines that suffer a net displacement (Δy) in the gradient direction as they head from upstream to downstream infinity. By analogy with the spinning spheroid, the 'limiting' open pathlines are again shown in red for all configurations in figure 2.5. The expectation is that these red curves now serve as fore-aft asymmetric separatrices (for $\phi_{j0} \neq 0, \pi/2$), asymptoting to the flow axis far upstream or downstream. These separatrices would therefore seem to demarcate pathlines that extend to infinity in the upstream and downstream directions from those that do not, being forced to cross the flow axis at a finite x, either positive or negative (in a manner similar to the spinning spheroid or sphere above). It will be seen in section 5, where we consider pathlines that loop around the spheroid as a function of their upstream coordinates, that a subset of these separatrices mark the onset of chaotic scattering. This subset must correspond to the interval $\phi_{j0} \in (\pi/2, \pi)$ since, as implied by figure 2.5, it is separatrices with ϕ_{j0}'s in the above interval that begin from finite offsets, and are therefore accessible from upstream infinity.

Figure 2.6 shows the off-plane pathline configurations, again for a tumbling prolate spheroid. As for the inplane case, the pathlines correspond to fluid elements that cross the gradient-vorticity plane ($x = 0$) at a fixed vorticity offset of $z = 0.25$; the ϕ_{j0} values are the same as in figure 2.5. Expectedly, the off-plane pathlines are three-dimensional trajectories, and their fore-aft asymmetry manifests as net displacements in both the gradient and vorticity directions; these displacements(Δy or Δz) are indicated in the relevant pathline projections. Note that the 'separatrices' in particular have small scale wiggles superposed on a slower large-scale variation, on account of the tumbling dynamics of the spheroid.

Lateral displacements of the regular open pathlines: $0 < C \leq \infty$

The upstream and downstream coordinates, along the gradient and vorticity directions, are identical for all open streamlines associated with the spinning spheroid or a sphere. An obvious measure of fore-aft asymmetry, as already implied in figures 2.5 and 2.6, is therefore the difference between the upstream and downstream gradient and vorticity coordinates of a given open pathline. These lateral displacements in the gradient (Δy) and vorticity (Δz) directions have been used earlier to characterize the asymmetry of finite-St pair-sphere trajectories(St here being the Stokes number, and a measure of particle inertia; see [100]). The definition of the lateral displacement in the gradient direction(Δy) is indicated in figure 2.7a, along with a schematic in figure 2.7b highlighting the coordinates used for a general off-plane pathline. Both Δy and Δz may be calculated numerically, in a straightforward manner, for all pathlines down to the 'separatrices' shown in figures 2.5 and 2.6. For pathlines that approach the spheroid to within a distance of order its major axis, the lateral displacements will be comparable to the respective upstream coordinates: that is, $\Delta y \sim O(y_{-\infty})$ and $\Delta z \sim O(z_{-\infty})$. For far-field pathlines, however, the displacements are much smaller, allowing for an analytical approach involving a perturbation about the upstream coordinates. The analysis requires the expression for the far-field disturbance velocity

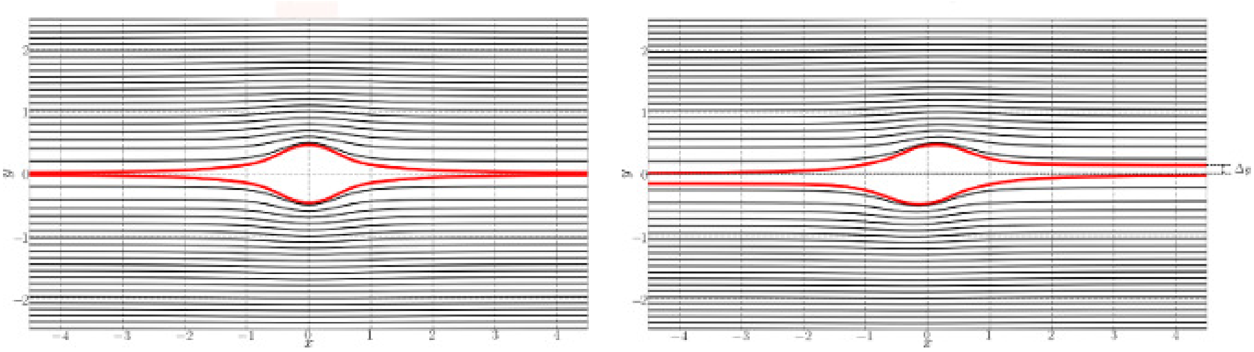

(a) $\phi_{j0} = 0$ (b) $\phi_{j0} = \pi/6$

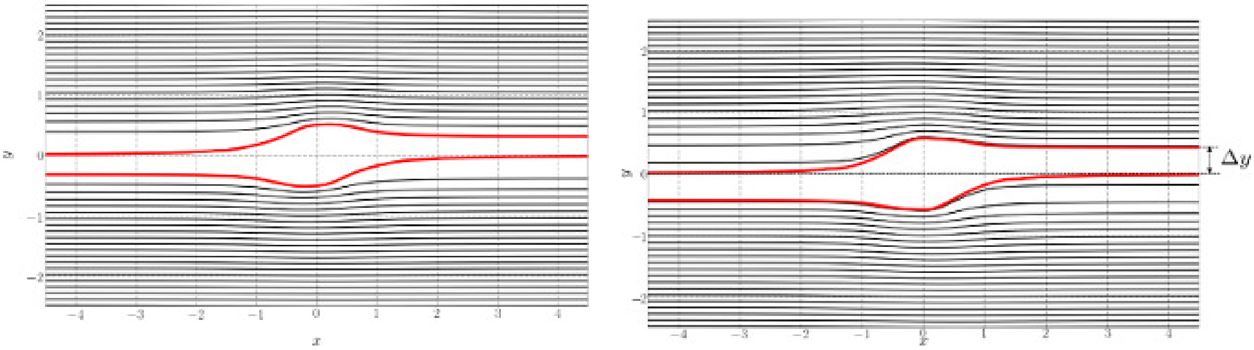

(c) $\phi_{j0} = \pi/4$ (d) $\phi_{j0} = \pi/3$

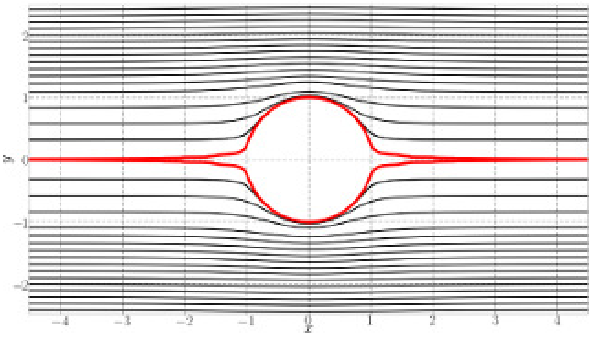

(e) $\phi_{j0} = \pi/2$

Fig. 2.5 The configuration of the inplane regular pathlines for a tumbling prolate spheroid with $\kappa = 3.28(\xi_0 = 1.05)$. The different configurations correspond to ϕ_{j0} values of (a)0, (b)$\pi/6$, (c)$\pi/4$, (d)$\pi/3$, and (e)$\pi/2$. All configurations are bounded below by separatrices shown in red. The Δy marked in (b) and (d) denotes the lateral displacement in the gradient direction.

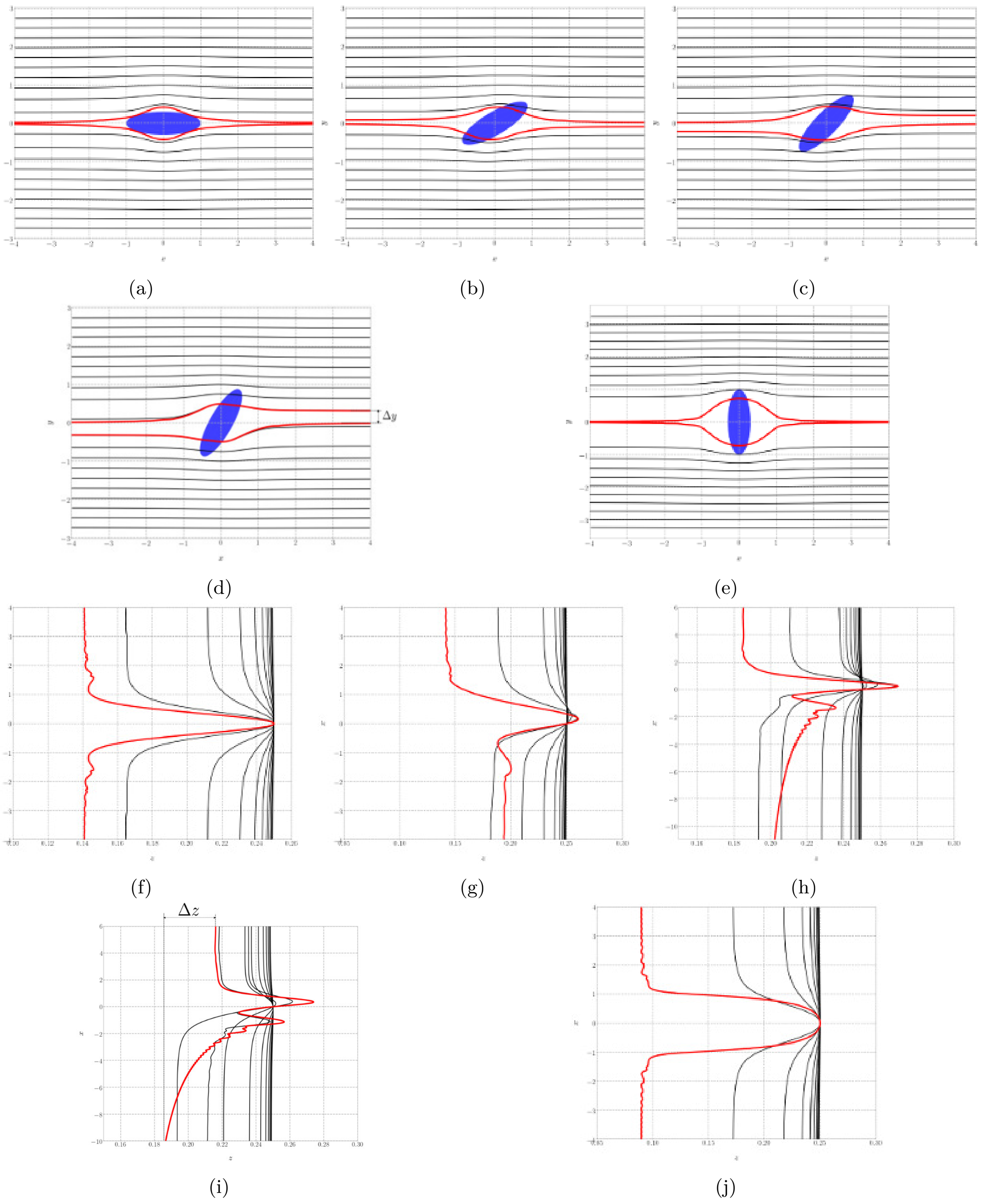

(a) (b) (c)

(d) (e)

(f) (g) (h)

(i) (j)

Fig. 2.6 The configurations of the off-plane(vorticity offset $z = 0.25$) regular open pathlines projected onto the flow-gradient(a,b,c,d,e) and flow-vorticity(f,g,h,i,j) planes for a tumbling prolate spheroid with $\kappa = 3.28(\xi_0 = 1.05)$; off-plane separatrices are shown in red. The different configurations correspond to ϕ_{j0} values of (a,f)0, (b,g)$\pi/6$, (c,h)$\pi/4$, (d,i)$\pi/3$, and (e,j)$\pi/2$. Δy and Δz denote the lateral displacements in the gradient and vorticity directions, respectively.

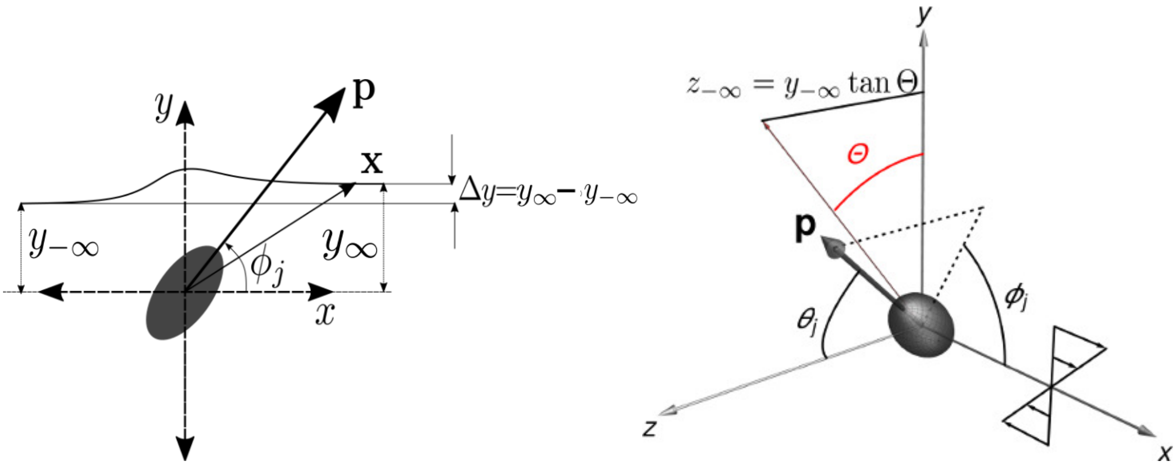

(a) (b)

Fig. 2.7 Figure (a) shows the lateral displacement of a regular open fluid pathline in the flow-gradient plane. Θ in (b) characterizes the initial upstream location of a fluid element outside the flow-gradient plane.

field due to a spheroid rotating in a precessional orbit. In contrast to a spinning spheroid discussed in section 2.1.2, a torque-free spheroid rotating in a generic Jeffery orbit appears, at leading order, as a time-dependent stresslet. The stresslet is now the sum of three distinct contributions, and may be written in the form:

$$\mathsf{S} = \frac{20\pi\mu d^3\xi_0^3}{3}\left(K_{ap/o}\,\mathsf{E}_\mathsf{a} + K_{tp/o}\,\mathsf{E}_\mathsf{t} + K_{lp/o}\,\mathsf{E}_\mathsf{l}\right). \tag{2.7}$$

where the subscripts p and o denote prolate and oblate spheroids, respectively. E_a, E_t and E_l are the rate of strain tensors associated with axisymmetric extension, transverse and longitudinal planar extensions, respectively, that, in invariant form, are given by:

$$E_{a\,ij} = (E_{kl}p_k p_l)\left[p_i p_j - \frac{\delta_{ij}}{3}\right], \tag{2.8}$$

$$E_{t\,ij} = (\delta_{il} - p_i p_l)E_{lk}(\delta_{kj} - p_k p_j) + \frac{1}{2}(E_{kl}p_k p_l)(\delta_{ij} - p_i p_j), \tag{2.9}$$

$$E_{l\,ij} = p_i p_l E_{lk}(\delta_{kj} - p_k p_j) + (\delta_{il} - p_i p_l)E_{kl}p_k p_j. \tag{2.10}$$

There are only three distinct stresslet coefficients, despite the five independent canonical velocity fields in Table 1.1, since the responses of the spheroid are identical for the pair of planar and transverse longitudinal extensions (owing to its circular cross-section; see [76]). The stresslet coefficients $K_{ap/o}$, $K_{tp/o}$ and $K_{lp/o}$ are functions of aspect ratio, and the relevant expressions for both prolate and oblate spheroids appear in Table 2.1. Note that the time dependence of the stresslet in (2.7) arises from the spheroid orientation vector ($\boldsymbol{p}$) being time dependent; $\boldsymbol{p} = \sin\theta_j \cos\phi_j\, \mathbf{1}_x + \sin\theta_j \sin\phi_j\, \mathbf{1}_y + \cos\theta_j\, \mathbf{1}_z$, where the time evolution of the Jeffery angles is given by (1.13) and (1.14). The lateral displacements may now be determined, using (2.7), as:

$$\Delta y = \int_{-\infty}^{\infty} \mathbf{1}_y \cdot \boldsymbol{u}^d\, dt, \qquad \Delta z = \int_{-\infty}^{\infty} \mathbf{1}_z \cdot \boldsymbol{u}^d\, dt, \tag{2.11}$$

where $\boldsymbol{u}^d = -(3/(8\pi\mu))\mathsf{S} :\boldsymbol{nnn}/r^2$ is the leading order dipolar term in the multipole expansion (see (2.3)), with S being defined by (2.7). The distance r, between the fluid element and the spheroid center, is a function of time, and may be approximated as $r = [(y_{-\infty}t)^2 + y_{-\infty}^2(1 + \tan^2\Theta)]^{1/2}$, where the gradient and vorticity coordinates have been replaced by their upstream values, and we have used that $z_{-\infty} = y_{-\infty}\tan\Theta$(see figure 2.7b). Thus, r changes at leading order only due to convection by the ambient shear, with the instant $t = 0$ corresponding to the fluid element being in the gradient-vorticity plane, with $\phi_j = \phi_{j0}$ (see (1.13) and (1.14)). The unit radial vector is given by $\boldsymbol{n} = (t\,\mathbf{1}_x + \mathbf{1}_y + \tan\Theta\,\mathbf{1}_z)/(1 + t^2 + \tan^2\Theta)^{1/2}$ and its projections along the gradient and vorticity directions, appearing in (2.11), may be written as $n_y = \boldsymbol{n}\cdot\mathbf{1}_y = 1/(1+t^2+\tan^2\Theta)^{1/2}$ and $n_z = n_y\tan\Theta$, respectively. Using the expressions for S, n_y and n_z above, the detailed expressions for the lateral displacements associated with the far-field pathlines are given by:

$$\begin{aligned}\Delta y = {} & \frac{K_{ap/o}}{8y_{-\infty}^2}\int_{-\infty}^{\infty}\frac{dt}{(t^2+\sec^2\Theta)^{5/2}}\left[\sin^2\theta_j\left(\tan^2\Theta(3\cos 2\theta_j+1)\sin 2\phi_j\right.\right.\\ & +6\tan\Theta\sin 2\theta_j\sin 2\phi_j(\sin\phi_j+t\cos\phi_j)+12\sin^2\theta_j\sin\phi_j\cos\phi_j\left(t^2\cos^2\phi_j+\sin^2\phi_j\right)\\ & \left.\left.+6t\sin^2\theta_j\sin^2 2\phi_j-2\left(t^2+1\right)\sin 2\phi_j\right)\right]\\ & +\frac{K_{tp/o}}{4y_{-\infty}^2}\int_{-\infty}^{\infty}\frac{dt}{(t^2+\sec^2\Theta)^{5/2}}\left[\frac{1}{2}\sin 2\theta_j\left(\left(-2\tan^2\Theta+t^2+1\right)\sin 2\theta_j\sin 2\phi_j\right.\right.\\ & \left.+4\tan\Theta(t\sin\phi_j+\cos\phi_j)\right)-8\tan\Theta\sin^3\theta_j\cos\theta_j\sin 2\phi_j(\sin\phi_j+t\cos\phi_j)\\ & \left.+\sin^4\theta_j\left(2t\cos 4\phi_j-\left(t^2-1\right)\sin 4\phi_j\right)+t\sin^2\theta_j(\cos 2\theta_j+3)\right]\\ & +\frac{K_{lp/o}}{8y_{-\infty}^2}\int_{-\infty}^{\infty}\frac{dt}{(t^2+\sec^2\Theta)^{5/2}}\left[\sin^2\theta_j\sin 2\phi_j\left(\tan^2\Theta(\cos 2\theta_j+3)-2\left(t^2+1\right)\right)\right.\\ & +4\tan\Theta\sin^3\theta_j\cos\theta_j\sin 2\phi_j(\sin\phi_j+t\cos\phi_j)-4\tan\Theta\sin 2\theta_j(t\sin\phi_j+\cos\phi_j)\\ & \left.+2\sin^4\theta_j\sin 2\phi_j(\sin\phi_j+t\cos\phi_j)^2+8t\cos^2\theta_j\right]\end{aligned} \tag{2.12}$$

$$\Delta z = \Delta y\tan\Theta. \tag{2.13}$$

The integral in (2.12) is evaluated numerically, and is a function of the spheroid aspect ratio (κ), the orbit constant (C) and ϕ_{j0}; the case of a tumbling spheroid may be obtained by setting $\theta_j = \pi/2(C = \infty)$. On account of the radial nature of the dipolar field, the dominant displacement of the pathline occurs when the fluid element is at a distance of $\mathrm{O}(y_{-\infty})$ or smaller from the gradient-vorticity plane. Since this corresponds to a time interval of $\mathrm{O}(\dot{\gamma}^{-1})$, independent of $y_{-\infty}$, the far-field lateral displacements exhibit a decay of $(y_{-\infty}^{-2})$ which is the same as that of the dipolar field. In light of this decay, in figure 10, we plot the rescaled lateral displacements, $y_{-\infty}^2\Delta y$, for pathlines in the flow-gradient plane, for tumbling prolate and oblate spheroids. Owing to the simple relationship between the two lateral displacements in (2.12), in figure 2.9 we plot the re-scaled total lateral displacement, $y_{-\infty}^2\Delta r = y_{-\infty}^2\sqrt{\Delta y^2+\Delta z^2} = y_{-\infty}^2\Delta y\sec\Theta$, for pathlines outside the flow-gradient plane (corresponding to $\Theta = \pi/9$), again for tumbling prolate and oblate spheroids.

$K_{ap}=\frac{4}{15\xi_0^3\left(\left(3\xi_0^2-1\right)\coth^{-1}(\xi_0)-3\xi_0\right)}$	$K_{ao}=-\frac{4}{15\xi_0^3\left(3\sqrt{\xi_0^2-1}+\left(2-3\xi_0^2\right)\csc^{-1}(\xi_0)\right)}$
$K_{tp}=-\frac{4\left(\xi_0^2-1\right)}{5\xi_0^2\left(2\xi_0^2-1\right)\left(-3\xi_0^2+3\left(\xi_0^2-1\right)\xi_0\coth^{-1}(\xi_0)+2\right)}$	$K_{to}=-\frac{4\sqrt{\xi_0^2-1}}{5\left(2\xi_0^3-\xi_0\right)\left(-3\xi_0^2+3\sqrt{\xi_0^2-1}\xi_0^2\csc^{-1}(\xi_0)+1\right)}$
$K_{lp}=\frac{8\left(\xi_0^2-1\right)}{5\xi_0^3\left(-3\xi_0^3+3\left(\xi_0^2-1\right)^2\coth^{-1}(\xi_0)+5\xi_0\right)}$	$K_{lo}=\frac{24}{5\left(9\xi_0^5\csc^{-1}(\xi_0)-3\xi_0\sqrt{\xi_0^2-1}\left(3\xi_0^2+2\right)\right)}$

Table 2.1 The aspect-ratio-dependent stresslet coefficients that appear in the far-field stresslet disturbance (see equation (2.12) in the text).

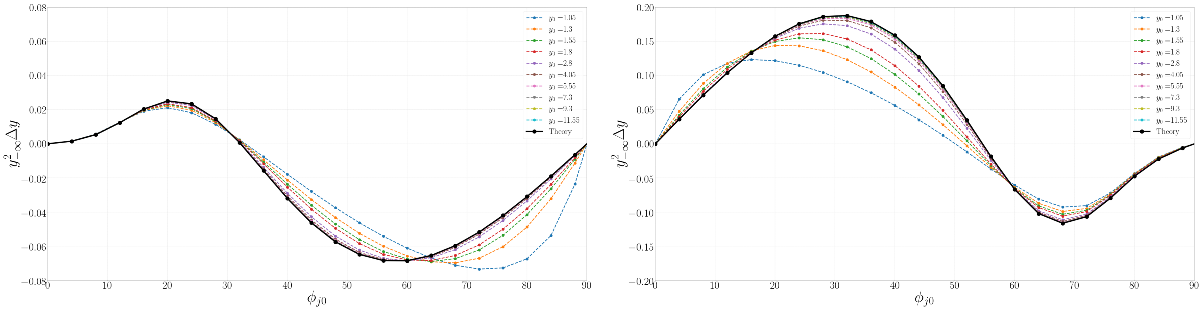

(a) (b)

Fig. 2.8 Lateral displacements in the gradient direction for fluid elements in the flow-gradient plane, as a function of the initial orientation(ϕ_{j0}). (a) A prolate spheroid ($\xi_0 = 1.01(\kappa = 7.12)$), and (b) an oblate spheroid ($\xi_0 = 1.01(\kappa = 0.14)$); both spheroids are in the tumbling orbit. The lateral displacement for $\phi_{j0} \in (\pi/2, \pi)$ may be obtained as $\Delta y(\phi_{j0}) = -\Delta y(\pi - \phi_{j0})$.

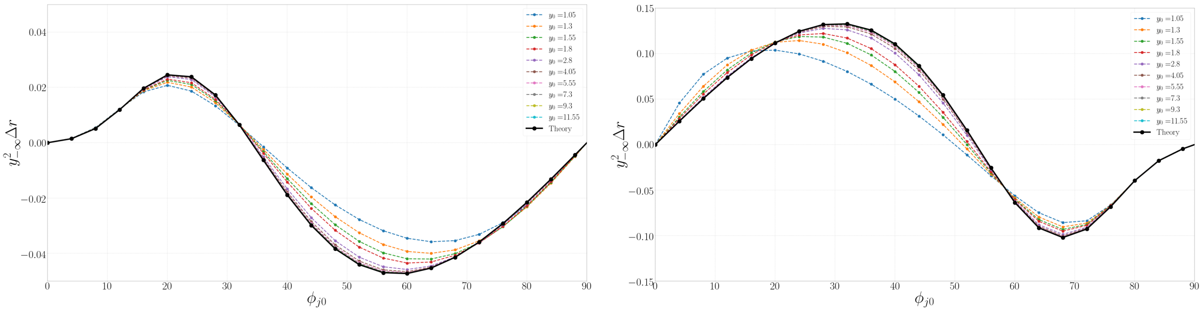

(a) (b)

Fig. 2.9 The total lateral displacements for off-plane fluid elements($\Theta = \pi/9$) as a function of the initial orientation(ϕ_{j0}). (a) A prolate spheroid ($\xi_0 = 1.01(\kappa = 7.12)$), and (b) an oblate spheroid ($\xi_0 = 1.01(\kappa = 0.14)$); both spheroids are in the tumbling orbit. The lateral displacement for $\phi_{j0} \in (\pi/2, \pi)$ may be obtained as $\Delta y(\phi_{j0}) = -\Delta y(\pi - \phi_{j0})$.

Figure 2.10 shows the re-scaled total lateral displacements for off-plane fluid elements ($\Theta = \pi/9$), and for prolate and oblate spheroids in a non-tumbling orbit ($C = 10$). Note that for this generic case, it is necessary to consider ϕ_{j0} in the larger interval $(0, \pi)$, with the displacements in the interval $(\pi, 2\pi)$ again obtained via a reflection transformation. In all cases (figures 2.8, 2.9 and 2.10), the numerical displacement curves approach the analytical far-field ones in the limit $(y^2_{-\infty} + z^2_{-\infty})^{1/2} \to \infty$.

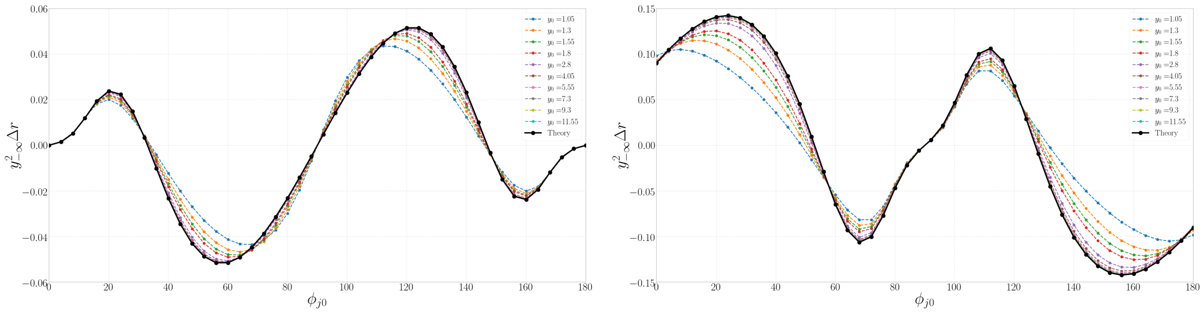

(a) (b)

Fig. 2.10 The total lateral displacements for off-plane fluid elements($\Theta = \pi/9$) as a function of the initial orientation(ϕ_{j0}). (a) A prolate spheroid ($\xi_0 = 1.01(\kappa = 7.12)$), and (b) an oblate spheroid ($\xi_0 = 1.01(\kappa = 0.14)$). Both spheroids are in a Jeffery orbit with $C = 10$. The lateral displacement for $\phi_{j0} \in (\pi, 2\pi)$ may be obtained as $\Delta y(\phi_{j0}) = -\Delta y(2\pi - \phi_{j0})$.

The separatrix of a tumbling spheroid

We end this subsection on the regular pathlines by analyzing the approach of the separatrices, marked in red in figure 2.5, towards the flow axis - the approach occurs in both the upstream and downstream directions for $\phi_{j0} = 0, \pi/2$, and in either of these two directions for other ϕ_{j0}'s. For the spinning spheroid, as seen earlier((2.5) and (2.6)), the rate of approach of the far-field separatrix ($y \propto x^{-3/2}$) remains identical to that of a sphere, with only a pre-factor that is a function of aspect ratio. The analysis for the analogously defined separatrices in figure 2.5 is more involved owing to the spheroid rotation. In the far-field ($r \gg 1$), one may, however, exploit a separation of time scales, with the fast scale corresponding to the Jeffery period (of $O(\dot\gamma^{-1})$ for $\kappa \sim O(1)$) and the slow time scale characterizing the rate of change of position of the fluid element. Note that, unlike the regular pathlines for large $y_{-\infty}$ analyzed above where this latter time scale remains $O(\dot\gamma^{-1})$, for the separatrices, the approach towards the flow axis implies that y is asymptotically small and the time scale of convection by the ambient shear is therefore correspondingly large. Note also that the magnitude of this slow time scale, being a function of y, is not known apriori. Keeping this in mind, we write the governing equations as:

$$\frac{d\boldsymbol{x}}{dT} = \boldsymbol{u}(\boldsymbol{x}, \boldsymbol{p}(\tau)) \tag{2.14}$$

$$\frac{d\boldsymbol{p}}{d\tau} = \boldsymbol{\omega} \cdot \boldsymbol{p} + \frac{\kappa^2 - 1}{\kappa^2 + 1} \left(\mathsf{E}.\boldsymbol{p} - \boldsymbol{p}\left(\mathsf{E} \colon \boldsymbol{pp}\right)\right). \tag{2.15}$$

where we have (formally) identified τ and T as the fast and slow time variables, respectively. The identification implies that $\boldsymbol{p}$ only evolves on the fast time scale, while $\boldsymbol{x}$ is a function of both τ and T. One may expand $\boldsymbol{x}$ in the usual manner $\boldsymbol{x}(T, \tau) = \boldsymbol{X}(T, \tau) + \tilde{\boldsymbol{x}}(\boldsymbol{X}, T, \tau)$ with the fast variable satisfying $1/T_j \int_0^{T_j} \tilde{\boldsymbol{x}} d\tau = 0$, with T fixed, and T_j being the Jeffery period. The slow and fast contributions of $\boldsymbol{x}$ may further be expanded in the following manner: $\boldsymbol{X}(T, \tau) = \boldsymbol{X}_0(T) + \boldsymbol{X}_1(T, \tau) + \cdots$ and $\tilde{\boldsymbol{x}} = \tilde{\boldsymbol{x}}_0 + \tilde{\boldsymbol{x}}_1 + \cdots$, respectively, where we have anticipated the leading order position to only evolve on the slow time scale. Since there isn't a readily available estimate of the slow time scale apriori, we don't introduce ε above, but nevertheless assume the higher order terms in the above expansions to be asymptotically smaller; thus, $\tilde{\boldsymbol{x}} \ll \boldsymbol{X}, \boldsymbol{X}_1 \ll \boldsymbol{X}_0$, and so on. We restrict ourselves to calculating the leading order slow contribution $\boldsymbol{X}_0(T)$ below (although, note that $\tilde{x}_0$ is responsible for the small-scale wiggles on the separatrices seen in figure 8 and figure 13.)

The far-field form may now be obtained by recalling the approximations used in the context of the spinning spheroid in section 2.1.2. Thus, in the far-field at leading order, we only retain the ambient flow in the x-component, and the octupolar contribution in the y-component. One may now write the scalar components of the two-time-scale equations as:

$$\begin{aligned}
\frac{dX_0}{dT}+\frac{\partial\tilde{x}_0}{\partial\tau} &= Y_0+\tilde{y}_0 && (2.16)\\
\frac{dY_0}{dT}+\frac{\partial\tilde{y}_0}{\partial\tau} &= -\frac{15}{4}d^5\xi_0^3L_c^2\kappa^2(\kappa^2-1)]\left[\left(K_{ap/o}-2K_{tp/o}+K_{lp/o}\right)\kappa^2\right. && (2.17)\\
&\left.\quad+2\left(K_{tp/o}-K_{ap/o}\right)\cot^2\left(\frac{\kappa\tau}{\kappa^2+1}\right)\right]\left[\kappa^2+\cot^2\left(\frac{\kappa\tau}{\kappa^2+1}\right)\right]^{-3}X_0^{-4}
\end{aligned}$$

where $L_c=\bar{\xi}_0(\xi_0)$ for a prolate(an oblate) spheroid. Averaging (2.17) and (2.18) over τ, with T fixed, and using the periodicity of the fast contributions, one obtains the equations governing X_0 and Y_0 as:

$$\begin{aligned}
\frac{dX_0}{dT} &= Y_0 && (2.18)\\
\frac{dY_0}{dT} &= -\frac{d^5\xi_0^3L_c^2}{32X_0^4(1+\kappa)^2}\kappa\left[K_{ap/o}(-3-30\kappa+9\kappa^2)\right.\\
&\quad\left.+K_{lp/o}(7-5\kappa(2+\kappa))-4K_{tp/o}(5+\kappa(-2+5\kappa))\right], && (2.19)
\end{aligned}$$

The analytical far-field form may now be obtained by taking the ratio of (2.18) and (2.19). Reverting to the original notation, one obtains the far-field separatrices (without the superimposed small-scale wiggles) in the following form:

$$\begin{aligned}
y_p &= 4\sqrt{\frac{\left(K_{ap}\left(-9\kappa^2+30\kappa+3\right)+4K_{tp}(\kappa(5\kappa-2)+5)+K_{lp}(5\kappa(\kappa+2)-7)\right)}{3\kappa(\kappa+1)^2\,x^3}}, && (2.20)\\
y_o &= 4\sqrt{\frac{\kappa\left(K_{ao}\left(-9\kappa^2+30\kappa+3\right)+4K_{to}(\kappa(5\kappa-2)+5)+K_{lo}(5\kappa(\kappa+2)-7)\right)}{3(\kappa+1)^2\,x^3}}. && (2.21)
\end{aligned}$$

again exhibiting a far-field decay of $x^{-3/2}$. Figure 2.11 shows the comparison between both fore-aft symmetric (for $\phi_{j0}=\pi/2$) and asymmetric (for $\phi_{j0}=\pi/3(\pi/6$ for oblate)) separatrices obtained numerically, and the analytical predictions above. The numerical separatrices are obtained by choosing an initial location (y_0) on the gradient axis, and progressively refining this based on the final outcome of the integrated trajectory (escape to $x\to\pm\infty$, or crossing of the flow axis at a finite x). Notwithstanding the small-scale wiggles that decrease in amplitude with increasing x, a good comparison is obtained with (2.20) and (2.21).

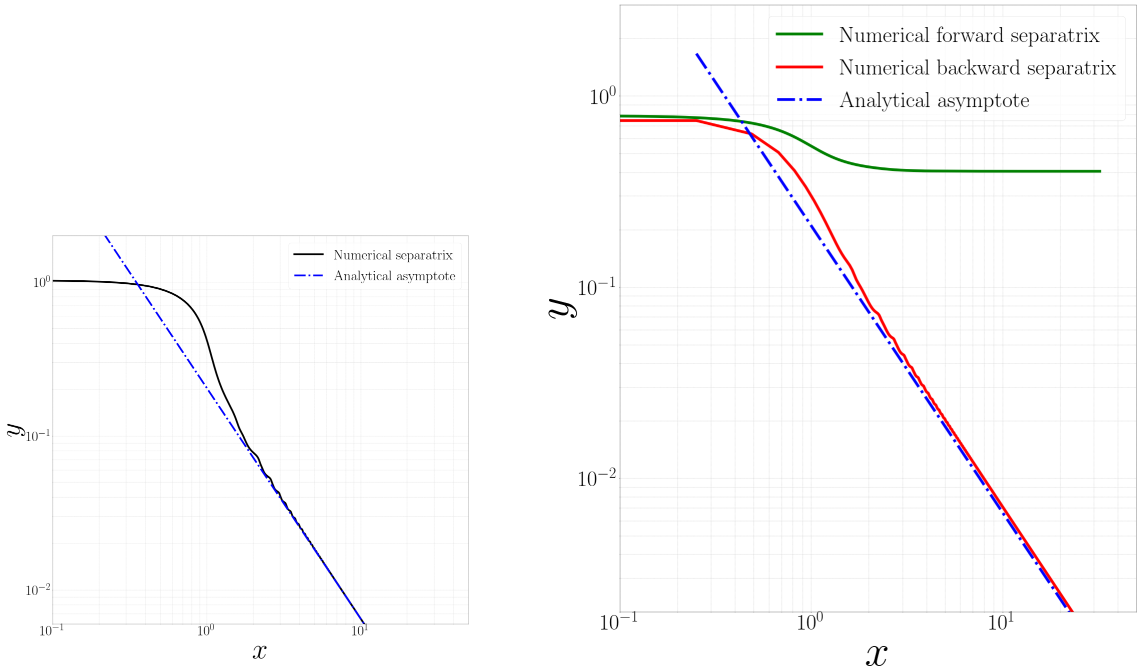

(a) Prolate-$\phi_{j0} = \pi/2$ (b) Prolate-$\phi_{j0} = \pi/3$

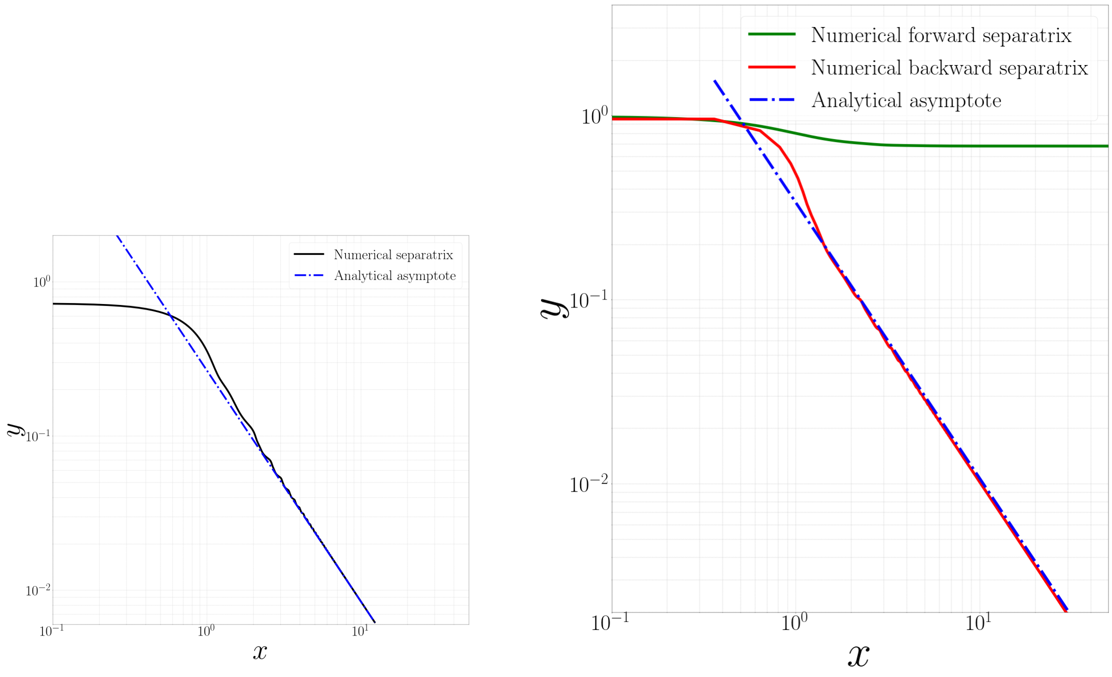

(c) Oblate-$\phi_{j0} = \pi/2$ (d) Oblate-$\phi_{j0} = \pi/6$

Fig. 2.11 Comparison between the numerical and analytical separatrix branches for a tumbling prolate spheroid with $\xi_0 = 1.15(\kappa = 2.025)$: (a) $\phi_{j0} = \pi/2$ (fore-aft symmetric) (b) $\phi_{j0} = \pi/3$(fore-aft asymmetric) and for an oblate spheroid with $\xi = 1.15(\kappa = 0.49)$:(c) $\phi_{j0} = \pi/2$(fore-aft symmetric) (d) $\phi_{j0} = \pi/6$(fore-aft asymmetric).

Chapter 3

Spheroid in a simple shear flow: The singular pathlines

Thus far, we have dealt with the regular open pathlines, which are (except for $\phi_{j0} = 0, \pi/2$) fore-aft asymmetric generalizations of the open streamlines around a sphere. That these do not constitute the entire set of pathlines may be seen from the fact that all of the in-plane separatrices in figure 2.5 intersect the gradient axis at an ordinate value (say, ${y_0}^{sep}$) greater than y_{min}, the value corresponding to the intersection of the spheroid surface with $x = 0$; the y_{min} value depends on ϕ_{j0}, and ranges between $\bar{\xi}_0/\xi_0$ and unity, these limiting values corresponding to flow and gradient-aligned prolate spheroids, respectively. In-plane pathlines spanning the interval $(y_{min}, {y_0}^{sep})$ have therefore not been accounted for; a similar argument may be made for the off-plane pathlines. The pathlines in these intervals are the analogs of closed streamlines for the sphere case, and the naive expectation is perhaps that the strictly periodic closed streamlines for a sphere would transform to aperiodic but bounded pathlines for a non-spinning spheroid. Interestingly, as will be seen below, this is not the case.

To examine pathlines in the interval $(y_{min}, {y_0}^{sep})$, we consider the case $\phi_{j0} = \pi/2(y_{min} = 1)$. The regular (in-plane) pathline configuration analogous to that shown in figure 2.5, but for a prolate spheroid with $\xi_0 = 2(\kappa = 1.15)$, is shown in figure 3.1a. The regular pathlines are bounded below by a fore-aft symmetric separatrix that asymptotes to the flow axis at upstream and downstream infinity, and intersects the gradient axis at ${y_0}^{sep} \approx 1.11621$. As seen in figures 3.1b-e, the pathlines 'below' the separatrix that intersect the gradient axis in the interval $(1, {y_0}^{sep})$ are again open, in that they eventually asymptote to finite y values in the upstream and downstream directions, but loop around the spheroid a certain number of times before doing so. Importantly, there appears to be no pattern to the number of loops; this number varies in a seemingly random (but sensitive) fashion as y_0 is decreased below ${y_0}^{sep}$ even by a very small amount. For instance, the number of loops for the pathlines in figure 3.1b is 1 and in 3.1c it is 2, but that in figure 3.1d is 23, while that in figure 3.1e is again 2; the dramatic increase in the number of loops in figure 3.1d occurs despite a change in y_0 that is $O(10^{-5})$! The fact that the pathlines crossing the gradient axis below the separatrix nevertheless asymptote to finite gradient offsets at upstream and downstream infinity obviously implies a crossing of the separatrix at some point. This crossing does not violate uniqueness since the spheroid orientation, at the time of crossing, is different for the separatrix and any of these looped trajectories (which we term the singular open pathlines); an argument along the same lines also shows that such looped trajectories, asymptoting to different upstream and downstream gradient offsets, is not inconsistent with the reversibility of the Stokes equations either.

3.1 The residence time distributions

To characterize this seemingly random dependence of the number of loops of the pathlines above, we define an appropriate residence time ($\mathcal{D}t$), taken to be the total time that a fluid element spends in a certain neighbourhood of the spheroid. Unless otherwise specified, this neighbourhood is taken to be the x-interval $(-20, 20)$ in the figures to follow; the qualitative nature of the findings reported below is independent of the particular choice of neighbourhood, provided the x-value chosen is large enough compared to the spheroid dimensions. Figures 3.2a and 3.2b depict the variation in the residence time defined above. The residence times are plotted as a function of y_0, over a range that brackets y_0^{sep}, for both a tumbling prolate spheroid (with $\phi_{j0} = \pi/2$) and a spinning one. In the former case, we see a discontinuous change in the nature of the residence time curve as one moves across the separatrix. $\mathcal{D}t$ exhibits an initial smooth increase for the regular pathlines corresponding to $y_0 > y_0^{sep}$, but there is an abrupt transition to a seemingly random dependence for the singular pathlines with $y_0 < y_0^{sep}$. Figure 3.2b shows the analogous residence time plot for the spinning spheroid, in which case the residence time varies in a smooth manner with y_0, attaining a maximum at the closed streamline(corresponding to y_0' in the inset) that exactly spans the x-interval under consideration. The subsequent decrease for $y_0 < y_0'$ corresponds to choosing $\mathcal{D}t$ as half the period of the closed streamlines that no longer span the chosen x-interval, but instead intersect the flow axis at a pair of points, within the interval (-20,20), and symmetrically placed about the origin.

We now examine the irregular variation of the residence time encountered in figure 3.2a in greater detail. For this purpose, we consider the same spheroid as in Figure 3.1, again in its tumbling orbit ($\theta_j = \pi/2$). The consideration of such a spheroid with an aspect ratio near unity (ξ_0=2; $\kappa = 1.15$) serves the additional purpose of illustrating the singular nature of the spherical particle limit from the perspective of the streamline/pathline topology. Figure 3.3a shows the variation of the residence time of the singular open pathlines which pass through the negative x-axis within the interval $x_0 \in (-9.5, -3)$. The residence time is obtained in the manner defined above, via forward and backward time integrations starting from a specific initial point in the aforementioned interval, and until the pathline leaves the interval (-20,20). Similar to figure 3.2a, the extremely irregular dependence of the residence time on x_0 is readily apparent (note that each of the pathlines intersects the x-axis multiple times, and in principle, it is possible that a pair of chosen initial conditions end up being part of the same singular pathline, although this should, in principle, occur with an infinitesimal probability; we have verified that this is not the case by monitoring the upstream and downstream coordinates, and ensuring that these are different for each of the initial points chosen). The plots that follow in figures 3.3b-e show the variation in the residence time at progressively finer resolutions by focussing on increasingly small subsets of the x_0-interval considered above. These figures correspond to 1000 initial conditions in the x_0-intervals (-4,-3), (-3.1,-3), (-3.01,3) and (-3.001,3), respectively. Thus, in going from figure 3.3a to e, the length scale of the interval under consideration has decreased by four orders of magnitude, but the irregular dependence of the residence time clearly persists down to the smallest scales. This fractal dependence of the residence time measure is a signature of chaotic scattering, and is suggestive of the existence of a chaotic saddle in the region around the spheroid[16, 15, 7–9, 41]. The chaotic saddle above includes an infinite number of unstable periodic orbits (and bounded aperiodic ones), whose

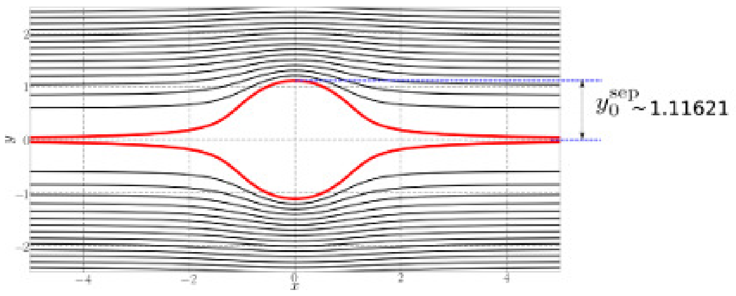

(a)

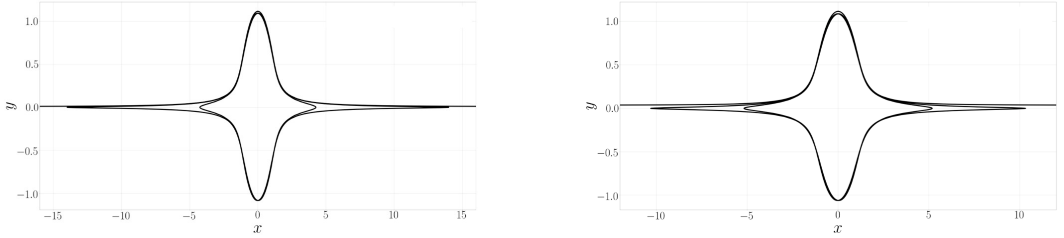

(b) $y_0 = y_0^{\rm sep} - 10^{-5}$

(c) $y_0 = y_0^{\rm sep} - 4 \times 10^{-5}$

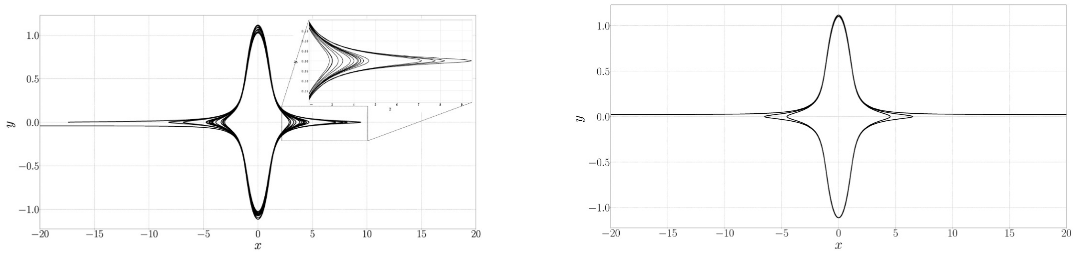

(d) $y_0 = y_0^{\rm sep} - 10 \times 10^{-5}$

(e) $y_0 = y_0^{\rm sep} - 20 \times 10^{-5}$

Fig. 3.1 The open pathline configuration for a tumbling prolate spheroid ($\xi 0 = 2.0 (\kappa = 1.15)$) with $\phi_{j0} = \pi/2$. (b)-(e) correspond to singular open pathlines that cross the gradient axis just below the separatrix(shown in red, with $y_0 = y_0^{\rm sep}$) at four different y_0's.

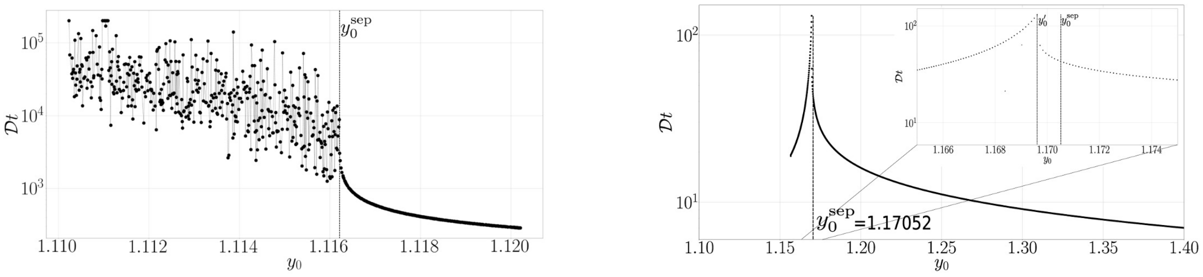

(a) Tumbling

(b) Spinning

Fig. 3.2 Variation of the residence time of a fluid element for a prolate spheroid($\xi_0 = 2.0 (\kappa = 1.15)$): (a) in the tumbling orbit with $\phi_{j0} = \pi/2$, (b) in the spinning mode; the ordinate of the separatrix y_0^{sep} is shown by the dashed line; y_0' corresponds to the closed orbit spanning the x-interval $(-20, 20)$.

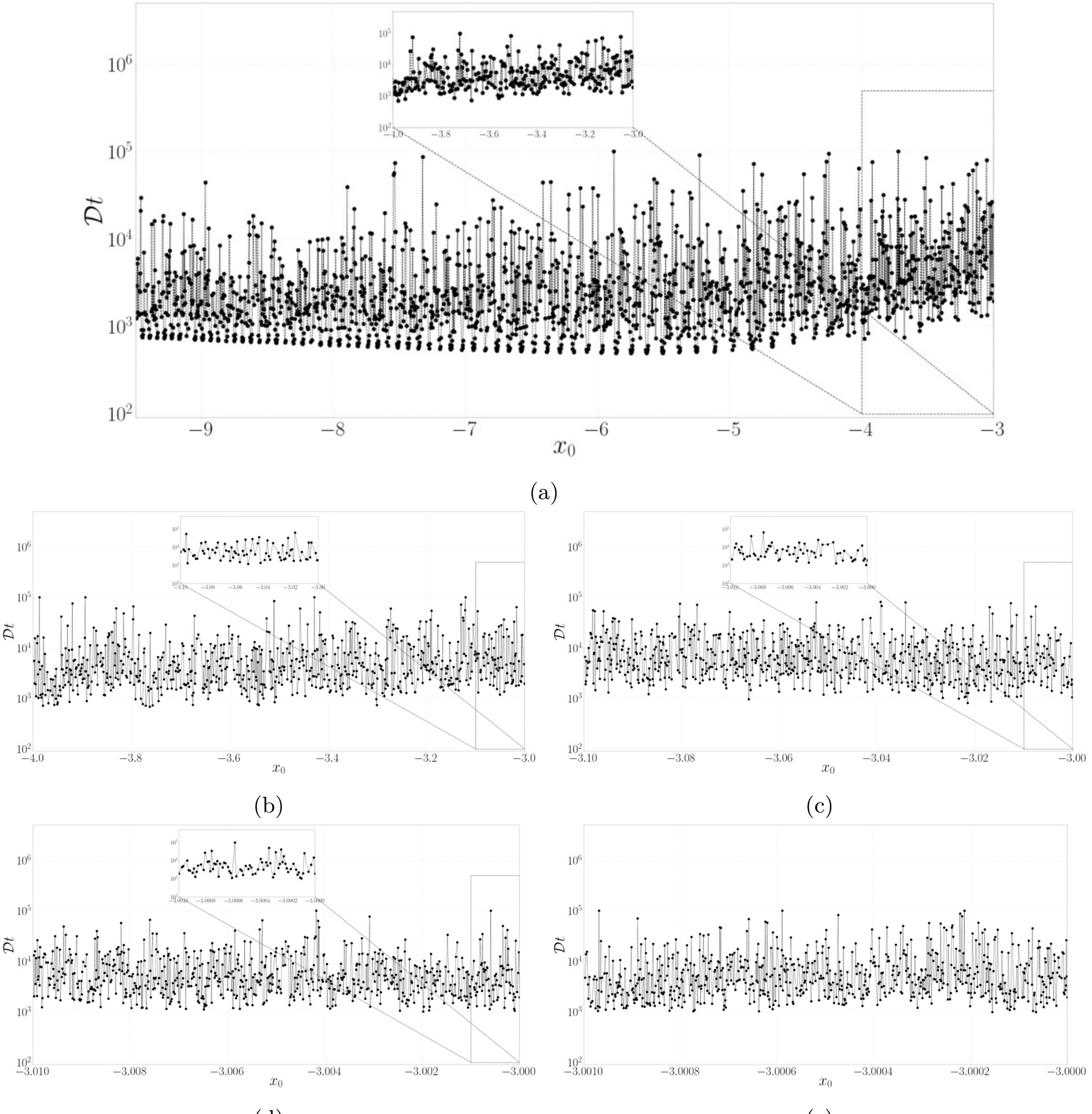

(a)

(b)

(c)

(d)

(e)

Fig. 3.3 The sensitive dependence of the residence time of a fluid element, for a tumbling prolate spheroid ($\xi_0 = 2.0(\kappa = 1.13)$) with $\phi_{j0} = 0$, plotted as a function of the 'initial condition' (defined as a point on the negative x-axis). Figure (a) depicts the dependence in the entire interval (-9.5,-3), while figures (b)-(e) show the dependence of the residence time in the intervals (-4,-3), (-3.1,3), (-3.01,3) and (-3.001,3), respectively.

stable and unstable manifolds intersect to form a Cantor-like set. The existence of single-looped periodic orbits may, for instance, be inferred by considering two neighbouring pathlines, integrated over the approximate duration of a single loop, as shown in figures 3.4a and b. The pair of initial points in the figures correspond to $x_0 = -3.2217088$ and $x_0 = -3.2214089$ on the negative x-axis, and one observes the subsequent intersections with the (negative) x-axis to occur opposite sides of the initial point in the two cases, implying that the pair of pathlines shown bracket a single-loop closed orbit between them. This argument may be extended in an obvious manner to show the existence of closed pathlines with multiple loops.

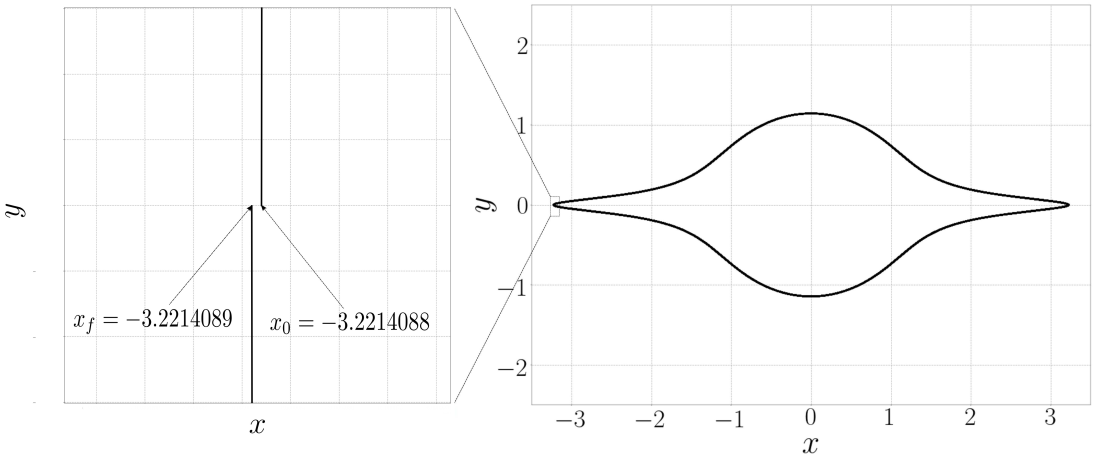

(a) $x_0 = -3.2214088$

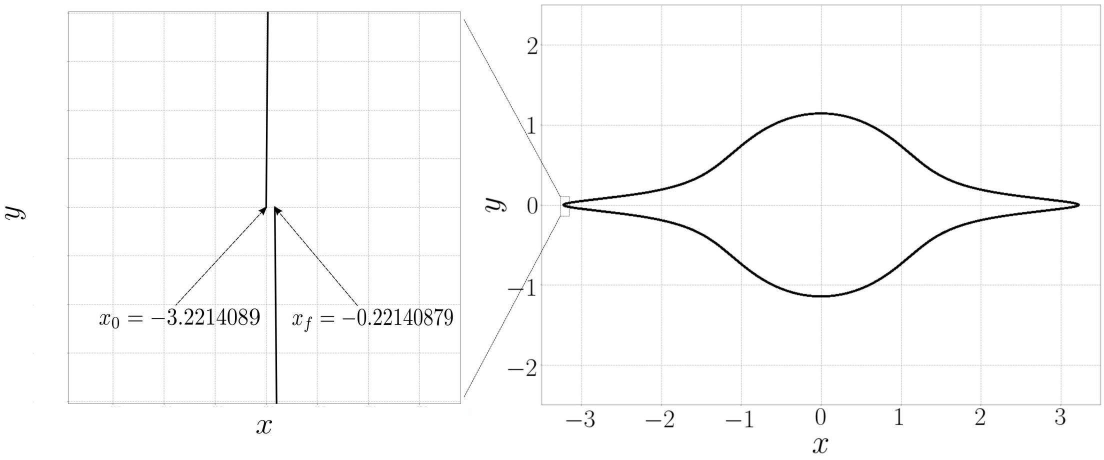

(b) $x_0 = -3.2214089$

Fig. 3.4 Existence of periodic pathlines for the tumbling prolate spheroid($\xi_0 = 4.0(\kappa = 1.03)$- a single-loop periodic orbit with an approximate period of $40T_j$: (a) final point displaced to the right of the initial point $(-3.2214088, 0)$ and (b) final point displaced to the left of the initial point $(-3.2214089, 0)$.

Having established the signatures of chaotic scattering in the residence time plot for a tumbling spheroid, in figures 3.5a-d, we consider analogous residence time plots for the spheroid in other finite-C precessional orbits. The spheroid is the same as that in figure 3.3, and the orbits chosen correspond to $C = \infty$(already shown), 5, 0.5, 0.1 and 0.05, respectively, with the initial point again restricted to the interval (-9.5,-3) on the negative x-axis. The plots appear to show a progressive decrease in the extent of irregularity with decreasing C. One reason for this decrease is that, for lower C's, there appear regular intervals between those that correspond to chaotic scattering, and this interlacing behavior will be seen in more detail in the next section; note that this interlacing tendency is, in fact, already present for $C = \infty$, although not evident owing to the much smaller scale (see the inset of figure 3.5a which presents a magnified view). The decrease in irregularity is also because, for the smaller C's, an increasing fraction of pathlines do not open for the duration of the numerical integration($t_{max} = 8000T_j$); examples of such bounded pathlines are shown in figures 3.5d and e. Such bounded pathlines, arising as an artifact of the finite integration duration, begin to populate an upper horizontal plateau with residence times equal to the maximum integration time; in fact, figure 18(d) for $C = 0.05$ consists entirely of pathlines that do not open over the duration of the integration. However, as shown in figure 3.6, the fraction of initial conditions leading to bounded pathlines for the case $C = 0.2$ decreases perceptibly for an integration duration ($t_{max} = 32000T_j$) four times the one chosen for figure 3.5. Thus, the fraction of bounded pathlines appears to depend on the duration of the numerical integration. Although impossible to ascertain by numerical means, the limiting integrable case of a spinning spheroid ($C = 0$) is a singular one, with a spheroid rotating in an orbit with C small but finite nevertheless leading to chaotic scattering; the associated large residence times are, however, inaccessible to numerics.

3.1.1 Local graphs of the invariant manifolds and the chaotic saddle

Graphical representations of the unstable and stable manifolds of the chaotic saddle are another qualitative signature of chaos. Here, we numerically evolve an initially circular blob of 'dye' [44] located along the negative x-axis on account of being advected by the fluid motion induced by the rotating spheroid. A forward integration in time must trace out the unstable manifold of the chaotic saddle for sufficiently long times, while a backward-in-time integration of the equations yields the stable manifold. Figure 3.7 compares the evolution of the aforementioned circular blob (made up of 10^6 randomly distributed initial points) for a sphere and for a (nearly spherical) prolate spheroid with $\xi_0 = 4(\kappa = 1.03)$; the spheroid is chosen to rotate in a Jeffery orbit with $C = 20(\phi_{j0} = 0)$. Figure 3.7a and b show that the blob for the case of a sphere, although significantly distorted for large times owing to differential convection, has, nevertheless a finite spatial extent - the distorted blob lies within the interval (-6,6) for all time. This is because the initial blob has been chosen to lie entirely within the region of closed streamlines, and is therefore always bounded by the largest closed streamline that passes through one of the initial points on its periphery. In contrast, figures 3.7c and d show that the blob, for a spheroid, is sheared out to arbitrarily large distances in the flow direction as time goes to plus and minus infinity on account of the singular open pathlines discussed above (note the differing horizontal scales in figures 3.7a and b, and in figures 3.7c and d). While figure 3.7 highlights the singular role of non-sphericity with regard to the long-time temporal evolution of a blob, which in turn has implications for the rate of mass/heat transport from the spheroid(see conclusions section), it is figure 3.8 that highlights the striking differences between the sphere and spheroid cases even for finite times. The magnified views in figure 3.8 clearly show the fine-scaled features(wiggles) that emerge in the evolving blob, only for the spheroid, on account of the convoluted nature of the underlying unstable manifold of the chaotic saddle. In fact, in figure 3.8f, the initial distribution of points has been sheared out to an extent that the small-scale wiggles associated with the underlying chaotic saddle are no longer well resolved.

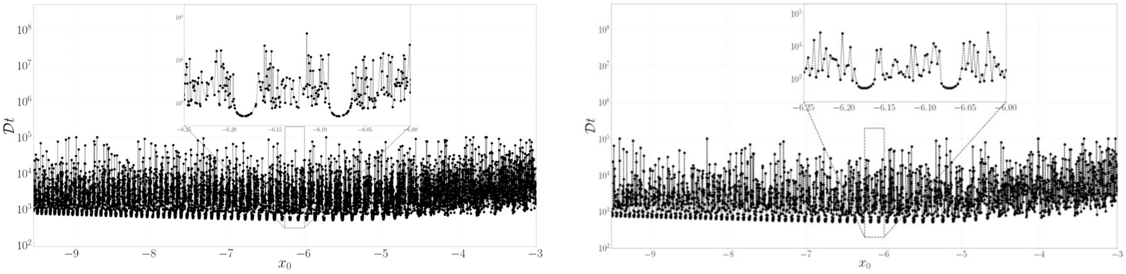

(a) $C = \infty$

(b) $C = 5.0$

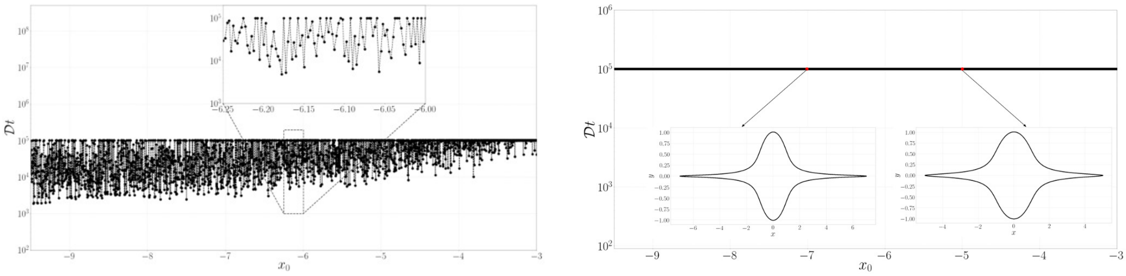

(c) $C = 0.5$

(d) $C = 0.05$

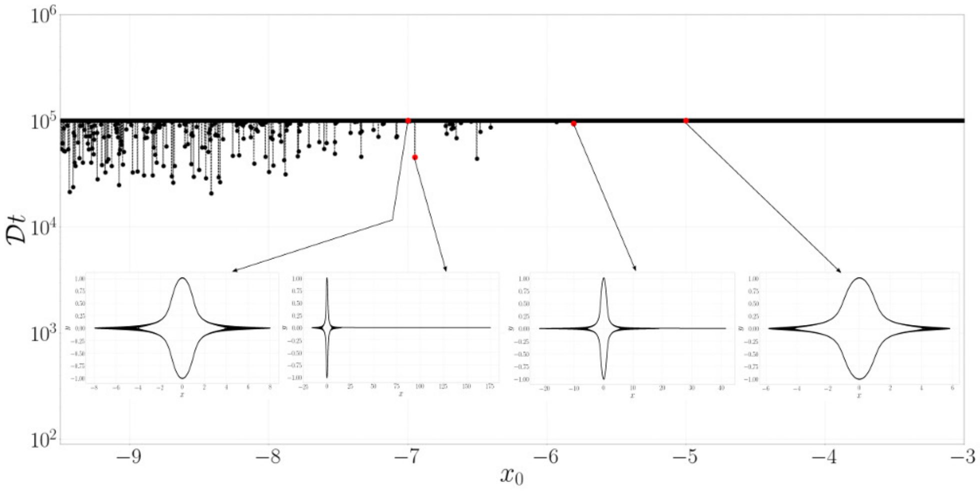

(e) $C = 0.2$

Fig. 3.5 Sensitive dependence of the residence time of fluid pathlines, on initial conditions, for a prolate spheroid($\xi_0 = 2.0(\kappa = 1.13)$) in finite-$C$ precessional orbits (a) $C = \infty$, (b) $C = 5.0$, (c) $C = 0.5$, (d) $C = 0.05$ and (e) $C = 0.2$. The insets in figure 18e shows that the highest residence times (plateau points) correspond to bounded pathlines, while those off the plateau lead to pathlines that open up over times shorter than the integration time($8000T_j$); the insets in 18d confirm that all of the pathlines for this case are bounded.

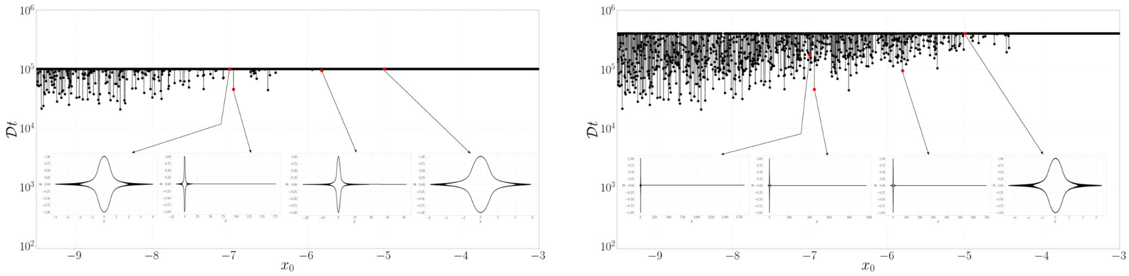

(a) $t_{max} = 8000T_j$ (b) $t_{max} = 32000T_j$

Fig. 3.6 The residence time of fluid pathlinse for a prolate spheroid($\xi_0 = 2(\kappa = 1.13)$), in Jeffery orbit corresponding to $C = 0.2$, for two different integration times: (a) $t_{max} = 8000T_j$, (b) $t_{max} = 32000T_j$. The fraction of singular open pathlines increases significantly for $t_{max} = 32000T_j$; sample pathlines are shown for points on the plateau as well as for ones off it.

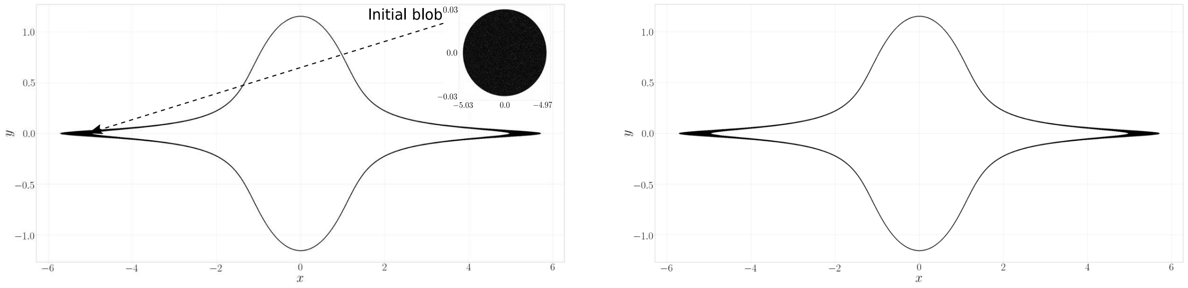

(a) $t = 2000T_j$ (b) $t = -2000T_j$

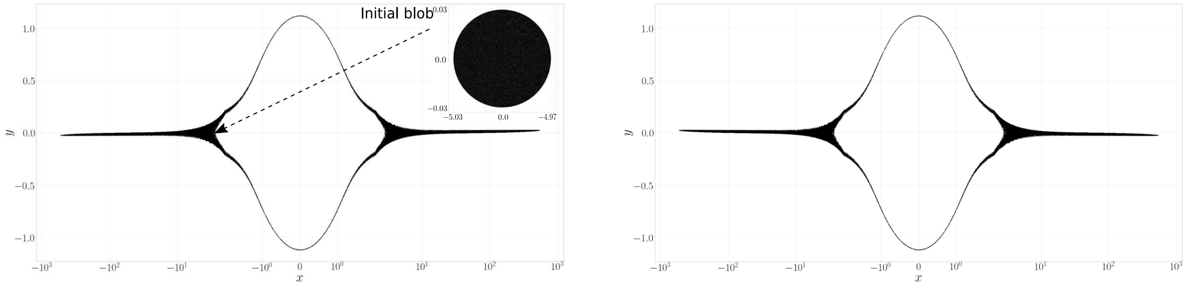

(c) $t = 2000T_j$ (d) $t = -2000T_j$

Fig. 3.7 The evolution of an initially circular blob of radius = 0.03, located at (-5,0,0)(shown in the inset) for a sphere and a prolate spheroid with $\kappa = 1.03(\xi_0 = 4.0)$ rotating in a Jeffery orbit with $C = 20$: (a,c)forward integration (b,d)backward integration.

Figure 3.9 shows evolving blobs for spheroids of different aspect ratios, and here, the scale of the aforementioned wiggles is seen to becomes larger with increasing aspect ratio. Further, the horizontal extent of the sheared blob, for large times, also increases substantially for high aspect ratio spheroids, implying a decrease in the 'loopiness' of the singular open pathlines. In the next section we will see a similar behavior emerge from a different perspective, wherein the dependence of the residence time (of fluid pathlines) is analyzed from the point of view of an 'impact parameter', defined as the gradient and/or vorticity coordinates of a fluid element far upstream.

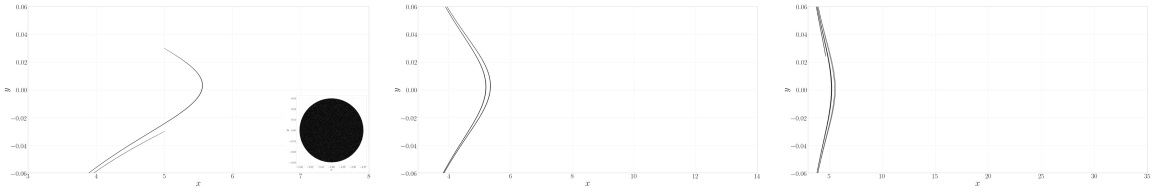

(a) $t = 50T_j$ (b) $t = 68T_j$ (c) $t = 200T_j$

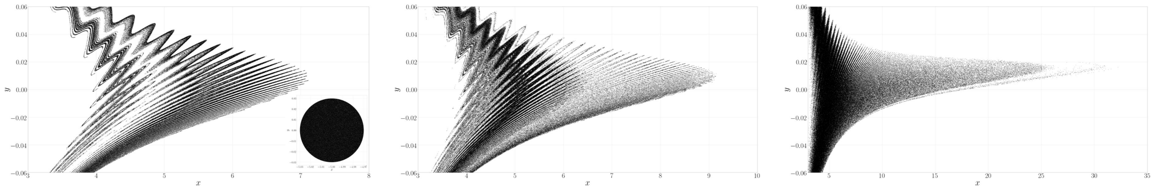

(d) $t = 50T_j$ (e) $t = 68T_j$ (f) $t = 200T_j$

Fig. 3.8 A comparison of the evolution of an initially circular blob for a sphere and a prolate spheroid ($\xi_0 = 4(\kappa = 1.03)$) in a precessional orbit with $C = 20$. The evolving blob, for the spheroid, traces out the unstable manifold, of the underlying chaotic saddle, for large times.

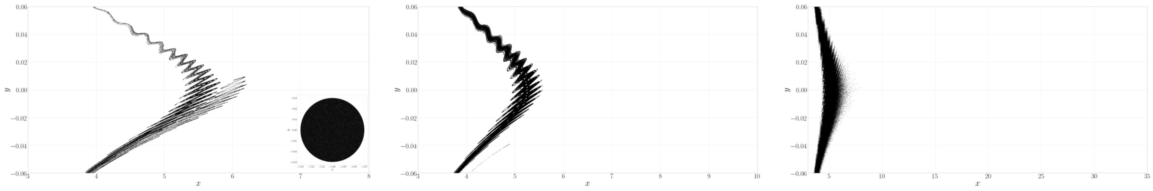

(a) $t = 50T_j$ (b) $t = 68T_j$ (c) $t = 200T_j$

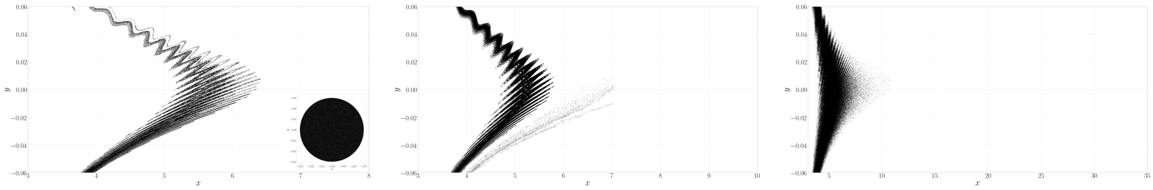

(d) $t = 50T_j$ (e) $t = 68T_j$ (f) $t = 200T_j$

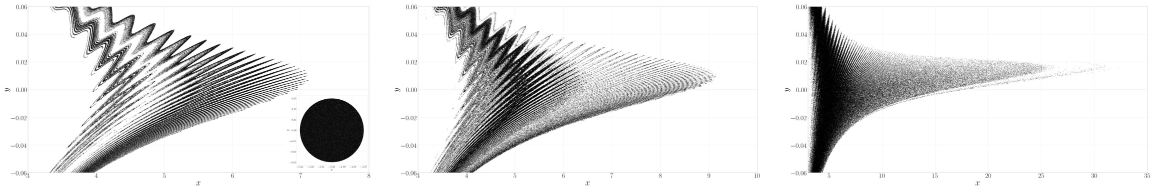

(g) $t = 50T_j$ (h) $t = 68T_j$ (i) $t = 200T_j$

Fig. 3.9 A comparison of evolving blobs for prolate spheroids in a precessional orbit with $C = 20$:(a,b,c)$\xi_0 = 8.0(\kappa = 1.008)$, (d,e,f)$\xi_0 = 6.0(\kappa = 1.01)$ and (g,h,i)$\xi_0 = 4.0(\kappa = 1.03)$. The scale of the wiggles, and the horizontal spread of the distorted blob, increase with increasing aspect ratio.

Finally, in Figure 3.10, we give a representation of the invariant chaotic saddle, its projection onto the flow-gradient plane and in the neighborhood of the rotating spheroid, obtained in the following manner. The representation corresponds to a near-sphere, with $\xi_0 = 4(\kappa = 1.03)$, and it therefore makes sense to relate this representation to an invariant set for a sphere; an example of the latter is a region contained within any of the closed streamlines. With this in mind, we initialize 34 million fluid elements uniformly distributed in a rectangular domain spanning the intervals (-5,5) and (-1,1) in the x and y-directions, and integrate these over a duration of $1000T_j$ both forward and backward in time. Those initial points that remain within a closed streamline that spans the interval (-5,5) are plotted in the said figure. The fine-scaled structure evident in Figure 3.10 is a representation of the invariant set responsible for the chaotic scattering signatures detailed above. Further, the emergent non-trivial foliated structure is also indicative of the singular nature of the spherical limit. For a sphere, the spatial extent of the initial distribution would have remained unchanged, since fluid elements within the chosen closed streamline remain so regardless of the duration of integration. Finally, note that Figure 3.10 denotes (approximately) the intersection of the saddle with the region inside the aforementioned closed streamline. As evident from figures 3.8 and 3.9, the saddle will also have a fine-scaled structure 'radiating' out of the closed streamline, but resolving this appears to require excessively long integration times.

3.1.2 The uncertainty dimension of the chaotic saddle

The chaotic saddle may be characterized quantitatively in terms of its fractal dimension. While there are quite a few ways by which one may obtain such a dimension, herein we adopt the methodology of [15] by determining the uncertainty dimension. In this method a large number(N_0) of initial conditions are chosen randomly, and each of these conditions is perturbed by a small amount (ϵ), and is marked uncertain if the corresponding output states are markedly different. In the present case, we choose 5000 pairs of original and ϵ-perturbed upstream gradient offsets in the interval $0 \leq y_{-\infty} < y_{-\infty}^{sep}$, with $x = -20$, $z_{-\infty} = 0$, and $\phi_{j,-\infty} = 0$, the latter corresponding to the spheroid phase, in a particular Jeffery orbit, at $x = -20$. We then check if the integrated pair of final states have similarly signed y-components, implying that both initial members of the chosen pair asymptote to either upstream (negative y) or downstream (positive y) infinity. If not, the pair is deemed uncertain, and one then calculates the uncertainty ratio as $f(\epsilon) = N/N_0$, N being the number of uncertain pairs. For the number of initial pairs chosen above, N is $O(10^3)$ even for the smallest ϵ's examined, ensuring statistical accuracy. Figures 3.11a and b show the variation of the uncertainty ratio with aspect ratio for tumbling prolate spheroids, and with orbit constant (C) for a given prolate spheroid with $\xi_0 = 1.05 (\kappa = 3.28)$, respectively. An algebraic scaling, $f(\epsilon) \sim \epsilon^{\alpha}$, for sufficiently small ϵ, is observed in all cases over the range of ϵ's examined (down to $O(10^{-8})$). The uncertainty dimension is then defined as $D_c = D - \alpha$, where we take $D = 3$ since fractality is only observed is along the gradient direction; in section 6, it is shown that the non-trivial interlacing of the regular and chaotic scattering intervals persists for all values of the vorticity coordinate. For a spinning spheroid, as already shown (see figure 3.2b) there is a unique value of the separatrix offset. For this case alone, one expects $f(\epsilon) \propto \epsilon$, so that $\alpha = 1$ and $D_c = 2$, consistent with the fact that the separatrix is a regular surface embedded in three dimensions. However, as already implied by the results in Figure 3.5, the spinning spheroid appears to be a singular limit, and this is reinforced by the results of Fig 3.11b, where D_c does not approach 2 even as C decreases to 0.01. Finally, it needs mention that despite the algebraic scaling obtained in Figure 3.11, as will be seen later, the probabilities densities of residence times show algebraic rather than the exponential tails familiar from much of the literature [16, 15, 52, 41, 39]. The implications of this finding are discussed briefly in the next section.

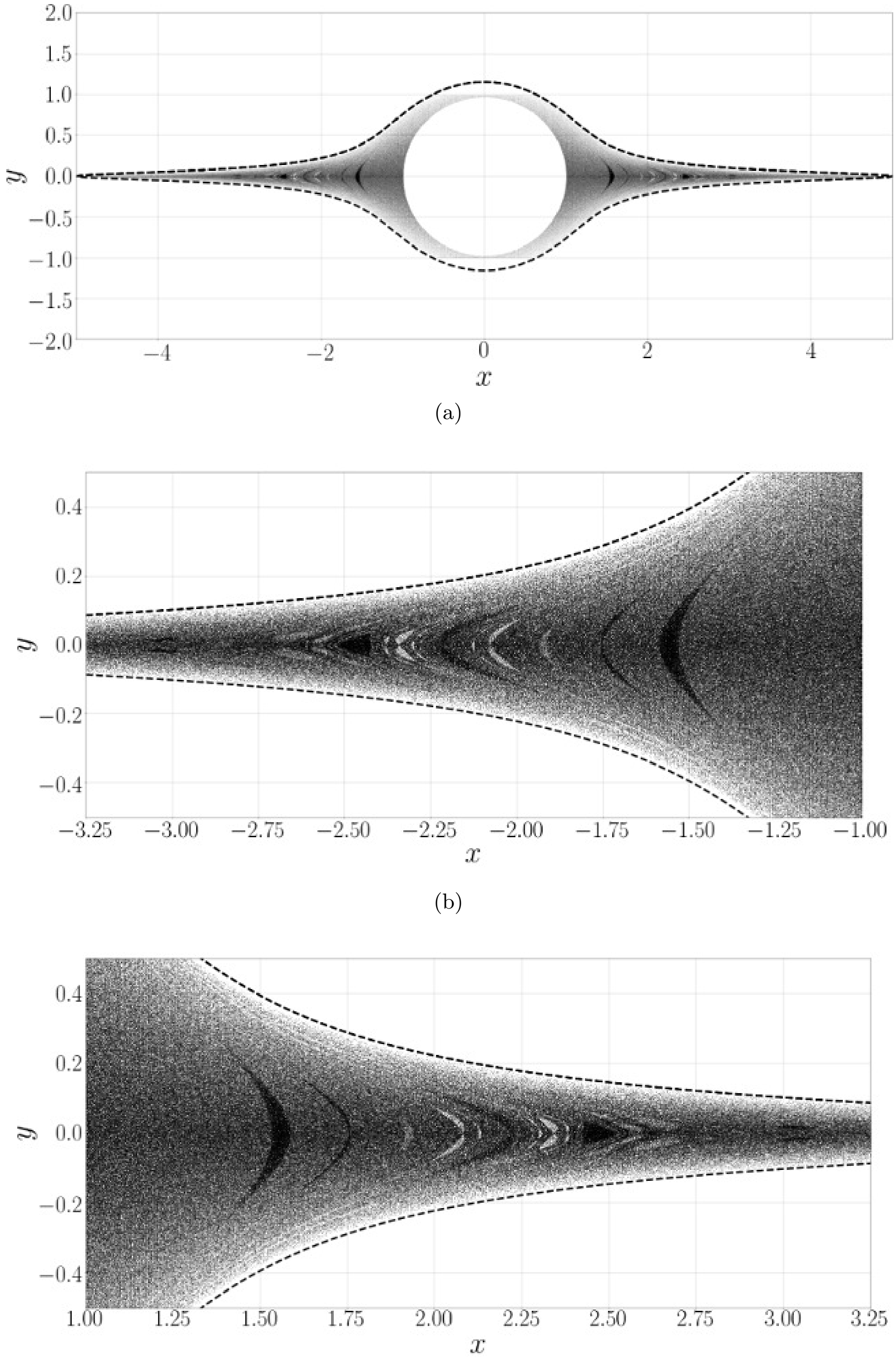

(a)

(b)

(c)

Fig. 3.10 A representation of the intersection of the invariant chaotic saddle with the region contained within a closed streamline (for a sphere); the graphs shown are for a prolate spheroid with $\xi_0 = 4(\kappa = 1.03)$ in a Jeffery orbit with $C = 20$: (a) Full view; (b) and (c) correspond to magnified views of the left and right hand portions. The dashed curve denotes the closed streamline of choice (note that the central part of the saddle is truncated at the top and bottom, being limited by the width of the initial rectangular region).

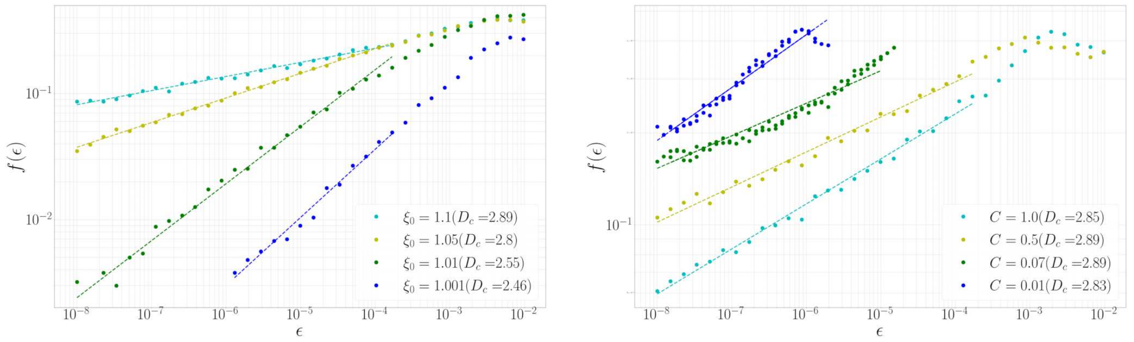

(a) (b)

Fig. 3.11 Plot of the uncertainty ratio $f(\epsilon)$ of the chaotic saddle for (a) prolate spheroids of different aspect ratios in the precessional orbit of C=20 and (b) a prolate spheroid of $\xi_0 = 1.05$ in different Jeffery orbits(C=0.01, 0.07, 0.5 and 1).

3.2 Transition from regular to chaotic pathlines: Boundary of the chaotic saddle

Having established the signatures of chaotic scattering for the fluid pathlines around any non-spinning spheroid, we now proceed to analyze the pathlines from the perspective used in earlier efforts(for instance, see [16, 15]). This is done by plotting the output variable, which is still the residence time, as a function of an appropriate input one, the focus being on the singular regions corresponding to apparent divergences of the residence time. Such regions would appear scale-dependent in a numerical investigation, on account of the true divergences being localized on a Cantor set of vanishing measure [54, 114, 98, 39]. The input variable must correspond to the analog of the impact parameter used in the chaotic scattering literature[15]. In our case, this is the upstream gradient offset($y_{-\infty}$) of a fluid element in the plane of shear; or, both the gradient and vorticity offsets ($y_{-\infty}$ and $z_{-\infty}$) of an element off the flow-gradient plane. In addition one, of course, needs to specify the particular Jeffery orbit, and the phase of rotation(within a given orbit) at the initial instant; the latter is again done via the azimuthal angle which is now denoted as $\phi_{j-\infty}$. Note that these upstream offsets have already been used to analyze the regular open pathlines above. The difference here is that the offsets are used as a common basis to analyze both the regular and singular pathlines; the latter group of pathlines was examined earlier, only as a function of their points of intersection with the flow axis, in order to establish the signatures associated with chaotic scattering. One may now analyze the transition from the regular to the singular open pathlines, as a function of the aforementioned upstream offsets, and thereby, analyze the boundary of the chaotic saddle (what has been termed 'the edge of chaos' in the literature; see [98]). The latter has been the subject of earlier investigations in the context of two-dimensional Hamiltonian problems[55].

In figures 3.12 and 3.13 we plot the residence time as a function of $y_{-\infty}(z_{-\infty} = 0)$ for tumbling prolate spheroids with $\xi_0 = 2.0(\kappa = 1.13)$ and $\xi_0 = 1.05(\kappa = 3.28)$, respectively; $\phi_{j,-\infty} = 0$ for both cases. The residence time curves exhibit a small-scale modulation superposed on an underlying monotonic increase with decreasing $y_{-\infty}$. The reason for the latter increase is obvious. The modulation leading to a non-monotonic dependence on $y_{-\infty}$ arises owing to the spheroid orientation being a function of time. For $y_{-\infty}$'s not too different, a fluid element crossing the gradient-vorticity plane, at the instant that the spheroid is close to a vertical orientation, will do so at a higher y_0, leading to a reduced residence time. With decreasing $y_{-\infty}$, the residence time, for a given change in $y_{-\infty}$, changes by a greater amount relative to the fixed Jeffery period. This leads to the wavelength of the modulation in Figures 3.12 and 3.13(and the ones thereafter) decreasing with $y_{-\infty}$. Note that the absolute wavelength scales in proportion to the Jeffery period, and is therefore greater for the larger aspect ratio spheroid ($\xi_0 = 1.05$). The red vertical line in each plot denotes the ordinate of the separatrix ($y_{-\infty}^{sep}$) that demarcates the regular regions from those that exhibit intervals of chaotic scattering; this demarcation is evident from the magnified views in figures 3.12b and 3.13b, which clearly contrast the smooth peak(s) for $y_{-\infty} > y_{-\infty}^{sep}$ with the irregular dependence that ensues for $y < y_{-\infty}^{sep}$. Note that it is $\phi_{j,-\infty}$ that is now fixed at 0, and the value of ϕ_{j0} emerges during the course of the integration; one finds $\phi_{j0} = 111.8^o$ and 168.6^o for the separatices corresponding to $\xi_0 = 2.0$ and $\xi_0 = 1.05$, respectively. Thus, the separatrices marked by the red vertical lines in figures 3.12 and 3.13 correspond to fore-aft asymmetric separatrices with finite upstream offsets - keeping in mind the pathline configurations in Figure 7, these separatrices correspond to $\phi_{j0} \in (\pi/2, \pi)$, and are obtained from those in Figure 7 by reflecting about the gradient axis. Similar to Figure 3.2a, the dependence for $y_{-\infty}$'s less than $y_{-\infty}^{sep}$ isn't entirely irregular. Instead, there are intervals of regular dependence separated by chaotic 'bursts', with the relative sizes of the regular and chaotic intervals being clearly sensitive to the aspect ratio. Figures 3.12b,c and 3.13 b,c correspond to magnified views, with each view corresponding to 10^4 initial conditions ($y_{-\infty}$'s), and highlight the interlacing of regular and chaotic intervals down to the smallest (numerically) resolved scales; in other words, what appears as an interval of chaotic dependence at a given coarse resolution contains smaller intervals of regular intervals within, and this appears to continue ad infinitum. Figures 3.12c and 3.13c suggest qualitatively different transitions from regular to chaotic scattering for the two aspect ratios. The transition for the spheroid with a near-unity aspect ratio($\xi_0 = 2$) in Figure 3.12c appears to be discontinuous, with $\mathcal{D}t$ approaching a finite limit for $y_{-\infty} \to y_{-\infty}^{sep+}$, but appearing to diverge for $y_{-\infty} \to y_{-\infty}^{sep-}$; in contrast, the transition for the larger aspect ratio spheroid appears to involve a divergence of the residence time regardless of the direction of approach towards the separatrix offset. Despite this difference in appearance, one expects $\lim_{y_{-\infty} \to y_{-\infty}^{sep+}} \mathcal{D}t$ to be finite, since this corresponds to the finite residence times of the fore-aft asymmetric separatrices mentioned above in the interval (-20,20).

The separatrix offsets in Figures 3.12 and 3.13 arise for $\phi_{j,-\infty} = 0$. A different offset will result for another choice of $\phi_{j,-\infty}$. To access all possible separatrices, one needs to choose $\phi_{j,-\infty}$'s spanning the interval $(0, \pi)$ for a given large negative x. The maximum among all such separatrix offsets would then determine the onset of chaotic scattering in the flow-gradient plane. The restriction of a large negative x is necessary so that the aforementioned maximum separatrix offset is independent of x; although, this maximum will occur at an x-dependent $\phi_{j,-\infty}$. Thus, in other to characterize the onset of chaotic scattering in the flow-gradient plane, one ought to have a plot, as depicted in Figure 3.14, of the residence-time surface as a function of both $y_{-\infty}$ and $\phi_{j,-\infty}$. The onset of chaotic scattering is demarcated by a critical curve $y_{-\infty}^{sep}(\phi_{j,-\infty})$ in this plane. The residence-time surface is smooth on one side of this separatrix curve, but one expects a jagged irregular distribution of peaks on the other side; the latter irregular dependence has indeed been observed in the context of the laminar-turbulent transition[39]. Note that, provided x is sufficiently large, the set of $y_{-\infty}^{sep}$ values is invariant to a change in x. Instead, and as mentioned above, each $y_{-\infty}^{sep}$ now corresponds to a different $\phi_{j,-\infty}$, the relation between the two $\phi_{j,-\infty}$'s being determined by the angle through which the spheroid rotates as the fluid element translates from the first to the second value of x (this translation is almost entirely due to the ambient simple shear). This 'juggling' of $y_{-\infty}^{sep}$'s will, of course, change the separatrix curve in the

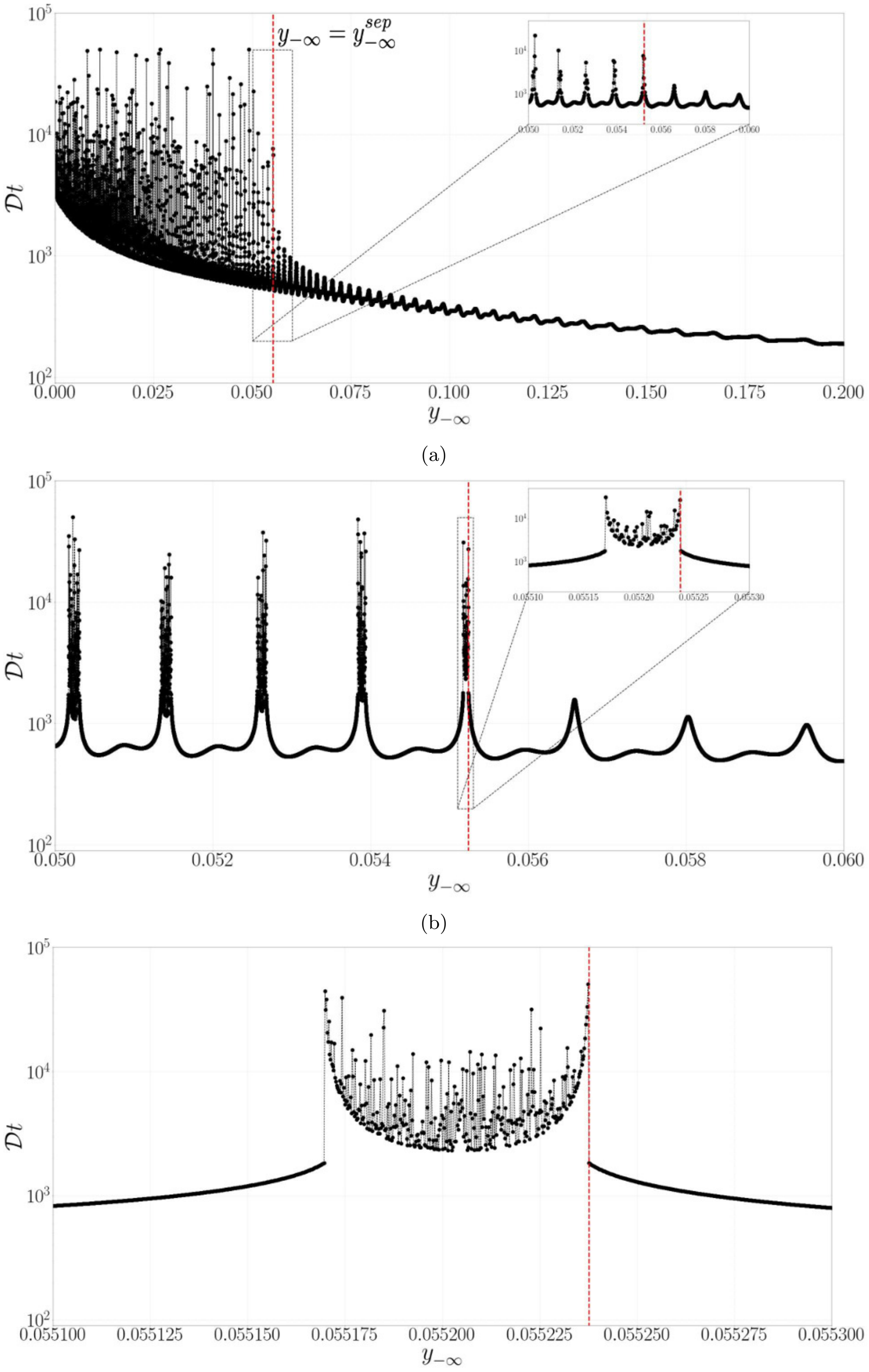

(a)

(b)

(c)

Fig. 3.12 Variation of the residence time for a tumbling prolate spheroid($\xi_0 = 2.0(\kappa = 1.13)$), with $\phi_{j,-\infty} = 0$, as a function of the upstream gradient offset of the fluid pathline ('upstream' here corresponds to $x = -20$). The red vertical line in all figures denotes the separatrix($y_{-\infty}^{sep}$) that separates the regular($y_{-\infty} > y_{-\infty}^{sep}$) region from the one that includes intervals of chaotic scattering($y_{-\infty} < y_{-\infty}^{sep}$).

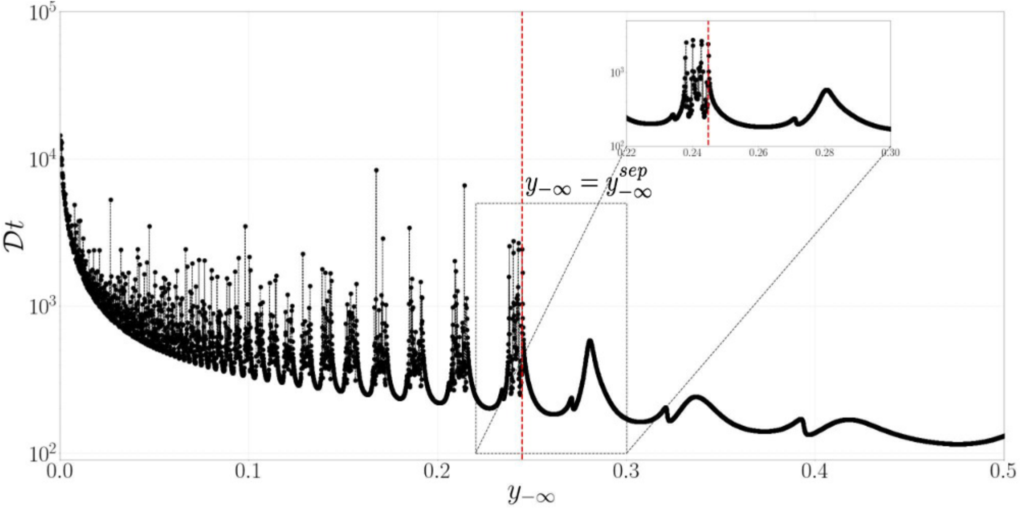

(a)

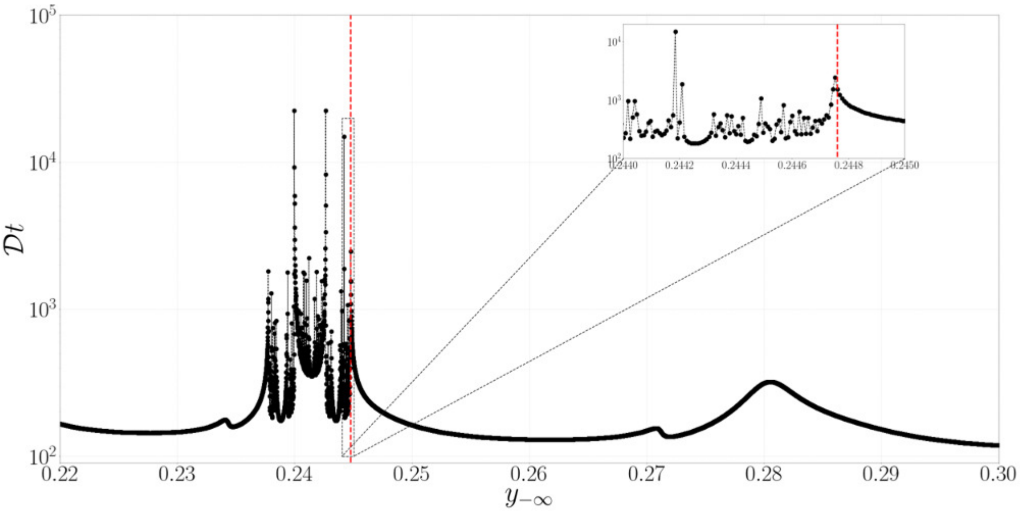

(b)

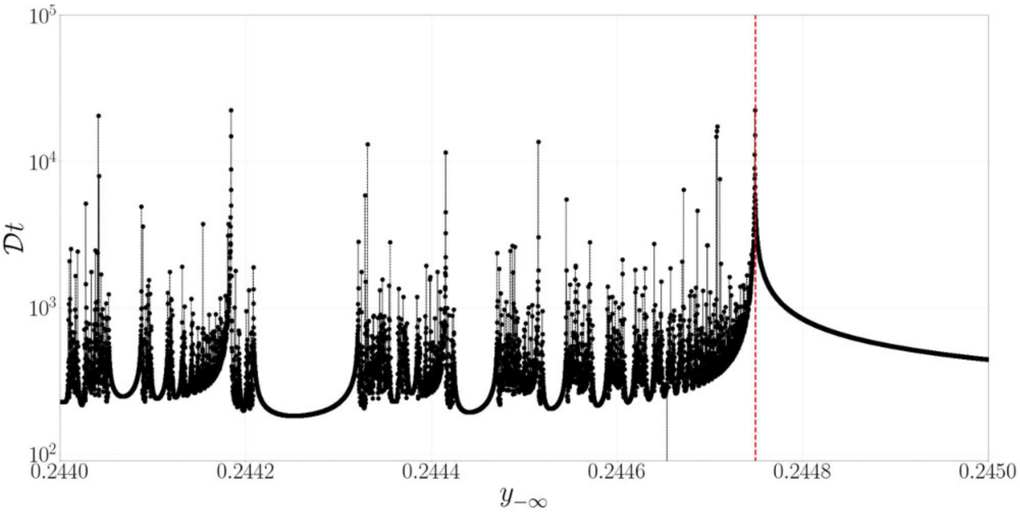

(c)

Fig. 3.13 Variation of the residence time for a tumbling prolate spheroid($\xi_0 = 1.05(\kappa = 3.28)$), with $\phi_{j,-\infty} = 0$, as a function of the upstream gradient offset of the fluid pathline ('upstream' here corresponds to $x = -20$). The red vertical line in all figures denotes separatrix($y_{-\infty}^{sep}$) that separates the regular($y_{-\infty} > y_{-\infty}^{sep}$) region from the one that includes intervals of chaotic scattering($y_{-\infty} < y_{-\infty}^{sep}$).

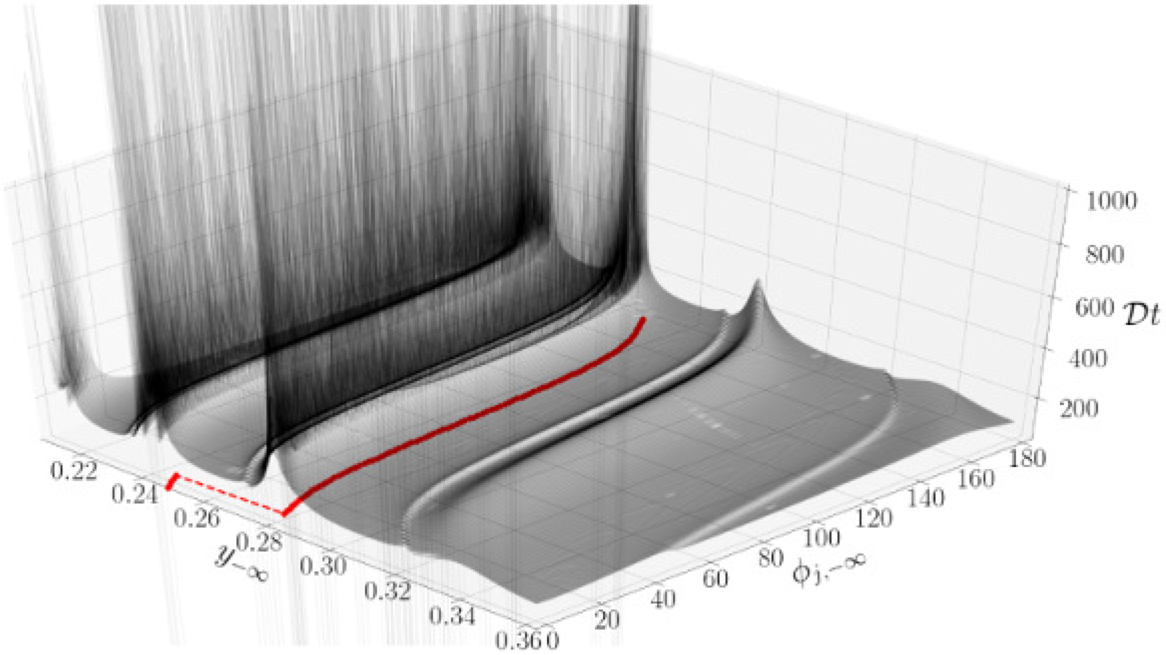

(a)

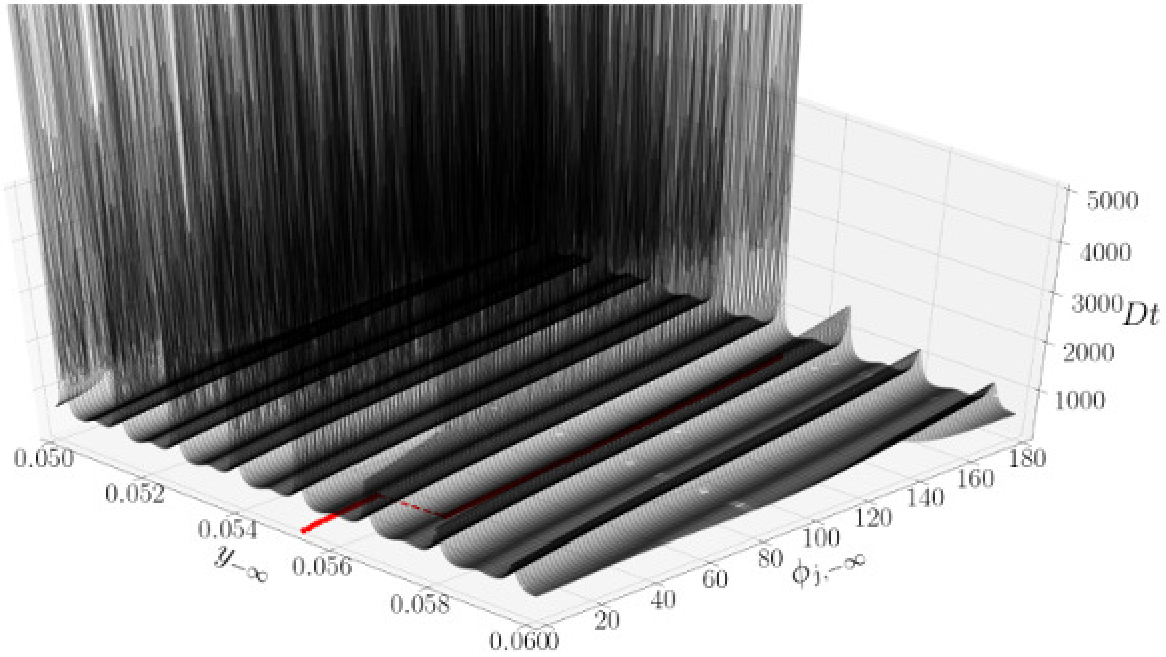

(b)

Fig. 3.14 Variation of the residence time surface for a tumbling prolate spheroids of (a) $\xi_0 = 1.05(\kappa = 3.28)$) and (b) $\xi_0 = 2(\kappa = 1.15)$), as a function of the upstream gradient offset of the fluid pathline ('upstream' here corresponds to $x = -20$) and $\phi_{j,-\infty}$.

$y_{-\infty}, \phi_{j,-\infty}$ plane. In both figures 3.14a and b, the separatrix curve has a step discontinuity; as will be seen below, this jump arises due to the abrupt appearance of a chaotic burst on a previously regular peak.

Having characterized the residence time surface, we return to the specific case of $\phi_{j,-\infty} = 0$, and now compare the manner in which the signatures of chaotic scattering disappear as one approaches the limit of an integrable system (note that the term 'integrable' is used here in a loose sense, to denote the regular nature of the trajectories, and the resulting smooth dependence on initial conditions; the problem of a spheroid in a simple shear flow is evidently non-Hamiltonian). The two limiting integrable cases are that of a spinning spheroid of any aspect ratio, the streamline topology for which has already discussed in detail in section 2.1, and an infinitely slender prolate spheroid ($\kappa \to \infty$ or $\xi_0 \to 1$) in any of the finite-C Jeffery orbits. We examine the latter limit first. The integrability in this case arises because viscous slender body theory[11] shows that the time dependent disturbance velocity field associated with a slender fiber (responsible for the non-integrability of this system), in a region around it of order its length, scales as the inverse of the logarithm of its (large) aspect ratio. Thus, at leading logarithmic order, a fluid element is merely convected by the ambient simple shear flow. Such an approximation has been earlier used to analyze the effect of polymeric stresses on fiber motion in simple shear flow; in particular, to analyze the viscoelasticity-induced drift across (meridional) Jeffery orbits for large Deborah numbers[45]. In this limit, the polymeric stress at a point is approximated based on the integrated effect of velocity gradients experienced by a fluid element (containing polymer molecules) along an ambient flow streamline that convects the element upto the point of interest. Figures 3.15a-e show a comparison of the residence time distributions for tumbling prolate spheroids of increasing aspect ratio, approaching the slender fiber limit; κ ranges from 2.4 ($\xi_0 = 1.1$) in figure 3.15a to 70.7 ($\xi_0 = 1.0001$) in figure 3.15e. Note that the length scale characterizing the undulations in the residence time curves, induced by the spheroid orientation dynamics, increases with increasing κ. As mentioned earlier, this is due to an increase in the Jeffery period. Each of the residence time curves is overlaid on a smooth curve that plots the residence time estimated based on convection by the ambient shear alone and that is therefore proportional to $1/y^{-\infty}$. For the smaller aspect ratios, notwithstanding the chaotic bursts, the ambient-flow-based estimate, ends up overestimating the residence time. This is because accounting for the disturbance velocity field leads to the fluid element being advected to larger y in the vicinity of the rotating spheroid, in turn leading to a faster (local) convection by the ambient flow. For the largest aspect ratios (figures 3.15d and e), the ambient-flow-based estimate is quite accurate, validating to some extent a slender-body-theory-based analysis that neglects of the disturbance velocity field as far as the fluid pathlines is concerned. From figures 3.15d and e, it is also evident that the separatrix offset, $y_{-\infty}^{sep}$, that marks the onset of the chaotic bursts, eventually decreases with increasing aspect ratio, again emphasizing the dominance of the ambient flow, and thence, the approach towards an integrable limit ($\kappa = \infty$). This approach is, however, a singular one, with the intermittent chaotic bursts corresponding to large departures of the residence time from the $O(1/y^{-\infty})$ ambient-flow-based estimate even for the largest κ shown. As shown in figure 3.15e, these departures correspond to a 'trapping' of the fluid pathline for a long time in the vicinity of the rotating spheroid. Such trapped pathlines execute a large number of loops around the spheroid; in contrast, the pathlines above the separatix, and those in the regular intervals for $y_{-\infty} < y_{-\infty}^{sep}$, are open. Interestingly, for the largest κ, the dips of the residence time curve below the ambient-flow-based estimate correspond to regular reversing pathlines that do not loop around the spheroid (see inset in Figure 3.15e). Finally, note that the signatures of chaotic scattering are also not readily apparent for the largest κ. Thus, although we have marked a separatrix offset in this case, it is possible that the irregular dependence of the residence time, in a manner resembling the smaller κ's, now occurs on scales smaller than those resolved.

Based on the residence time distributions shown in figure 3.15, and those for other aspect ratios, figure 3.16a plots the upstream (gradient) offset of the separatrix ($y_{-\infty}^{sep}$), marking the onset of chaotic scattering, as a function of the spheroid aspect ratio. Although the separatrix offset appears to eventually decrease monotonically for the largest aspect ratios with $y_{-\infty}^{sep} \sim \kappa^{-4.5}$, for $\kappa \to \infty$, the variation for moderately large aspect ratios is non-monotonic on account of a series of seemingly discontinuous jumps in $y_{-\infty}^{sep}$ at certain aspect ratios (similar to the jumps seen earlier in figures 3.14a and b). To examine this further, we plot in figure 3.16b the residence time distributions for a pair of aspect ratios on either side of a particular $y_{-\infty}^{sep}$ jump. It is seen from the distributions that the jump arises from the sudden appearance of a chaotic burst in a previously smooth peak (located just above the separatrix) with increasing aspect ratio. Note that, even for a slender fiber, there would still be fluid elements that approach the fiber to within a distance of order its diameter, and which would then suffer a strong interaction (since the disturbance field isn't small in this region). But, the fraction of fluid elements that undergo such a strong interaction must approach zero as κ^{-1}, owing to the smallness of the 'collisional' cross section which scales as the product of the fiber length and diameter. Thus, the upstream gradient offset of fluid elements that undergo a strong interaction is expected to scale as κ^{-1}. While $y_{-\infty}^{sep}$ in figure 3.16a asymptotes to zero more rapidly, as $\kappa^{-4.5}$, the numerical values of the offsets remain larger than the spheroid diameter for the largest aspect ratios examined. We have verified that the separatrix offsets for oblate spheroids exhibit a similar series of jumps for κ decreasing to zero (not shown). Unlike the prolate case, the oblate spheroid disturbance field remains finite in the limit $\kappa \to 0$, and one might therefore expect the separatrix offset for a flat disk to also remain finite. Over the range of aspect ratios examined, however, we find separatrix offsets for oblate and prolate spheroids to remain comparable in magnitude.

Next, in figure 3.17, we present a comparison of the residence time distributions as a function of the orbit constant C, for a prolate spheroid of $\xi = 1.05(\kappa = 3.28)$. The sequence of orbit constants chosen is C=1, 0.5, 0.1, 0.04, 0.01, and thus approaches the other integrable limit (a spinning spheroid: $C = 0$) mentioned above. Similar to figure 3.15, and for purposes of comparison, we plot the residence time distribution corresponding to a spinning spheriod, of the same aspect ratio, in each of the sub-figures. For a spinning spheroid, and for the finite x-interval (-20,20) under consideration, the residence time remains finite regardless of $y_{-\infty}$. Since closed streamlines correspond to an infinite residence time, the spinning spheroid curve shown terminates at the separatrix($y_{-\infty}^{sep(spin)}$); this is unlike figure3.2b where it was continued to the closed orbits within, by taking the residence time to be equal to the orbital half-periods. Although for the aspect ratio examined in Figure 3.17, there remains a large difference between the offsets of the actual separatrix ($y_{-\infty}^{sep}$) and the spinning-spheroid separatrix ($y_{-\infty}^{sep(spin)}$) down to the smallest C's, the location of the separatrix for the smallest C's nevertheless begins to correlate with a rather abrupt increase in the residence times, in a manner resembling the spinning-spheroid distribution. Unlike the slender fiber limit examined above, figure 3.18 shows that the separatrix offset starts from an order unity value (specific to $\kappa = 1.05$) for large C, and decreases monotonically for C going to zero, implying a similar decrease of the size of the chaotic region as one approaches the spinning-spheroid limit.

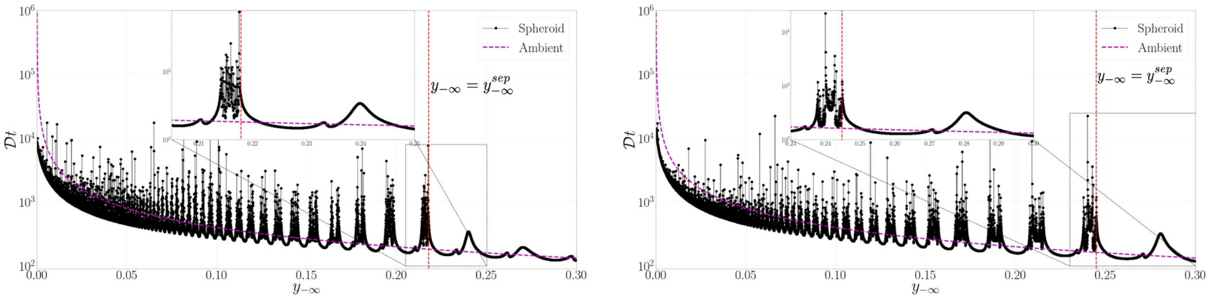

(a) $\xi_0 = 1.1$ (b) $\xi_0 = 1.05$

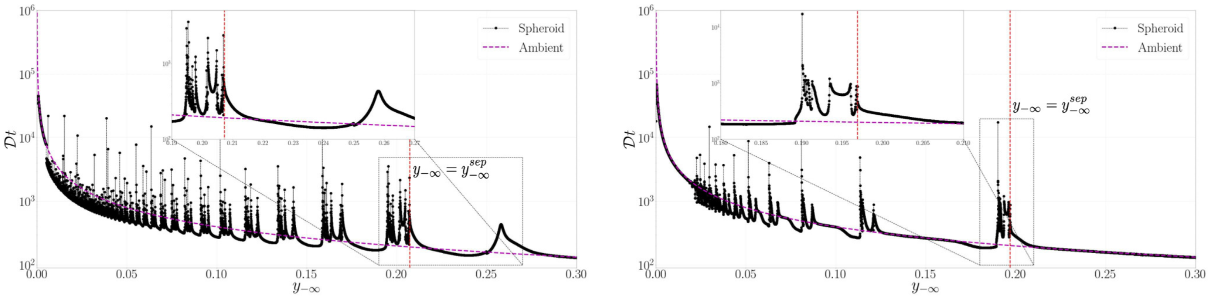

(c) $\xi_0 = 1.01$ (d) $\xi_0 = 1.001$

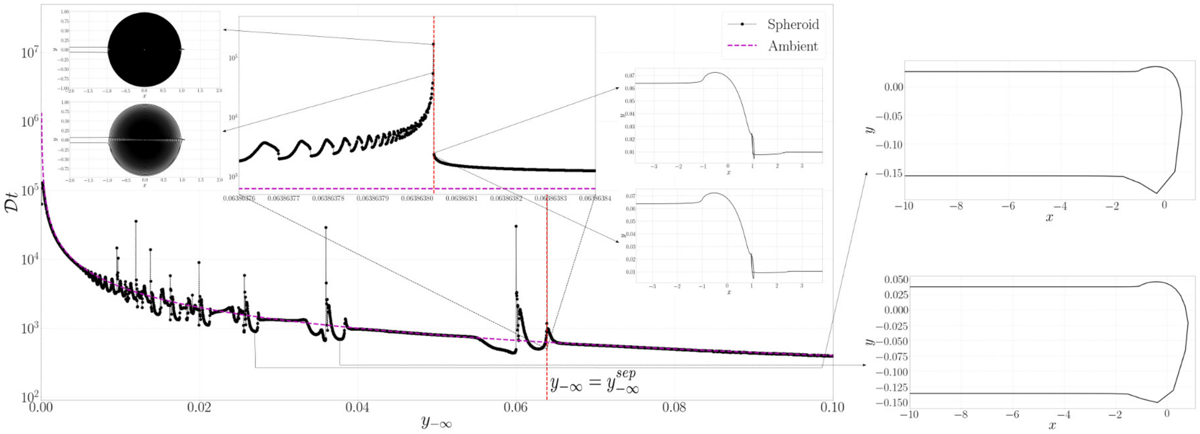

(e) $\xi_0 = 1.0001$

Fig. 3.15 Variation of the residence time for tumbling prolate spheroids with $\xi_0 = 1.1, 1.05, 1.01, 1.001, 1.0001 (\kappa = 2.4, 3.28, 7.12, 22.68, 70.7))$ with $\phi_{j,-\infty} = 0$. The red vertical line separates the regular and chaotic regions, the magenta curve denotes the residence time estimate based on the ambient simple shear flow. The insets in Figure 3.15e show sample pathlines for upstream offsets less and greater than that of the separatrix ($y_{-\infty}^{sep}$); those below the separatrix, and within the chaotic burst intervals, loop around the spheroid a large number of times (the two insets on the left), while the other pathlines are open (the insets on the right).

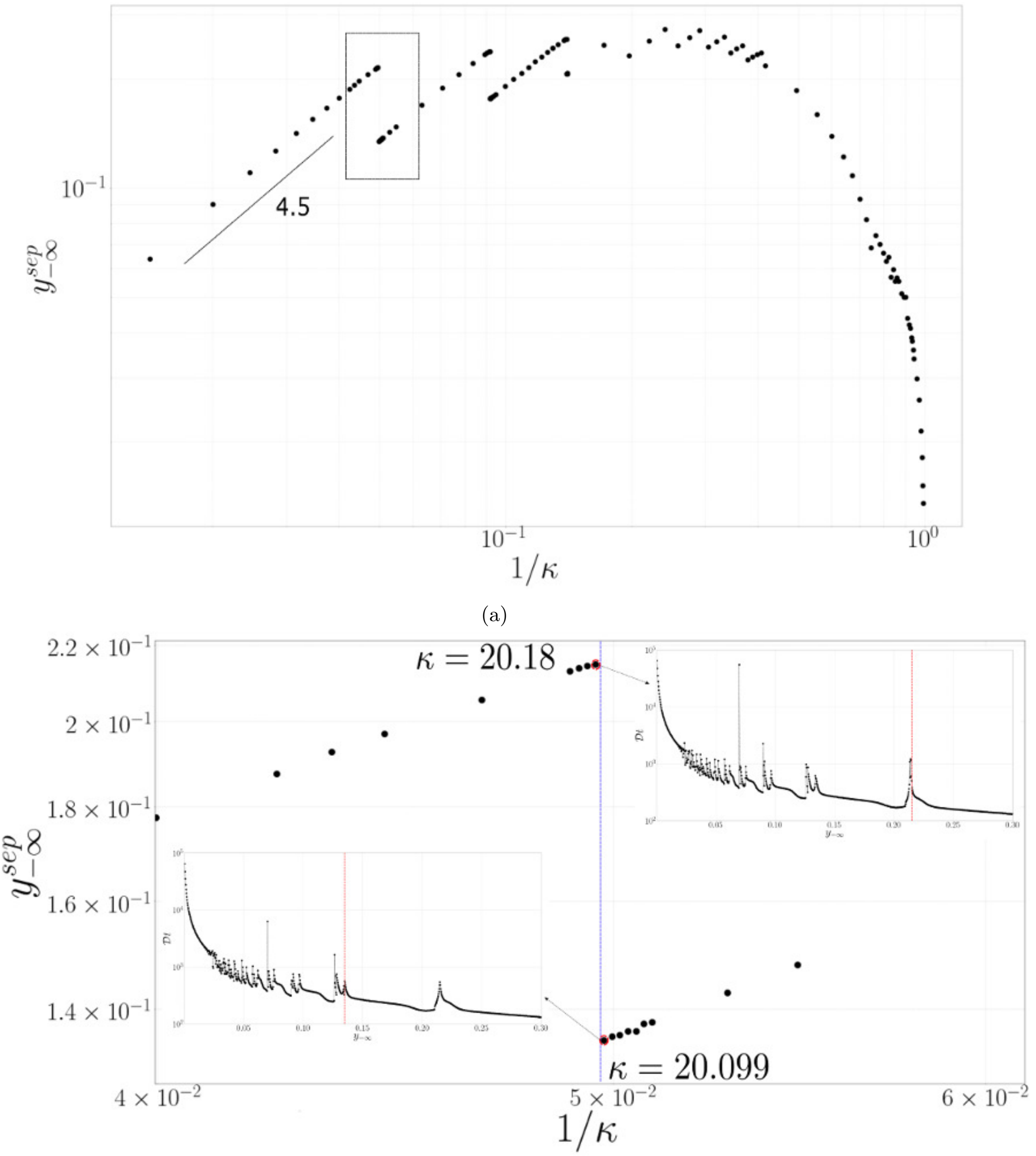

(a)

(b)

Fig. 3.16 (a) The upstream gradient offset of the separatrix, $y_{-\infty}^{sep}$, for tumbling spheroids, as a function of the spheroid aspect ratio, (b) Residence time plots for the (circled) aspect ratios κ =20.18 and 20.099, in the close vicinity and on either side of a $y_{-\infty}^{sep}$ jump.

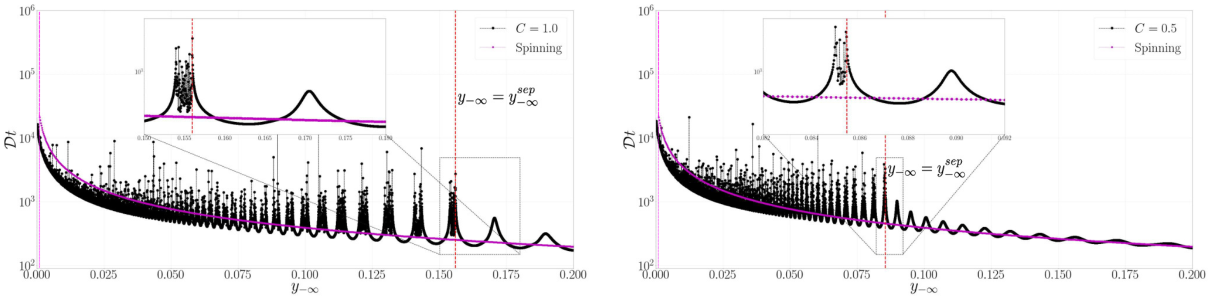

(a) $C = 1, t = 4000T_j$ (b) $C = 0.5, t = 4000T_j$

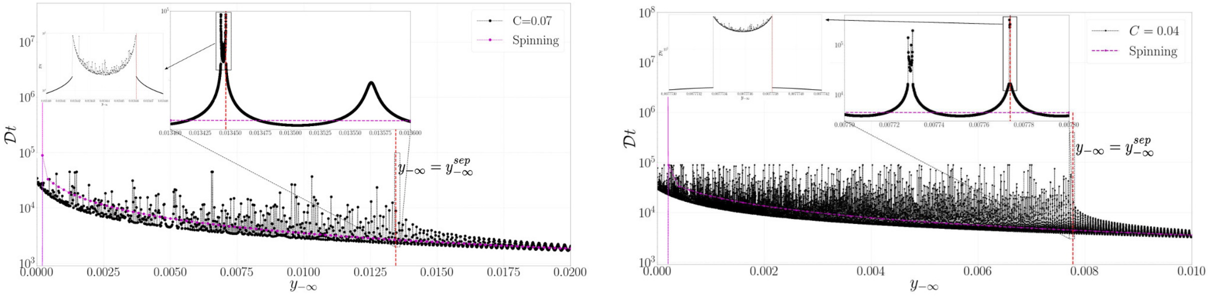

(c) $C = 0.07, t = 10000T_j$ (d) $C = 0.04, t = 10000T_j$

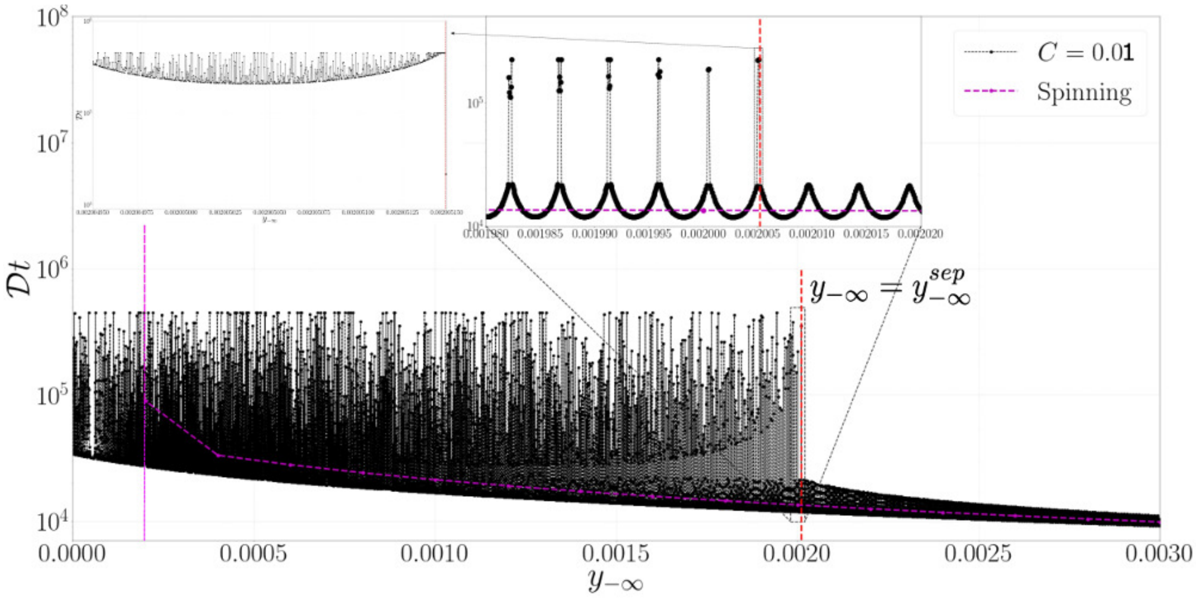

(e) $C = 0.01, t = 20000T_j$

Fig. 3.17 Variation of the residence time, for prolate spheroid with $\xi_0 = 1.05(\kappa = 3.28)$ in Jeffrey orbits $C = 1.0, 0.5, 0.07, 0.04, 0.01$ with $\phi_{j,-\infty} = 0$. Red vertical line in each figure separates the regular and chaotic regions, the magenta curve denotes the residence time for the spinning($C = 0$) spheroid, with the magenta vertical line denoting the separatrix for the spinning orbit.

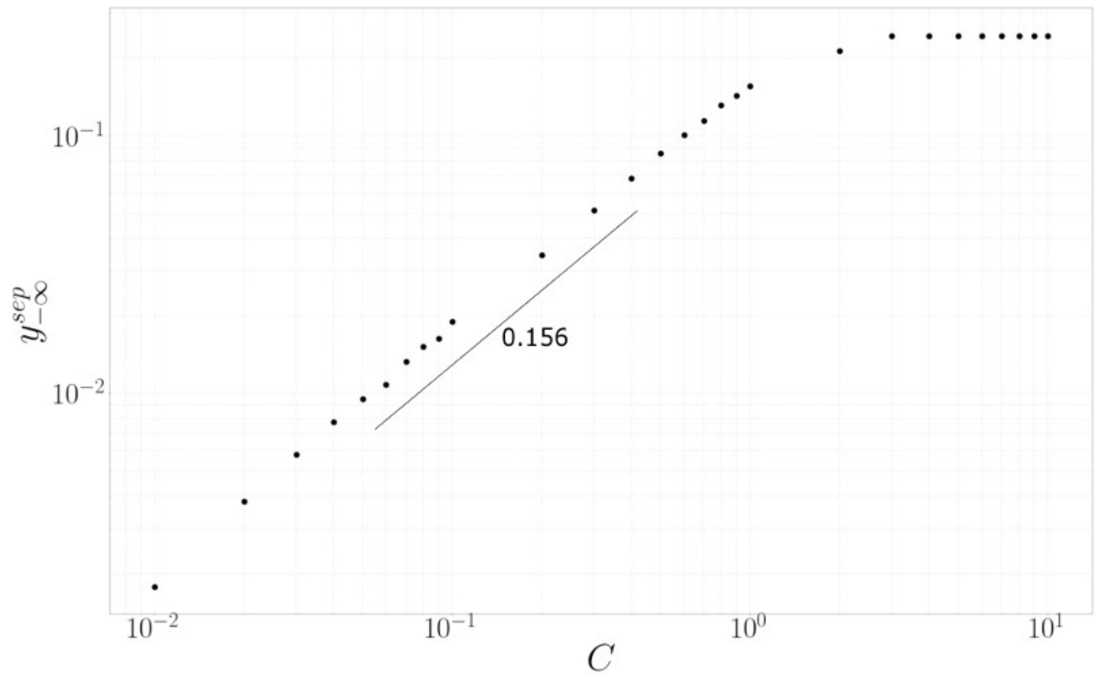

Fig. 3.18 The gradient offset of the separatrix, $y_{-\infty}^{sep}$, plotted as a function of the Jeffery orbit constant C, for a prolate spheroid with $\xi_0 = 1.05 (\kappa = 3.28)$.

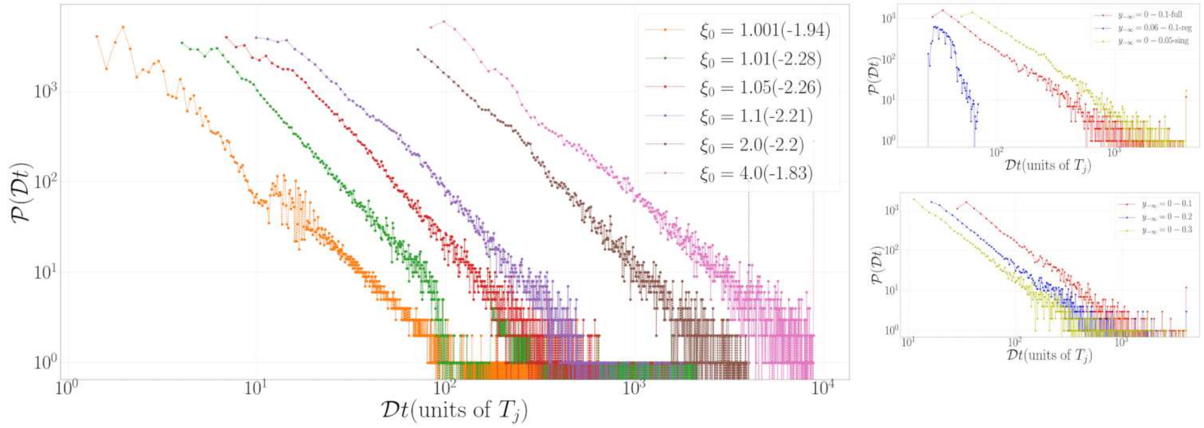

Fig. 3.19 The main figure shows the residence time probability densities for tumbling prolate spheroids of different aspect ratios; the slopes of the algebraic tails appear within brackets. The top figure on the right shows the total probability density for $\xi_0 = 2$, and the component densities corresponding to regular $(y_{-\infty}^{sep}, y_{-\infty})$ and singular $(0, y_{-\infty}^{sep})$ pathlines. The bottom figure on the right demonstrates the insensitivity of the tail to the interval of upstream offsets considered.

Figure 3.19 shows the residence time probability densities for tumbling prolate spheroids of decreasing aspect ratios: $\kappa(\xi_0)$=22.38(1.001), 7.12(1.01), 3.28(1.05), 2.4(1.1), 1.15(2) and 1.03(4). Rather surprisingly, and in contrast to much of the literature on chaotic scattering, the probability densities for all cases examined appear to have algebraic rather than exponential tails [16, 15, 52, 41, 39]. The lower figure on the right shows the invariance of the algebraic tail to the interval of upstream offsets considered. The top figure on the right shows three probabililty densities corresponding to regular pathlines in $(y_{-\infty}^{sep}, y_{-\infty})$, singular pathlines in $(0, y_{-\infty}^{sep})$, and all of the pathlines in $(0, y_{-\infty})$. The tail, corresponding to asymptotically long residence times, is seen to be entirely controlled by the singular pathlines; an increase in $y_{-\infty}$ only amounts to considering a greater number of regular pathlines, with shorter residence times, leaving the tails unaffected. An important implication of the algebraic tails in Figure 3.19 is the absence of a characteristic escape time, and the related possibility of a scale dependent structure of the underlying chaotic saddle, in turn implying that the spheroid may be a non-hyperbolic scatterer [65]. Despite the aforementioned evidence of non-hyperbolicity, however, we find algebraic scaling behavior for the uncertainty ratio, as seen in Figure 3.11, and as is expected for a hyperbolic scatterer. Further, successively magnified views of the residence time plots do not reveal an obviously denser distribution of chaotic scattering intervals on the smaller scale. Thus, ascertaining the nature of the scatterer (non-hyperbolic or otherwise) requires a more detailed numerical investigation with an emphasis on scales (the $\epsilon' s$ in Figure 3.11) much smaller than those examined here.

Chapter 4

Conclusion and outlook

4.1 Chaotic Scattering in simple shear flow: Summary and implications

In this study, we have examined the topology of the fluid pathlines induced by freely rotating neutrally buoyant spheroids, both prolate and oblate, and of an arbitrary aspect ratio, in simple shear flow. The fluid pathline configuration is analyzed as a function of the particular spheroid orbit, as defined by the orbit constant C. In the spinning or log-rolling ($C = 0$) orientations, one has a steady scenario, and the fluid pathlines are the same as streamlines. Further, the topology of the streamline configuration is identical to that already known for the limiting cases of a sphere or a cylinder. There are two distinct groups of streamlines, open and closed, and these are separated by a surface of limiting streamlines, termed separatrices, that 'closes at infinity'. For spinning prolate spheroids, various measures relating to the streamline configuration, including the size of the closed streamline region, the orbital periods of the individual closed streamlines, etc, are bounded between those for a sphere and a cylinder (see Figure 2.1).

On the other hand, when the spheroid is in any of the precessional orbits, including the tumbling one($0 < C \leq \infty$), almost all pathlines are open, in that they come from and eventually go to infinity. Nevertheless, the open pathlines may be divided into two groups. The first group are the regular open pathlines which come from and go to infinity without looping around the precessing spheroid. The residence time for these pathlines, in a certain neighborhood of the spheroid, is a smooth function of their initial coordinates defined as their offsets, far upstream, in the gradient and vorticity directions. One may therefore regard these regular pathlines as trivial generalizations of the open pathlines around a sphere or a cylinder. In general, these pathlines are fore-aft asymmetric (with respect to the gradient vorticity plane), and may therefore be characterized via the net displacements in the gradient or vorticity directions (see Figure 2.5). For the most slender spheroids, there is the appearance of regular reversing pathlines that are absent for a torque-free sphere or a cylinder.

The most important results of this thesis concern the second group of open pathlines, the singular ones, that loop around the precessing spheroid on their way from upstream to downstream infinity. These differ in a profound manner from the closed pathlines around a freely rotating cylinder or a sphere. It is observed that the number of loops, or alternatively, the residence time of these pathlines in a certain neighborhood of the spheroid, has an extremely sensitive, seemingly random, dependence on the initial offset, with this sensitivity persisting until the smallest (numerically) resolved scales. Such a fractal dependence on initial coordinates is a defining characteristic of chaotic scattering as investigated earlier in other scenarios that include the laminar-to-turbulent transition in plane Couette flow[98], pipe flow[39, 41, 93], dynamics of point vortices[7, 6, 37], to name a few. The infinitely sensitive variation of the residence time found here implies the existence of a chaotic saddle, and thence, of a set of singularities on a Cantor-like set in the vicinity of the rotating spheroid; for the particular case of simple shear flow examined here (see final paragraph below), this singular set might extend to infinity along the flow axis. The singular set refers to the set of bounded pathlines with infinite residence times, and includes both an infinite number of periodic orbits, and an uncountably infinite number of aperiodic ones. It is, of course, numerically impossible to exactly locate any of these pathlines, but their existence may be inferred in a manner similar to that in Figure 3.4. We have investigated the nature of the local graph of the unstable manifold by numerically mimicking the experiment of [44], whereby the fractal structure is readily evident(Figure 3.9); a partial representation of the invariant chaotic saddle, for a near-sphere, is shown in Figure 3.10. We have also investigated in detail the transition from regular to chaotic scattering as a function of the underlying physical parameters that include the upstream gradient offset, the orbit constant and the spheroid aspect ratio. This included looking at the nature of approach to the known integrable limits - that of an arbitrary aspect ratio spheroid in the spinning orbit (Figure 3.18), and that of an infinitely slender prolate spheroid in any orbit (Figure 3.16). An aspect not investigated in detail is the variation in the spatial extent of the chaotic saddle as one moves away from the flow-gradient plane, that is, as a function of the upstream vorticity offset of the pathlines. Figure 4.1 presents the results of a limited investigation along these lines, and shows that (1) the scenario, for a fixed non-zero $z_{-\infty}$, remains similar to the inplane case, and (2) that the separatrix offset $y_{-\infty}^{sep}$ decreases with increasing $z_{-\infty}$.

One needs to emphasize the distinction between Hamiltonian and non-Hamiltonian settings here. In the former case, one can relate the onset of chaos to the onset of bound orbit sequences that correspond to infinite yet non-recurring sequences of reflection from the Hamiltonian peaks (as indicated by [38, 37]). It is also not difficult to identify a critical energy level, based on the governing Hamiltonian, that signals the onset of the aforementioned bound sequences. There doesn't seem to exist any such analogy in our case, and thus, no obvious way to predict the offset of the separatrices that mark the onset of chaotic scattering. The latter is true for the other non-Hamiltonian problems too (the laminar-turbulent transition, for example). Finally, it is important to mention that we have found the probability densities of residence times, for all cases examined, to have algebraic rather than exponential details, suggesting that the underlying scatterer has a non-hyperbolic character. The non-hyperbolic character has previously been attributed to a no-slip boundary in the vicinity of the chaotic saddle [44], but is more difficult to rationalize in the present problem, since the spheroid rotates at a finite rate at all times.

As indicated in the Introduction, the findings of the present investigation might have profound implications for transport problems in disperse multiphase systems. In what follows, we briefly discuss three instances, in roughly increasing order of complexity. The first is the transport of heat or mass from particles in shearing flows. As originally shown by Acrivos [1, 87], the rate of scalar transport from a freely rotating sphere in a planar linear flow has an exceptional character; planar linear flows form a one-parameter subset of the general family of linear flows (see discussion in the final paragraph below, for the values that this parameter takes), with the limiting values of the parameter corresponding to planar extension and solid-body rotation. The dimensionless rate of transport, as characterized by the Nusselt number (Nu), does not increase indefinitely with the Peclet number (Pe). Such an increase would occur

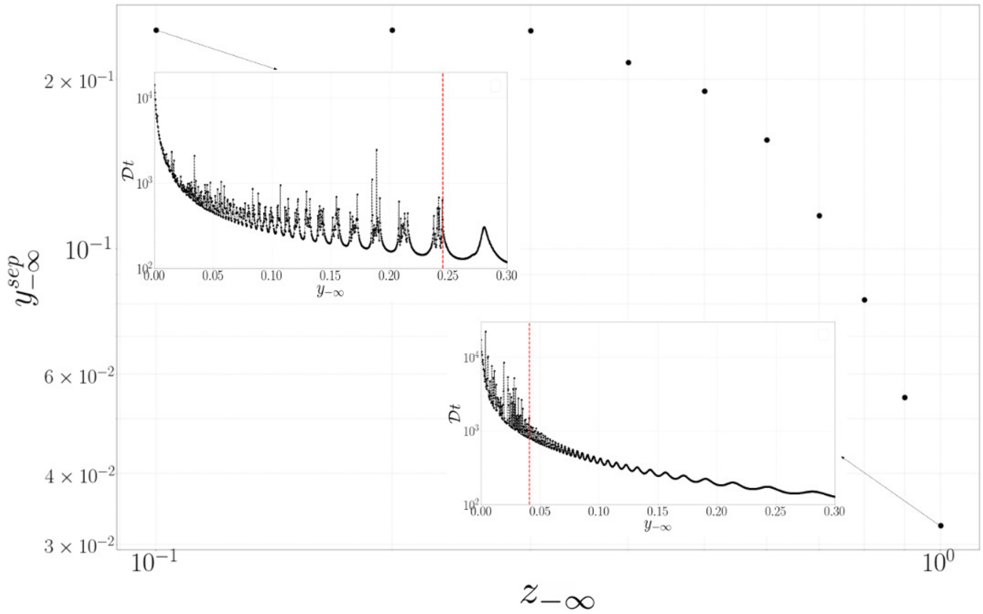

Fig. 4.1 The gradient offset of the separatrix, $y^{sep}_{-\infty}$, plotted as a function of the vorticity offset $z_{-\infty}$, for a prolate spheroid with $\xi_0 = 1.05 (\kappa = 3.28)$, with the sample residence time distributions for $z_{-\infty} = 0.1$ and 1.0

if, at large Pe corresponding to the convectively dominant limit, the transport were to occur via a thin boundary layer, as is the case for a translating sphere; see [2]. Instead, Nu saturates at an order unity value dependent on flow-type, the saturation arising due to the transport eventually being limited by diffusion across closed streamlines that surround the sphere in all of the planar linear flows (except planar extension). The singular alteration of the trajectory topology owing to a deviation of the particle from sphericity, found here, must manifest as qualitatively different Nu v/s Pe curves for a sphere and spheroid in a given planar linear flow. In contrast to a sphere, for large enough Pe, one expects the transport from a freely rotating spheroid to be dominated by the set of singular open pathlines which convect heat or mass away in an efficient manner. This should avoid the diffusion limitation for a sphere, leading to a continued growth of Nu with Pe, with the nature of this growth dependent on the residence time distributions of fluid elements obtained here (for instance, those shown in Figure 3.12); any scaling exponent characterizing the large-Pe asymptotics of Nu, would be a sensitive function of aspect ratio via the residence time distributions. For spheroids with near-unity aspect ratios (the weakly non-integrable cases), corresponding to small eccentricities of $O(1/\xi_0)$ with $\xi_0 \gg 1$, scaling arguments based on averaging over the closed streamlines around a sphere, show that Nu will start increasing beyond a Pe of $O(\xi_0^4)$. Thus, for a near-sphere, one expects Nu to begin from a diffusive plateau for small Pe, increase to an intermediate order-unity convective plateau (with $Nu \approx 4.5$ for the specific case of simple shear flow) for $1 \ll Pe \ll \xi_0^4$, and increase again (to infinity) for $Pe \geq O(\xi_0^4)$. Recent efforts [101, 103, 59] have examined the singular effect of weak inertia-induced convection on the originally diffusion-limited behavior of Nu in the Stokesian limit. The above discussion suggests that departure from sphericity again have a singular effect, manifesting as a convective enhancement for large Pe. The convective flow in the inertial case may be derived using a straightforward perturbation expansion in the particle Reynolds number, but that for the non-spherical case is non-trivial, and even for a near-sphere would require the notion of lobe dynamics. The latter has been used earlier to describe the efficient (non-diffusive) exchange of material between the irrotational volume entrained by a vortex ring, or a pair of counter-rotating point vortices, and the ambient[92].

A second problem concerns the rheology of dilute viscoelastic suspensions of anisotropic (axisymmetric) particles which sensitively depends on the orientation dynamics of these particles in an imposed shear. The degenerate nature of the orientation distribution, arising from the existence of closed (Jeffery) orbits in the Stokesian limit [67, 29, 76] is well known, and implies that the orientation distribution, in a viscoelastic suspending medium, crucially depends on a viscoelasticity-induced drift across orbits. This drift is governed by the polymeric stress field. For small Deborah numbers (De), the polymeric stress may be determined using an ordered fluid expansion, and is therefore only a function of the local velocity gradient associated with the Stokesian velocity field. But, for large De, the relaxation times are long compared to the characteristic residence time of a fluid element in the vicinity of the rotating particle, and one expects the polymeric stresses to therefore arise from the integrated effects of the velocity gradients seen by a polymer molecule as it is convected along a fluid pathline. For small polymer concentrations, these pathlines will have a near-Newtonian (Stokesian) character, and the non-trivial pathline topology identified here implies that the polymeric stress field, and thence the particle drift, might be crucially influenced by the stresses that develop along the singular open pathlines. In fact, on account of the non-integrable nature of the pathline topology, one expects the spatial variation of polymeric stresses to have a singular character; that is to say, the polymeric stresses at points located arbitrarily close to each other might differ by a finite amount, on account of an analogous difference in the residence times of fluid pathines arriving at these points. This in turn points to a probabilistic (rather than deterministic) formulation of the particle-polymer-molecule interaction where, rather than determining the polymer stress field at each point in the domain, one attempts to instead determine the probability distribution of polymeric stresses that develops in the neighborhood of a single point (within the domain influenced by the chaotic saddle). For large aspect ratios, the above problem admits a well known simplification, on account of the disturbance velocity field being logarithmically small (as discussed in section 3.2). For finite De, this simplification allows one to approximate the polymeric stresses by integrating a functional of the Stokesian velocity gradients along an ambient streamline instead of the actual fluid pathline. This simplification has been exploited in earlier calculations (for instance, see [45]). While such a simplification is certainly valid for steady velocity fields, as for instance, the flow around a sedimenting spheroid with an unchanging orientation in the Stokesian limit (see section 5 in [29] and [68]), the scenario in an ambient shear flow might be more complicated even in the slender fiber limit. As shown in figure 3.15, the approach to this limit has a singular character - while the residence time, based on the convection by the ambient shear alone, does give an accurate estimate for the regular intervals, for sufficiently large aspect ratios, the occasional chaotic bursts nevertheless lead to very pronounced departures of the residence time from the ambient-shear-based envelope. It would be of interest to examine quantitatively the consequences of such departures for the polymeric stresses that develop along the heavily looped pathlines.

The pathline topology found here is also relevant to inertio-elastic focussing of anisotropic particles in microfluidic channels with applications towards shape sorting [112, 3]. The focusing arises due to transverse migration driven by elasto-inertial lift forces. For small Re and weakly elastic fluids, the contributions from the elastic and inertial non-linearities will be additive. The inertial lift force arises from the flow on length scales of order the channel cross-sectional dimension, while the dominant contributions to the elastic lift force arise from smaller length scales of order the particle size. Scaling arguments based on this may be used to show that the inertial lift force is $O(Re\,\mu U a^3/H^2)$, while the elastic lift force must be $O(De\,\mu U a^4/H^3)$ (see [47, 48]). As a result, a non-trivial inertio-elastic equilibrium arising from a balance of the two lift force contributions requires De to be $O(Re\,H/a)$ where $H/a \gg 1$ is the ratio of channel to particle size. Thus, for $Re \sim O(1)$ or greater, calculating the elastic lift force will involve determining polymeric stresses, for large De, along fluid pathlines along the lines mentioned above, and this calculation will beset by the same issues.

The third problem which, in fact, motivated the examination of the fluid pathline topology in the first place concerns pair-spheroid interactions. As mentioned in the introduction, one expects the fluid pathline topology around a single particle to have some bearing on the nature of pair-particle interactions. This is certainly true for a spherical particle, where the streamline and pair-particle-pathline topologies are identical. Thus, the findings here imply that pair-spheroid trajectories are likely to have a similar singular character. As indicated in [75], one would ideally want to characterize pair-spheroid interactions via a phase-averaged scattering kernel that would relate the pre- and post-interaction orbit constants. The findings here would, however, imply that even an infinitesimal change in the input orbit constant would likely lead to an order unity change in the post-interaction orbit constant. In other words, the scattering kernel would be singular (in fact, such singular kernels in the context of reacting molecules constituted the very first pieces of evidences of chaotic scattering, see [43, 82]). Therefore, similar to the polymer-spheroid problem above, instead of the exact pair-interaction kernel, one would again want to describe even individual pair-interactions in a probabilistic framework.

4.2 Chaotic Scattering in hyperbolic planar linear flows

Although a canonical flow-type from the fluid mechanical viewpoint, owing to its significance to rheology, for instance, the choice of simple shear flow does appear inconvenient from the dynamical systems perspective. As is well known (for instance, see [77, 104]), simple shear flow may be regarded as a member of the aforementioned one-parameter family of planar linear flows. The parameter here is α (say), with $(1+\alpha)/(1-\alpha)$ being proportional to the ratio of extension to vorticity. Simple shear, corresponding to $\alpha = 0$, is then the threshold flow, with equal magnitudes of extension and vorticity (leading to straight streamlines), separating the hyperbolic planar linear flows with open streamlines ($\alpha > 0$), from the elliptic ones with closed streamlines ($\alpha < 0$). If one now considers a spinning spheroid in a hyperbolic linear flow, from the results of section 2.1, one expects, similar to a sphere, a trajectory topology where separatrices demarcate the closed from the open streamlines; for instance, see Figure 4.2a above(also see Figure 6 in [104] which sketches the trajectory topology for a sphere). Importantly, for a hyperbolic linear flow, the closed streamline region, projected onto the flow-gradient plane, has a finite spatial extent for any spheroid aspect ratio, and the aforementioned separatrices are now heteroclinic trajectories connecting a pair of saddle points(see Figure 4.2a). If the analogy with a sphere is exact, then the closed streamline envelope has a finite volume, and the saddle points will correspond to the points of intersection, of a fixed-point curve, with the flow-gradient plane. All of these fixed points have a saddle-like character, with the curve reducing to a fixed-point circle for the case of a sphere. The existence of such heteroclinic connections highlights the structurally unstable trajectory topology for a spinning spheroid. One may now interpret the deviation of the spheroid, from the spinning orbit to a precessional one, corresponding to a small but finite C, to constitute a perturbation that renders the system non-integrable. Importantly, one expects the non-integrability of the perturbed system to manifest as transverse intersections of the stable and unstable manifolds associated with the two saddle

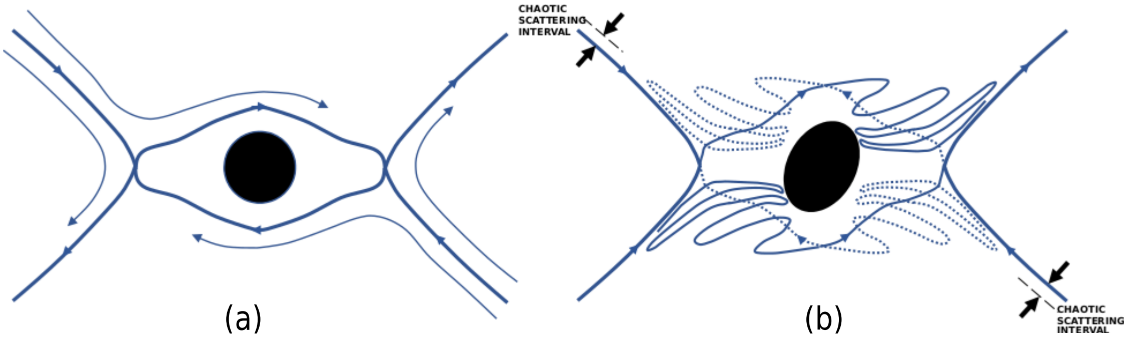

Fig. 4.2 Smooth and chaotic separatrix in the hyperbolic flow over (a)a sphere and (b)a precessing spheroid; note that the infinitely convoluted manifolds lead to lobes that eventually extend to arbitrarily large distances along the separatrices (that go off to infinity), and it is the presence of these lobes that lead to the chaotic scattering intervals indicated in Figure(b).

points(see Figure 4.2b), and the existence of such intersections can be rigorously demonstrated via the construction of a Melnikov function [109], as has been done earlier in the fluid mechanical context [57, 4]. As sketched in Figure 4.2, the implication of these intersections is that, in the far-field, intervals of chaotic scattering must replace the original separatrix for the spheroid rotating in any precessional orbit. The trajectory topology in Figure 4.2, although less symmetric, nevertheless resembles the pathline topology analyzed by [92], wherein the non-integrability arose from the time dependence imposed by an oscillatory planar extension acting on a counter-rotating vortex pair. Although related, the emphasis in this work was not on the chaotic scattering aspects, but instead on the exchange of fluid across the (infinitely) convoluted intersecting manifolds. Figure 4.2 suggests that, from a dynamical systems viewpoint, the non-integrability for the simple shear flow examined here is perhaps best interpreted as the singular limiting case, for $\alpha \to 0^+$, of a hyperbolic linear flow, when the saddle points recede to infinity.

In what follows, we report preliminary numerical evidence for the emergence of an interval of chaotic scattering in a hyperbolic planar linear flow, thereby reinforcing the qualitative arguments given above based on the intersecting manifolds sketched in Fig 4.2b. Figure 4.3 plots the residence time distributions for a prolate spheroid of aspect ratio $\kappa = 1.15(\xi_0 = 2)$ in a hyperbolic linear flow with $\alpha = 0.001$; the small α implies that the flow chosen lies in the close vicinity of simple shear flow. Figure 4.3a shows the streamline configuration around a spinning spheroid, and corresponds to the integrable limit. Here, the finite separatrix envelope ends in a pair of saddle points as indicated above, and pairs of separatrices(shown in red lines) emerge from each of these saddle points, heading off to infinity; note that the small value of α ensures that the saddle points are well separated from the spheroid (the distance, along the x-axis of the saddle points scales as $\mathcal{O}(\alpha^{-1/5})$ for $\alpha \to 0$. Among the aforementioned separatrices that head off to infinity, the separatrix in the second quadrant (negative x, positive y) separates streamlines that head off to infinity in the positive-x direction from the reversing streamlines that head off to infinity along the negative-x direction. Next, Figure 4.3b depicts the residence time distributions for precessing spheroids as a function of the orbit constant(C); the distributions have been calculated as a function of the gradient offset ($y_{-\infty}$) of fluid elements that have been released at $x_{-\infty} = -20$ (the numerical representation of upstream infinity). We choose nine different initial upstream Jeffrey orientations($\phi_{j,-\infty} = 0, 0 \leq \theta_{j,-\infty} < \pi/2$) of the spheroid, each of which corresponds to a particular initial Jeffrey orbit, with $\theta_{j,-\infty} = 0$ and $\pi/2$ corresponding to the spinning and tumbling orbits, respectively. In each of the cases above, the fluid element is started off at the upstream gradient offset $(y_{-}\infty)$, at $x_{-\infty} = -20$, and integrated forward in time for $2000\,T_j$. Note that, in Fig 4.3b, the aforementioned residence time distributions have been displaced in the vertical direction for easy viewability, with the baseline spinning case being shown at the bottom. For the spinning case, as evident from Fig 4.3a and the explanation given above, the residence time distribution is a smooth curve with a maximum corresponding to the separatrix. In all other cases, the distributions are not smooth on account of chaotic scattering as seen in Figure 4.4 which shows the individual residence time distributions for all the aforementioned nine cases on a magnified scale as a function of the initial upstream gradient offsets. It is readily evident from these plots that the regular peak of the residence time distribution for $C = 0$ bursts into chaotic peaks as $C > 0$ and the width of the chaotic scattering interval gradually increases as the spheroid approach the tumbling orbit($C = \infty$).

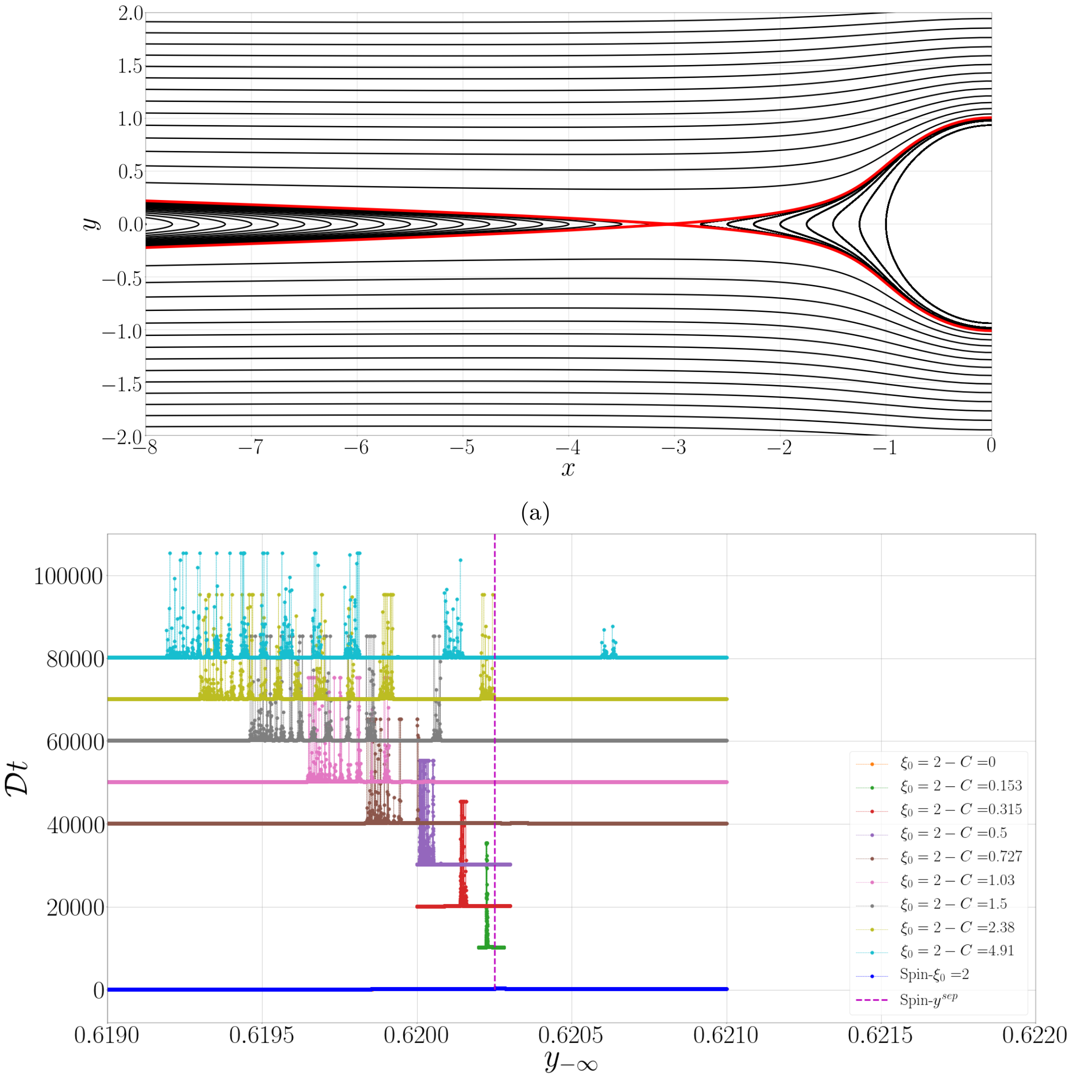

(a)

(b)

Fig. 4.3 Prolate spheroid of $\xi_0 = 2(\kappa = 1.15)$ in a hyperbolic linear flow with $\alpha = 0.001$: (a) Streamline configuration around a spinning spheroid only in the left half of the flow-gradient plane (on account of symmetry about the gradient axis); the red curves represent the separatrices. (b) Comparison of the chaotic scattering intervals that emerge in the residence time distributions, for fluid elements that begin at $x_{-\infty} = -20$, for different C's (C =0, 0.153, 0.315, 0.5, 0.727, 1.03, 1.5, 2.38 and 4.91). The purple dotted lone denotes the upstream gradient offset for the separatrix for the spinning($C = 0$) case.

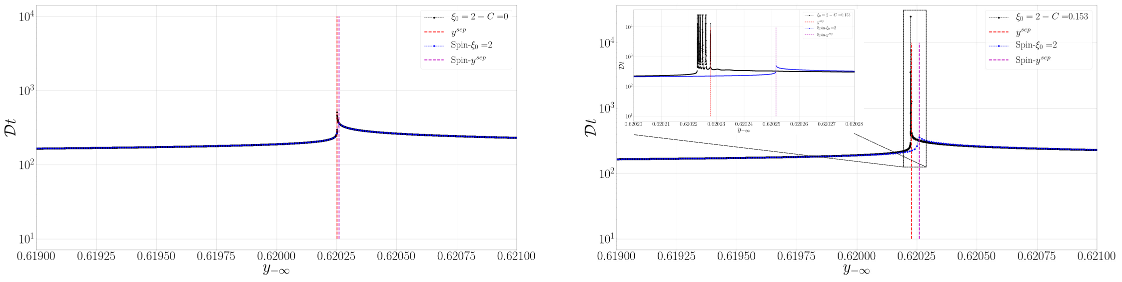

(a) $\theta_{j,-\infty} = 0$ (b) $\theta_{j,-\infty} = 10$

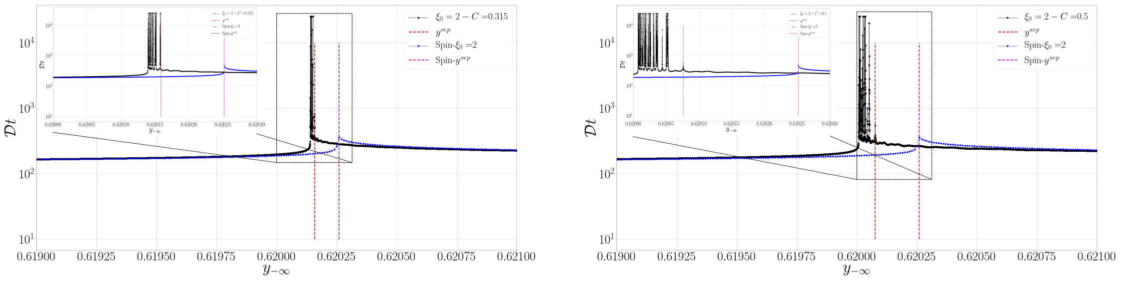

(c) $\theta_{j,-\infty} = 20$ (d) $\theta_{j,-\infty} = 30$

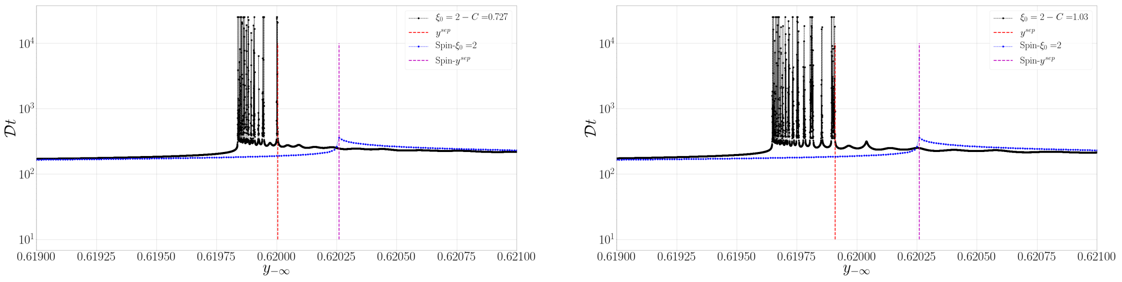

(e) $\theta_{j,-\infty} = 40$ (f) $\theta_{j,-\infty} = 50$

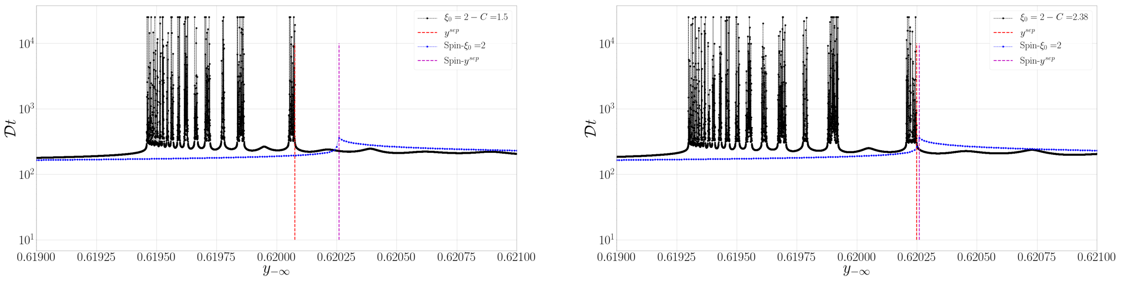

(g) $\theta_{j,-\infty} = 60$ (h) $\theta_{j,-\infty} = 70$

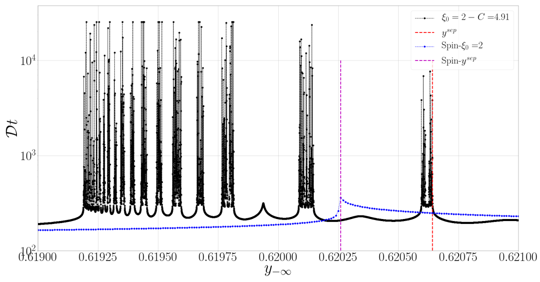

(i) $\theta_{j,-\infty} = 80$

Fig. 4.4 Residence time distributions for a prolate spheroid of $\xi_0 = 2(\kappa = 1.15)$ rotating along different Jeffrey orbits. The blue curve represents the residence time for the spinning case, and is shown for comparison in each of the subfigures. The red and the magenta dashed lines represent the upstream gradient offsets denoting the boundary of the chaos for the precessing spheroid and the separatrix of the spinning one, respectively.

Part II

Discretization of stochastic partial differential equations

Chapter 5

Introduction

Thermal fluctuations are an essential part of complex phenomena as diverse as Brownian motion in colloidal suspensions[12, 94], concentration fluctuations in semi-dilute polymer solutions [46, 78, 111], capillary waves at fluctuating interfaces[89, 40, 97], critical dynamics in binary mixtures [34, 35, 110, 105] and pattern formation [28, 79]. In these systems, stochastic partial differential equations(PDE) are used to describe the time evolution of conserved quantities. Examples of such PDE's include the fluctuating Cahn-Hilliard-Cook equation [23, 26, 96], the fluctuating Navier-Stokes equations of Landau and Lifshitz[64], model-H dynamics of phase transition[49], the fluctuating lubrication equation [99, 31] and models of electrohydrodynamic instabilities in electrospinning experiments [66]. The fluxes, in the conservation laws, which are coarse-grained expressions of microscopically reversible Hamiltonian dynamics, must satisfy an important constraint: the stochastic part of the flux cannot be chosen independently but must be related through a detailed balance condition, also known as the Fluctuation Dissipation Theorem(FDT), to the irreversible part of the flux [115]. This relation is necessary to ensure that the coarse-grained dynamics yields a stationary state with a Gibbs distribution, or in other words, that the dynamics expressed by the conservation law is consistent with micro-reversibility.

Discretization in space *and* time is a necessary step in seeking numerical solutions to any PDE including stochastic conservation laws. The discretization of the *spatial* part of the conservation law commonly requires discrete analogs of the vector differential operators - the gradient, divergence, curl and of the Laplacian. It is well understood that the discrete differential operators do not always inherit all properties of the continuum operators. In particular, special care is needed to preserve the continuum "div-grad-curl" identities like the vanishing of the discrete curl of a discrete gradient or of the discrete divergence of a discrete curl. The discretization of the stochastic flux is more involved compared to Langevin equations as it is the *divergence* of a Gaussian random field. This is due to the fact that for detailed balance in a stochastic conservation law, it is necessary to ensure that the discrete divergence of a discrete gradient is identical to the discrete Laplacian (see below). A typical discrete representations of these operators, constructed in the setting of deterministic conservation laws, do not satisfy this last property, as at the discrete level $\boldsymbol{\nabla} \cdot \boldsymbol{\nabla} \neq \nabla^2$. Their use in stochastic conservation laws results in a violation of the detailed balance condition [86, 91, 51].

Discrete differential operators also fail to preserve symmetries, such as isotropy, of their analytical counterpart. For instance, the error in the discrete Laplacian, obtained through second-order central difference, is anisotropic at leading order and constrains the dynamics of the physical problem in the principal directions of the lattice which are the x, y, and z axes for a 3D Cartesian grid, as the grid points in the other directions are not taken into consideration while writing the respective stencil for the discrete Laplacian operator[90]. Use of larger stencils improves the accuracy of the result, but the physical solution of the problem still gets infused with anisotropy. So, here we are looking for discrete operators having the Fourier spectra as $\mathcal{F}(\tilde{\nabla}^2\phi) = -k^2\mathcal{F}(\phi) + G(k^4)\mathcal{F}(\phi) + \mathcal{O}(k^6)$, where $\mathcal{F}$ is the Fourier transform operator and $G(k^4)$ being some isotropic representation of the leading order error.

The necessity of a consistent discretization of the vector differential operators for satisfying in model H[49] was first expressed in the work of Delgado et. al.[32] and Garcia et. al.[36] for the finite-volume discretization of the compressible isothermal fluctuating hydrodynamics at nanoscale and the same for stochastic conservation law obtained from a large-volume expansion of the chemical master equation for reacting and diffusing species respectively. Thampi et. al.[107] presented both spectral and finite-volume discretizations of the order parameter equation in model H, using fluctuating discrete kinetic theory to describe momentum conservation. Several alternatives to explicit temporal integration has been explored by Torre et. al [33]. The issue of preservation of vector identities in the discrete operators was addressed earlier by interpolation based formulation on irregular mesh of nodal points for finite difference and finite element[69], and *mimetic*[17, 50] discretization. Similarly, the preservation of symmetry of the differential operators in the discrete space was achieved through lattice differential operators[60, 107, 90], where the discretizations along the diagonal directions, apart from the principal directions for a simple cubic(SC) spatial grid were considered. They showed that such a discretization provides an elegant way of deriving Laplacians with isotropic discretization error. A class of lattice differential operators satisfying both isotropy and fundamental vector identities needed for preservation of FDT at the lattice level has been recently addressed by [10].

In this part of this thesis we generalise the implementation of the isotropic lattice differential operators[106, 90] on stochastic PDE's discretized on different class of lattices, namely simple-cubic(SC) and body-centred-cubic(BCC) lattices and analize the conservation of detailed balance in the discrete space. Here, in the Chapter 6 we discussed the recently proposed[10] finite-difference discretization of a stochastic conservation law following a semi-discretization strategy and illustrate our general results with the specific example of model B[49] and Fluctuating Navier-Stokes(FNS)[64]. The stochastic partial differential equation is first discretized in space to yield a set of coupled stochastic ordinary differential equations. In this, we use discretizations of the gradient and divergence that ensure isotropic truncation errors to leading order in lattice spacing [106, 90]. We then *define* the Laplacian to be a composition of these discrete operators, so that the identity $\nabla^2 = \boldsymbol{\nabla}\cdot\boldsymbol{\nabla}$ is satisfied by construction. The resulting Laplacian operator is negative semi-definite with a trivial null space: the only eigenvector with a zero eigenvalue is the constant. The support of this Laplacian, though, is larger than those of comparable accuracy commonly used in finite-difference methods. In Chapter 7 we extend[74] the concept of lattice differential operators by implementing the same on a body-centered-cubic(BCC) spatial grid. By construction the lattice operators preserve symmetries like isotropy at least at the leading order and also by definition satisfies all the fundamental vector identities of differential operators. We advocate the use of BCC grid over SC in finite difference formalism, as not only the discrete differential operators are better approximated, complex shapes and domain geometries are also better represented [81].

Chapter 6

Isotropic lattice operators for stochastic conservation laws preserving detailed balance

As discussed in the Introduction, in this chapter we derive a numerical scheme for the discretization of stochastic PDE's, which preserves the FDT at the lattice level. Here we first present the numerical solutions of stochastic diffusion which is represented by Model B[49]. [1] It is observed in the following sections that, naive spatial discretization of these stochastic partial differential equations leads to the failure of the Fluctuation Dissipation Theorem(FDT) at the discrete level as most of the lattice operators fail to preserve the fundamental vector identities in the discrete space. To illustrate this with a simple example, let us consider the standard central - difference stencils in one dimension, for which

$$\tilde{\nabla}\phi(x) = \frac{\phi(x+\delta x) - \phi(x-\delta x)}{2\delta x}, \tag{6.1}$$

$$\tilde{\nabla}^2\phi(x) = \frac{\phi(x+\delta x) - 2\phi(x) + \phi(x-\delta x)}{(\delta x)^2}. \tag{6.2}$$

But, if we *define* the discrete Laplacian as,

$$\tilde{\nabla}^2\phi = \tilde{\nabla}\cdot\tilde{\nabla}\phi = \frac{\phi(x+2\delta x) - 2\phi(x) + \phi(x-2\delta x)}{4(\delta x)^2}, \tag{6.3}$$

where it is evident that $\tilde{\nabla}\cdot\tilde{\nabla} \neq \tilde{\nabla}^2$ and using Fourier transform of Eq.6.1 and Eq.6.2 it can be shown that,

$$\frac{\tilde{\nabla}_{\boldsymbol{q}}\cdot\tilde{\nabla}_{\boldsymbol{q}}}{\tilde{\nabla}^2_{\boldsymbol{q}}} = \frac{\cos(2q\delta x) - 1}{4\cos(q\delta x) - 4}, \tag{6.4}$$

where the subscripts indicate the Fourier transforms of the respective operators and are specific functions of the wave-number $\boldsymbol{q}$. This expression tends to unity as q tends to zero but is less than unity for all other values of q in the first Brillouin zone $|q| \leq \pi$. Therefore, the use of such a discretization will, even for a (hypothetically) perfect temporal integrator, introduce spurious wave number dependence in

---

[1] The findings of this chapter are published in [10]

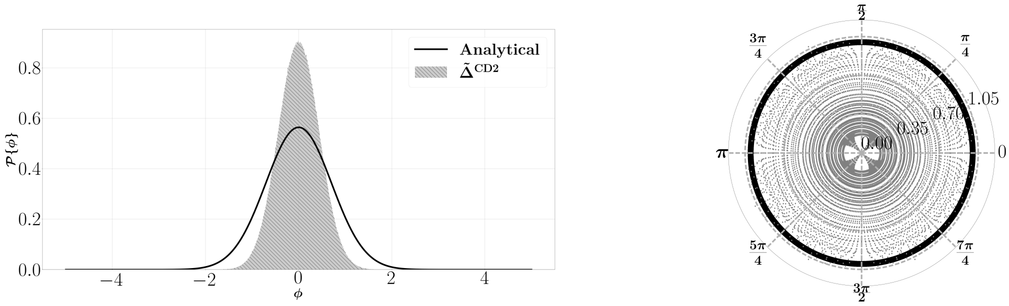

(a) (b)

Fig. 6.1 (a) Probability distribution and (b) polar spectra of the structure factor and compared with the analytical result(shown in black curve).

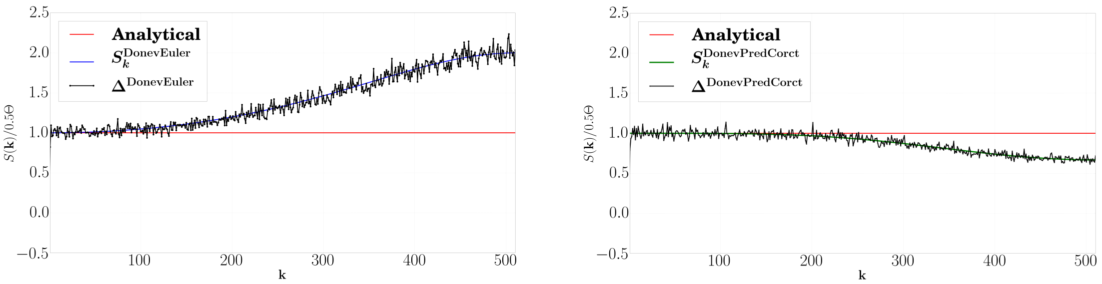

(a) (b)

Fig. 6.2 Averaged spectra of the structure factor calculated using (a) CD2 and (b) predictor corrector methods and compared with the analytical result(shown in red curve).

the two-point correlation. This artifact of the standard discretization has been noted earlier [24, 107]. We present the following plots showing the probability distribution of the order parameter(ϕ) along with the averaged and the polar spectra of the structure factors from the numerical solution of the stochastic diffusion equation using second order central difference(CD2) and other predictor-corrector algorithms and compared them with the analytical results. The departure from the analytical results is quite prevalent in all these cases; it is also observed in the averaged spectra the accumulation or deficit of energy in the higher wave numbers. We investigate this phenomenon in the following sections in more detail and also discuss the possible solution to that.

6.1 Model B

In this section, we briefly review model B dynamics, a stochastic partial differential equation for a conserved scalar order parameter field $\phi(\boldsymbol{x}, t)$ whose dynamics is driven by a competition between deterministic thermodynamic forces and stochastic forces of thermal origin [49, 23, 26]. The equation of motion is

$$\partial_t \phi = \boldsymbol{\nabla} \cdot \left(M \boldsymbol{\nabla} \frac{\delta \mathcal{F}}{\delta \phi} \right) + \boldsymbol{\nabla} \cdot \boldsymbol{\xi}, \tag{6.5}$$

where M is the order parameter mobility and $\mathcal{F}$, the Landau free energy, is a functional of the order parameter

$$\mathcal{F} = \int d^d\boldsymbol{x} \left[f(\phi) + \frac{1}{2} K (\boldsymbol{\nabla}\phi(\boldsymbol{x},t))^2 \right]. \tag{6.6}$$

The local part of the free energy density is typically taken to be $f(\phi) = \frac{1}{2}A\phi^2 + \frac{1}{4}B\phi^4$, where A can be either positive or negative but B is always positive. The positive coefficient K in the non-local part is related to the energy cost for gradients in the order parameter. The stochastic flux $\boldsymbol{\xi}(\boldsymbol{x},t)$ is a zero-mean Gaussian random field whose correlation is local in both space and time,

$$\langle \boldsymbol{\xi}(\mathbf{x},t)\boldsymbol{\xi}(\mathbf{x}',t')\rangle = 2k_BTM\,\boldsymbol{I}\,\delta(t-t')\delta(\mathbf{x}'-\mathbf{x}), \tag{6.7}$$

where k_B is the Boltzmann constant, T is the temperature and $\boldsymbol{I}$ is the identity matrix in the space of Cartesian indices. This fluctuation-dissipation relation for the stochastic flux ensures that the stationary probability distribution is

$$P[\phi(\boldsymbol{x},t)] = Z^{-1}\exp\left(-\beta\mathcal{F}\right),$$

where Z is the partition function.

From the point of view of renormalization group, Model B has a Gaussian fixed point corresponding to the parameters $A, K > 0$ and $B = 0$[23, 26]. It also has a non-trivial Wilson-Fisher fixed point when $A = 0$ and $B, K > 0$. In addition, it allows for two-phase coexistence between the phases $\phi = \pm 1$ when $A < 0$ and $B, K > 0$. The "domain wall" between these two phases is described by the ϕ^4 solution. Correlation functions in all three cases can be calculated in closed form.

Here, our principal interest is in the Gaussian fixed point. The free energy is quadratic and the order parameter distribution, consequently, is Gaussian. The two-point correlation determines all remaining correlation functions. In Fourier space, it is

$$\langle \phi(\boldsymbol{q})\phi(-\boldsymbol{q})\rangle = \frac{k_BT}{A+Kq^2}. \tag{6.8}$$

A first check on the accuracy of the discrete numerical method is provided by a comparison with the two-point correlation function. Away from the Gaussian fixed point, a more stringent check is provided by a comparison with the distribution of the order parameter. Below, we use both these checks to validate our numerical methods.

6.2 Spatial discretization and detailed balance

In this section we discretize Model B in space to show that naive discretizations leads to breakdown of detailed balance, shown in Figure 6.2, and how detailed balance can be restored by a redefinition of the discrete Laplacian. This analysis is best illustrated without the additional complication of order parameter non-linearity and therefore, we shall restrict ourselves to the Gaussian phase, though the results obtained will be generally applicable. In the Gaussian phase the equation of motion is linear and, for a constant mobility, takes the form

$$\partial_t\phi(\boldsymbol{x},t) = M\nabla^2(A-K\nabla^2)\phi(\boldsymbol{x},t) + \boldsymbol{\nabla}\cdot\boldsymbol{\xi}(\boldsymbol{x},t). \tag{6.9}$$

Let us denote the discrete gradient, divergence and Laplacian by $\tilde{\boldsymbol{\nabla}}$, $\tilde{\boldsymbol{\nabla}}\boldsymbol{\cdot}$ and $\tilde{\nabla}^2$ respectively. It follows that the equation of motion of the discretely sampled field is

$$\partial_t \phi(\boldsymbol{x},t) = M\tilde{\nabla}^2(A - K\tilde{\nabla}^2)\phi(\boldsymbol{x},t) + \tilde{\boldsymbol{\nabla}} \cdot \boldsymbol{\xi}. \tag{6.10}$$

It is then a straightforward exercise to show, using the fluctuation-dissipation relation for the random flux, that the two-point correlation function of the Fourier modes of the order parameter is given by

$$\langle \phi(\boldsymbol{q})\phi(-\boldsymbol{q})\rangle = \left(\frac{\tilde{\boldsymbol{\nabla}}_{\boldsymbol{q}} \cdot \tilde{\boldsymbol{\nabla}}_{\boldsymbol{q}}}{\tilde{\nabla}^2_{\boldsymbol{q}}}\right) \frac{k_B T}{A - K\tilde{\nabla}^2_{\boldsymbol{q}}}, \tag{6.11}$$

Comparing with the two-point correlation function of the continuum theory, Eq.6.8, it is evident that the discrete two-point correlation function will contain the factor

$$\mathcal{R}(\boldsymbol{q}) = \frac{\tilde{\boldsymbol{\nabla}}_{\boldsymbol{q}} \cdot \tilde{\boldsymbol{\nabla}}_{\boldsymbol{q}}}{\tilde{\nabla}^2_{\boldsymbol{q}}}, \tag{6.12}$$

which, generally, will differ from unity. If the discrete operators are such that $\mathcal{R}(\boldsymbol{q}) = 1$ and discrete Laplacian $\tilde{\nabla}^2_q = -q^2 + O(q^4)$, then Eq.(6.11) and Eq.(6.8) differs from each other by a term which is $O(K\,q^4)$ at least. To ensure that this "equilibrium ratio" is indeed unity for all wave numbers requires that the Fourier transform of the discrete gradient, divergence and Laplacian operators be related exactly as in the continuum. So, if the discrete Laplacian is *defined* as Eq.6.3 and repeating the above exercise shows that $\mathcal{R}(\boldsymbol{q})$ is unity for *all* wave numbers and the semi-discretization ensures that the correlation function approximates that of the continuum and it is free of spurious wave number dependent contributions. The Fourier transform of this Laplacian is

$$\tilde{\nabla}^2_{\mathbf{q}} = \frac{\cos(2q\delta x) - 1}{2(\delta x)^2} = -\frac{\sin^2(q\delta x)}{(\delta x)^2} \tag{6.13}$$

and is obviously negative semi-definite. The only null eigenvector in the first Brillouin zone is a constant.

6.2.1 Explicit time integrators

The use of the Laplacian in Eq.6.3 in conventional time discretization schemes will lead to reduced overall accuracy, which can be seen by considering a simple but illustrative example of the diffusion equation

$$\partial_t \phi = D\,\partial_x^2 \phi \tag{6.14}$$

for the scalar field ϕ. Using central differences and forward Euler for spatial and temporal discretization respectively, the resulting difference equation is

$$\phi_i^{n+1} = \phi_i^n + \frac{\alpha}{(m+1)^2}\left[\phi^n_{i+m+1} + \phi^n_{i-m-1} - 2\phi_i^n\right], \tag{6.15}$$

where $\phi_i^n \equiv \phi(i\delta x, n\Delta t)$ and $\alpha = D\,\Delta t/\delta x^2$ is the Courant–Friedrichs–Lewy (CFL) number. The Laplacian operators of Eq.6.2 and Eq.6.3 correspond to $m = 0$ and $m = 1$ respectively. The numerical stability of the difference scheme can be analyzed using the von Neumann method, where the dynamical variable ϕ_i^n is written in the discrete Fourier domain as

$$\phi_i^n = \lambda^n(q)\exp[Iqx_i], \tag{6.16}$$

with $\lambda(q)$ being the amplification factor, $x_i = i\delta x$ and I is the complex root of unity. The amplification factor for Eq.6.15 is easily obtained to be

$$\lambda(q) = 1 - \frac{4\alpha}{(m+1)^2}\sin^2\left[\frac{(m+1)\,q\delta x}{2}\right] \tag{6.17}$$

and thus stability, $|\lambda| < 1$, requires

$$0 \leq \alpha \leq \frac{(m+1)^2}{2}. \tag{6.18}$$

The continuum limit of Eq.6.15 under the "diffusive scaling" $\delta x \sim O(\epsilon)$ and $\Delta t \sim O(\epsilon^2)$, correct to $O(\epsilon^4)$, is

$$\frac{\partial\phi}{\partial t} + \frac{\Delta t}{2}\frac{\partial^2\phi}{\partial t^2} = D\left(\frac{\partial^2\phi}{\partial x^2} + \frac{(m+1)^2\delta x^2}{12}\frac{\partial^4\phi}{\partial x^4}\right). \tag{6.19}$$

This equation can be simplified using the Cauchy-Kowalewsky backward error analysis, where all higher order time and mixed derivatives are estimated by space derivatives obtained using the differential equation itself. For example, by taking a derivative in time of the evolution Eq.6.19, we can estimate

$$\frac{\partial^2\phi}{\partial t^2} = D^2\frac{\partial^4\phi}{\partial x^4} + O(\epsilon^2). \tag{6.20}$$

Thus, the effective differential equation with an error of $O(\epsilon^4)$ is

$$\frac{\partial\phi}{\partial t} = D\frac{\partial^2\phi}{\partial x^2} + \frac{D\,\delta x^2}{2}\frac{\partial^4\phi}{\partial x^4}\mathcal{I}^{\mathrm{CD2}}(m,\alpha), \tag{6.21}$$

where the transport coefficient associated with the biharmonic operator is

$$\mathcal{I}^{\mathrm{CD2}}(m,\alpha) = \frac{(m+1)^2}{6} - \alpha.$$

Based on this effective differential equation, we can analyze the accuracy for different values of m and thus the effect of a wider stencil on accuracy. The trade-off in using the "mimetic" stencil is now obvious: the wider stencil has a lower accuracy as $|\mathcal{I}^{\mathrm{CD2}}(1,\alpha)| > |\mathcal{I}^{\mathrm{CD2}}(0,\alpha)|$ in the parameter range $0 \leq \alpha \leq 1/2$ where the schemes are stable.

6.2.2 Delayed time integrators

The above shortcoming of the combination of the spatial "mimetic" Laplacian and the temporal explicit integrator can be remedied by using a recently introduced delayed-in-time integration scheme [80]. This scheme is motivated by the observation that computing derivatives on a wider stencil, while using spatial data from earlier times, can dramatically improve both stability and accuracy [80].

The delayed integrator applied to Eq.6.14 gives

$$\phi_i^{n+1} = \phi_i^n + \frac{\alpha}{(m+1)^2}\left[\phi_{i+m+1}^{n-m} + \phi_{i-m-1}^{n-m} - 2\phi_i^{n-m}\right], \tag{6.22}$$

which should be compared with Eq.6.15 for $m = 0$. The amplification factor for this scheme obeys

$$\lambda^{m+1} - \lambda^{m} + \frac{4\alpha}{(m+1)^2}\sin^2\left(\frac{(m+1)\,q\delta x}{2}\right) = 0, \tag{6.23}$$

which can be solved for $m = 1$ to obtain as

$$\lambda^2 - \lambda + \alpha\sin^2(q\delta x) = 0 \tag{6.24}$$

$$\Rightarrow \lambda = \frac{1}{2}\left(1 \pm \sqrt{1 - 4\alpha\sin^2(q\delta x)}\right). \tag{6.25}$$

It is observed from Eq.2.25 that the amplification factor λ has real values as long as $\alpha \le 1/4$; but if $\alpha > 1/4$ then λ becomes imaginary. To satisfy the stability of the scheme shown in Eq.6.22(for $m = 1$), one should have $|\lambda| \le 1$, which for imaginary root implies the condition of the multiplication of the roots for Eq.2.24, and that leads to $\alpha\sin^2(q\delta x) < 1$ and we have the stability condition as

$$\alpha \le 1,$$

which implies a gain in stability compared to $m = 0$. However, the gain is less than naive use of wider stencil (Eq.6.18). Here, we remind that wider stencil leads to better stability but much lower accuracy. However, the delayed scheme removes this problem of lower accuracy associated with wider stencil. This can be seen from the effective differential equation corresponding to the delayed scheme. In order to obtain such effective equation, similar to previous section, we use Cauchy-Kowalewski procedure. We write Eq.6.22 in differential form using Taylor series as

$$\frac{\partial\phi}{\partial t} + \frac{\delta t}{2}\frac{\partial^2\phi}{\partial t^2} = D\left(\frac{\partial^2\phi}{\partial x^2} - m\delta t\frac{\partial^3\phi}{\partial t\partial x^2} + \frac{(m+1)^2\delta x^2}{12}\frac{\partial^4\phi}{\partial x^4}\right) + O(\epsilon^3) \tag{6.26}$$

and then replacing the time and the mixed derivatives using evolution equation (Eq.6.26), to obtain the effective differential equation at the leading order as

$$\frac{\partial\phi}{\partial t} = D\frac{\partial^2\phi}{\partial x^2} + \frac{D\,\delta x^2}{2}\frac{\partial^4\phi}{\partial x^4}\mathcal{I}^{\text{Delayed}}(m,\alpha) + O(\epsilon^3), \tag{6.27}$$

where,

$$\mathcal{I}^{\text{Delayed}}(m,\alpha) = \frac{(m+1)^2}{6} - \alpha(2m+1).$$

Thus, for $m = 1$, Eq.6.27 implies

$$\partial_t\phi = D\,\partial_x^2\phi + \frac{D\,\delta x^2}{2}\left[\frac{2}{3} - 3\alpha\right]\partial_x^4\phi. \tag{6.28}$$

Thus, for $\alpha > 0.25$ the delayed scheme has higher accuracy $\mathcal{I}^{\text{Delayed}}(1,\alpha)$ than the standard CD2 schemes with $\mathcal{I}^{\text{CD2}}(0,\alpha)$ as well as naive scheme with wider stencil $\mathcal{I}^{\text{CD2}}(1,\alpha)$. This is illustrated in Fig.6.3, where the pre-factors $\mathcal{I}^{\text{CD2}}(m,\alpha)$ and $\mathcal{I}^{\text{Delayed}}(m,\alpha)$, are plotted with respect to the CFL(α)

Thus, long time integration can be efficiently performed by the delayed scheme, as it enhances the stability by a factor 2.0 as compared to that of the usual CD2 scheme, without reduction in accuracy. This is evident from the schematics (Fig.6.4), which shows that data taken from past requires wider stencil($2\delta x$) and thus, widening of stencil compensates for error due to the time delay.

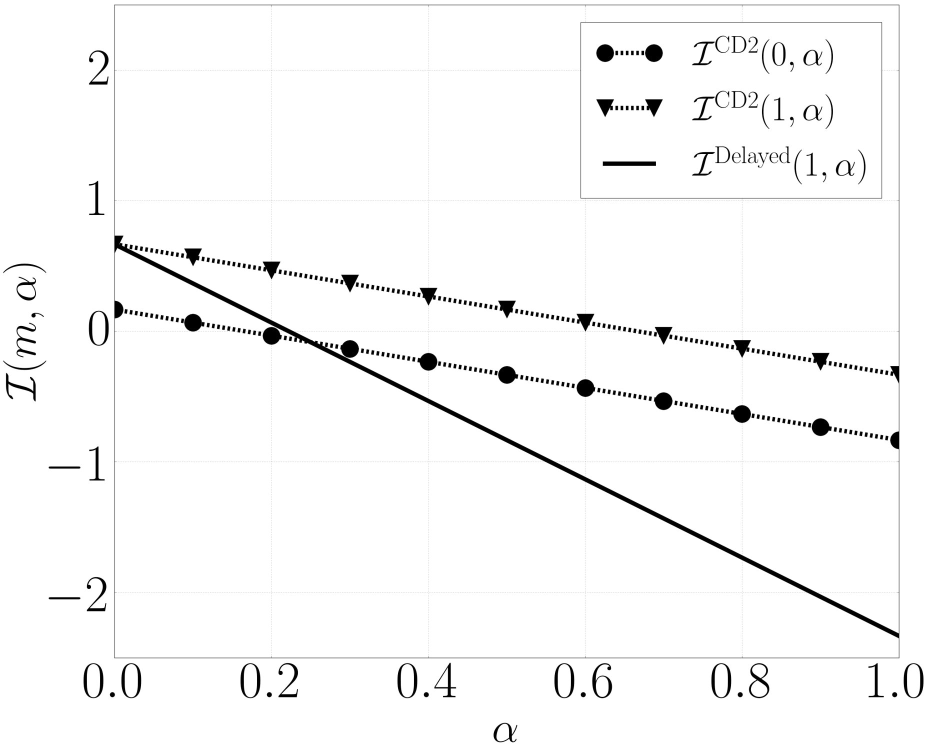

Fig. 6.3 Variation of pre-factors $\mathcal{I}^{\mathrm{CD2}}(m,\alpha)$ and $\mathcal{I}^{\mathrm{Delayed}}(m,\alpha)$ of with the CFL number α.

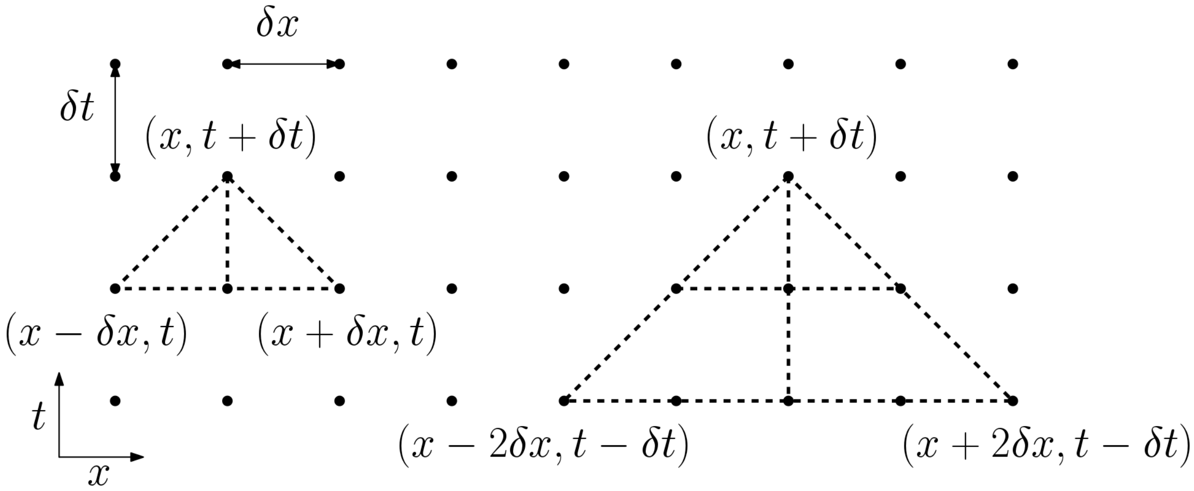

Fig. 6.4 Stencil for Standard(left) and Delayed(right) schemes and domain of dependence.

6.2.3 Delayed time integrators in multi-dimensional space

In last section, we have shown that the delayed scheme leads to better stability and accuracy for discretized diffusion equation in one dimension. However, for the multi-dimensional extension of the delayed scheme,

$$\phi_i^{n+1} = \phi_i^n + D\,\delta t \tilde{\Delta}\phi_i^{n-1}, \tag{6.29}$$

the increase in accuracy and stability requires further restrictions on the form of the discrete operators. This can be seen by repeating the analysis of previous section on multi-dimensional scheme. In this case, similar to the previous section, we write Eq.6.22 in differential form using Taylor series as

$$\frac{\partial\phi}{\partial t} + \frac{\delta t}{2}\frac{\partial^2\phi}{\partial t^2} = D\left(\tilde{\Delta}\phi - \delta t\frac{\partial\tilde{\Delta}\phi}{\partial t}\right). \tag{6.30}$$

If the discrete Laplacian preserves an isotropic structure at least at the leading order, with a as a stencil dependent constant, i.e,

$$\tilde{\Delta} = \nabla^2 + a\delta x^2\nabla^2\nabla^2 + \cdots, \tag{6.31}$$

the effective differential equation for the discrete analog of diffusion equation can be written as

$$\partial_t\phi = D\,\nabla^2\left[1 + \left(a\,\delta x^2 - \frac{3D\,\Delta t}{2}\right)\nabla^2\right]\phi. \tag{6.32}$$

Similar to the 1-D case, this equation for the delayed scheme also has better stability and accuracy. However, conventional discrete operators such as central difference operators do not satisfy Eq.6.31[106, 83, 84]m which can be seen by Taylor series expansion of central difference Laplacian operator in 3-D as:

$$\tilde{\Delta}^{\mathrm{CD2}} = \nabla^2 + \frac{\delta x^2}{12}(\partial_x^4 + \partial_y^4 + \partial_z^4). \tag{6.33}$$

The Fourier spectra of the above Eq.6.5, in the low wave number limit may be obtained as,

$$\tilde{\Delta}^{\mathrm{CD2}}(\boldsymbol{q}) = -q^2 + \frac{1}{12}(q_x^4 + q_y^4 + q_z^4)\delta x^2 + \mathcal{O}(\delta x^4), \tag{6.34}$$

where the leading order anisotropy of the error is readily evident. This anisotropic behaviour in the leading order error is illustrated in the polar spectra of the Green's function of the diffusion operators using CD2 in Figure 6.5.

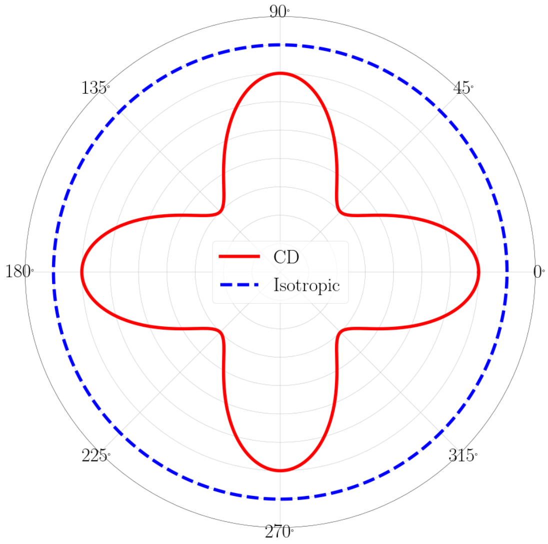

Fig. 6.5 Leading order error distribution for the Green's functions for the Laplacian using CD2. I thank **Mr. Nishant Soni**(EMU, JNCASR) for proving the Green's function calculation

So, to satisfy FDT at the discrete level in higher dimensional stochastic PDE's the discrete differential operators should be isotropic, at least at the leading order, as shown in 6.31 and a comprehensive study of these operators is furnished in the next chapter.

Chapter 7

Isotropic lattice operators on a class of lattices

In the previous chapter we see that the conservation of the FDT in the discrete space for multidimensional stochastic PDE's will require the discrete differential operators to have an isotropic error, at least at the leading order. The derivation of these isotropic operators on simple cubic(SC) and body-centred-cubic(BCC) lattice-grids stems from the lattice kinetic models[106], and part from preserving detailed balance these isotropic discrete operators also preserve the symmetries of their analytical counterpart[90]. In this chapter we present a more comprehensive study of the lattice operators on both SC and BCC lattices and present some benchmarking numerical simulation results to show the superiority of the BCC operators over the SC ones. [1]

7.1 Discrete lattice operators

Adopting the nomenclature from the lattice kinetic theory a typical computational grid of these discrete lattice operators are often called a $DnQm$ lattice, where n is the dimension and m is the number of discrete velocities/connectors[90]. The Figure 7.1 shows he computational domain discretized in terms of a D3Q27 cubic shells/lattices of dimension $\delta x \times \delta x \times \delta x$, along with the respective projections on the 2D lattice. The cubic shell is centred around the grid point i denoted by the radius vector $\boldsymbol{r}$. Following a cell dynamical terminology, the neighbouring grid points are denoted by 'NN(Nearest Neighbour)', 'NNN(Nest Nearest Neighbour)', 'NNNN(Next Next Nearest Neighbour)' and so on, which are indicated in Figure 7.1. There are 27 connecting vectors, denoted by $\boldsymbol{c}_i$), which connect the centre i to the rest of the neighbours. Among this 27 connecting vectors, 6 of them connect the face centres (NN) along the corresponding Cartesian axis, and have the form $(\pm1, 0, 0)$; 12 of them connect the edge centers(NNN) and are confined to the respective Cartesian plane having the form $(\pm1, \pm1, 0)$; and the final 8 connecting vectors connect the vertices(NNNN) of the cubic shell, having the form $(\pm1, \pm1, \pm1)$. From a lattice kinetic theory perspective, it can be observed that the connecting vectors($\boldsymbol{c_i}$) represent the discreet velocities and following Lattice Boltzmann(LB) terminology, the aforementioned 6, 12 and 8 velocities correspond to the "Energy Shells" 1(NN), 2(NNN) and 3(NNNN) respectively, whereas the centre i lies in the Energy Shell 0[90].

---

[1] The findings of this chapter are published in [74]

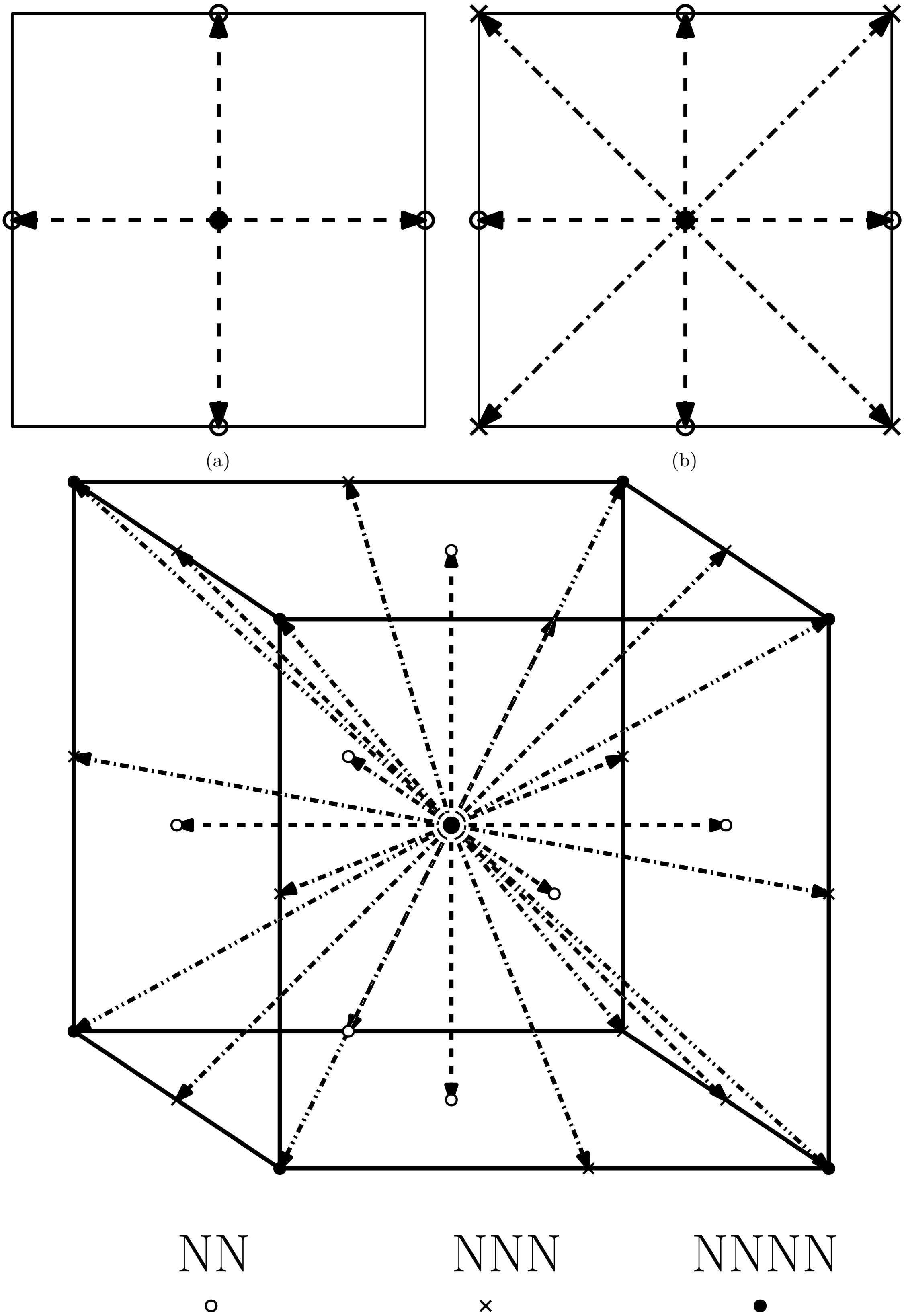

(a) (b)

(c)

Fig. 7.1 Typical computational grids on an SC lattice; the NN, NNN and NNNN are represented by a circle, a cross and a dot, respectively. (a) D2Q5 lattice, (b) a D2Q9 lattice (c) a D3Q27 lattice

The discrete lattice operators for *gradient*, *divergence* and *curl*, defined on a $DnQm$ lattice[90]:

$$\tilde{\boldsymbol{\nabla}}^{\mathrm{iso}}\boldsymbol{\Phi} = \frac{1}{\delta x}\sum_{i=1}^{N} w_i \hat{\boldsymbol{c}}_{\boldsymbol{i}} \boldsymbol{\Phi}\left(\boldsymbol{r}_i + \boldsymbol{c}_i\right), \tag{7.1}$$

$$\tilde{\boldsymbol{\nabla}}^{\mathrm{iso}} \cdot \boldsymbol{\Phi} = \frac{1}{\delta x}\sum_{i=1}^{N} w_i \hat{\boldsymbol{c}}_{\boldsymbol{i}} \cdot \boldsymbol{\Phi}\left(\boldsymbol{r}_i + \boldsymbol{c}_i\right), \tag{7.2}$$

$$\tilde{\boldsymbol{\nabla}}^{\mathrm{iso}} \times \boldsymbol{\Phi} = \frac{1}{\delta x}\sum_{i=1}^{N} w_i \hat{\boldsymbol{c}}_{\boldsymbol{i}} \times \boldsymbol{\Phi}\left(\boldsymbol{r}_i + \boldsymbol{c}_i\right), \tag{7.3}$$

Where w_i denotes the weights associated with each of the connectors $\hat{\boldsymbol{c}}_{\boldsymbol{i}}$. It is evident that to satisfy isotropy at the discrete space, at least at the fourth order, the following necessary conditions have to be satisfied[107],

$$\sum_{i=0}^{m} w_i = 1, \tag{7.4}$$

$$\sum_{i=0}^{m} c_{i,\alpha} c_{i,\beta} w_i = T\delta_{\alpha\beta}, \tag{7.5}$$

$$\sum_{i=0}^{m} c_{i,\alpha} c_{i,\beta} c_{i,\gamma} c_{i,\eta} w_i = T^2 \Delta_{\alpha\beta\gamma\eta}, \tag{7.6}$$

where Greek indices denote Cartesian directions, index i denotes the links, and T is a lattice dependent constant and for a cubic lattice with $\delta x = 1$ it can be shown that $T = 1/3$.

One could adopt the following recursive method[90] to find the isotropic lattice operators(7.1) by considering a general discrete operator in the following form:

$$D_{\boldsymbol{s}} \equiv \frac{1}{T}\sum_{i=0}^{m} w_i e^{\boldsymbol{c}_i \cdot \boldsymbol{s}}, \quad \boldsymbol{s} \equiv \boldsymbol{\nabla}, \tag{7.7}$$

which can be applied on a scalar function $\varphi(\boldsymbol{r})$ defined on this lattice as:

$$D_{\boldsymbol{s}}\left[\varphi(\boldsymbol{r})\right] = \frac{1}{T}\sum_{i=0}^{m} w_i e^{\boldsymbol{c}_i \cdot \boldsymbol{s}} \varphi(\boldsymbol{r}) = \sum_{i=0}^{m} w_i \varphi(\boldsymbol{r} + \boldsymbol{c}_i). \tag{7.8}$$

Considering the following two transformations one may obtain,

$$\mathcal{F}(\boldsymbol{r}) = 2\left(D_{\boldsymbol{s}} - \frac{1}{T}\right)\varphi(\boldsymbol{r}), \tag{7.9}$$

$$\mathcal{G}(\boldsymbol{r}) = \frac{dD}{d\boldsymbol{s}}\varphi(\boldsymbol{r}). \tag{7.10}$$

	N(2D projection)	D2Q9	D3Q27
0	1	0	0
NN	6(4)	1/3	1/3
NNN	12(4)	1/12	0
NNNN	8(0)	NA	1/24

Table 7.1 Weights for D2Q9 and D3Q27 lattices on an SC grid, with N being the number of neighbours.

Using Eq.(7.8) and the above transformations(Eq(7.9) and Eq.(7.10)) one obtains:

$$\mathcal{F}(\boldsymbol{r}) = \frac{2}{T}\left[\sum_{i=0}^{m} w_i \varphi(\boldsymbol{r}+\boldsymbol{c}_i) - \varphi(\boldsymbol{r})\right], \tag{7.11}$$

$$\mathcal{G}(\boldsymbol{r}) = \frac{1}{T}\sum_{i=0}^{m} w_i \varphi(\boldsymbol{r}+\boldsymbol{c}_i). \tag{7.12}$$

Taylor expanding Eq.(7.11) and Eq(7.12) and using the constraints in Eq.(7.4) the discrete Laplacian and Gradient operators can be obtained as follows:

$$\nabla^2\varphi(\boldsymbol{r}) = \frac{2}{T}\left[\sum_{i=0}^{m} w_i \varphi(\boldsymbol{r}+\boldsymbol{c}_i) - \varphi(\boldsymbol{r})\right] + O(\nabla^4), \tag{7.13}$$

$$\nabla\varphi(\boldsymbol{r}) = \frac{1}{T}\sum_{i=0}^{m} w_i \varphi(\boldsymbol{r}+\boldsymbol{c}_i) + O(\nabla^3). \tag{7.14}$$

By construct these lattice operators are isotropic up to the leading order, with the error coefficient being $O(T)$ for any suitable choice of weights. Table 7.1 shows the weights(used in [10]) appearing in the lattice operators for a D2Q9 grid. The laplacian may be obtained through $\tilde{\Delta}^{\text{iso}} = \tilde{\boldsymbol{\nabla}}^{\text{iso}} \cdot \tilde{\boldsymbol{\nabla}}^{\text{iso}}$ and has the following leading order behaviour of the spectral error:

$$\tilde{\Delta}^{\text{iso}}(\boldsymbol{q}) = -q^2 + \frac{1}{3}q^4\delta x^2 + \mathcal{O}(\delta x^4), \tag{7.15}$$

with $\boldsymbol{q}$ is the wave vector with q being its magnitude. Here δx is the grid size for the cubic grid. Here, we would like to remind that the analytical laplacian, Δ, has a spectral representation $-q^2$. In the next section we introduce a more refined lattice model which drastically improves the isotropy and accuracy of the lattice operators.

7.2 BCC lattice operators

So far we have discussed lattice operators (7.1) described on an SC grid. Figure 7.2 shows a discrete representation of a circle in the simple cubic lattice(SC) and it is quite obvious that the simple cubic lattice has poor space discretization in representing the local curvature. As it is known that an octahedron has better discrete representation of curvatures than a square, one could use a BCC lattice for spatial grid distribution, and moreover the Wigner-Sietz cell for a BCC lattice is a truncated octahedron[85, 25].

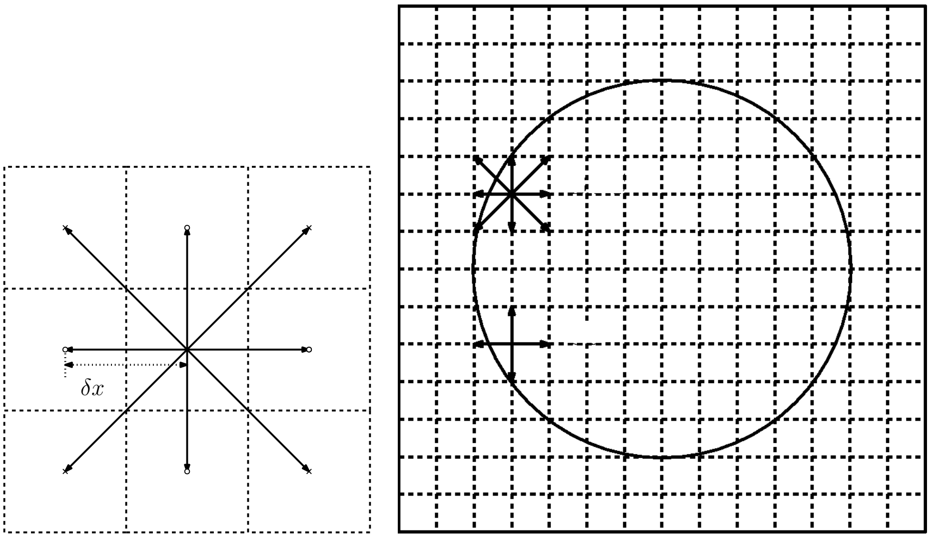

Fig. 7.2 Representation of a circle on an SC grid with and without the diagonal connectors.

Figure 7.3 shows much more accurate discrete representation of the same circle on a BCC grid, which is already introduced in lattice kinetic models[81], shows that the total number of boundary grid points is almost double as compared to that of the previous SC representation. This is expected as in a BCC lattice the neighbouring grid points (in the diagonal directions) are separated by a grid spacing of $\delta x/2$, instead of δx as in an SC grid. The off-grid points are approximated at the centre of the BCC grid in a staircase fashion, as often done in many finite difference and LBM formulations, and even in the staircase arrangement the accuracy for the BCC grid is quite high due to increased number of the surface points as compared to that of the SC.

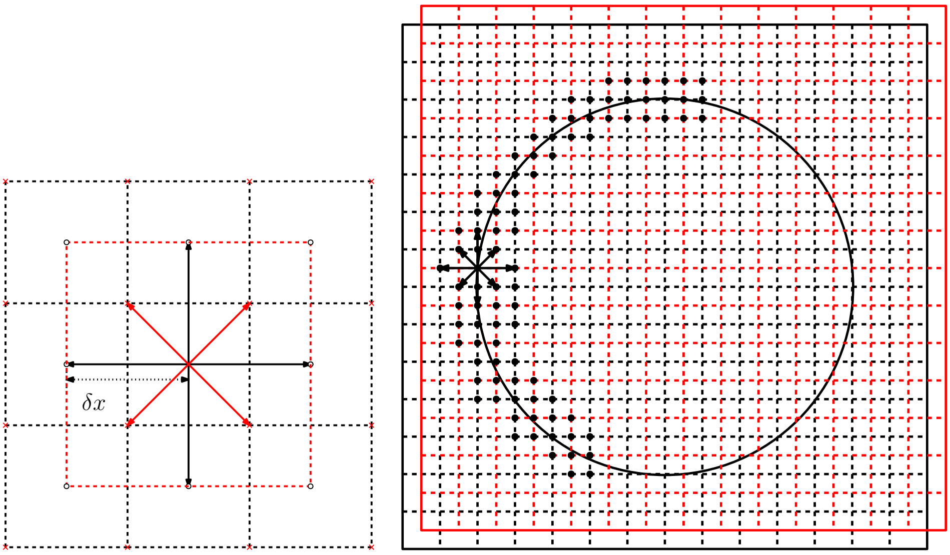

Fig. 7.3 Representation of a circle on a BCC grid

We generalize the aforementioned *DnQm* model on an BCC lattice, which will be called *RDnQm* onwards. The corresponding connecting vectors($\boldsymbol{c}_i$) change from $(\pm1, \pm1, \pm1)$ to $(\pm1/2, \pm1/2, \pm1/2)$

		RD2Q9		RD3Q27	
	N(2D projection)	$c_{i\alpha}=1/2$	$c_{i\alpha}=1$	$c_{i\alpha}=1/2$	$c_{i\alpha}=1$
0	1	0	0	0	0
NN	6(4)	0	1/24	0	1/24
NNN	12(4)	7/12	1/16	0	0
NNNN	8(0)	NA	NA	7/24	1/32

Table 7.2 Weights for RD2Q9 and RD3Q27 lattices on a BCC grid, with N being the number of neighbours, with $c_{i\alpha}$ being the connecting vector of the i-th link and in the direction α.

which lead to the new lattice constant $T = 1/5$. The lattice operators retain the same mathematical form as (7.1) along with the previously known constraints(7.4) and the weights are listed in table 7.2. In the low wave number limit the leading order error in the Fourier space of the Laplacian, defined on the BCC grid, is:

$$\tilde{\Delta}^{\text{iso}}(\boldsymbol{q}) = -q^2 + \frac{1}{24}q^4\delta x^2 + \mathcal{O}(\delta x^4). \tag{7.16}$$

It should be noted that the coefficient in the isotropic error for BCC-grid Laplacian(7.16) is eight time less than that of the SC lattice(7.15).

Here we show the following example of the time evolution of a scalar field on a BCC lattice-grid to show the effectiveness of the BCC operators.

7.2.1 Passive scalar advection

We consider any general scaler field(ϕ) which could be temperature or concentration, is being convected due to the presence of a background flow having velocity $\boldsymbol{u}$, in a periodic domain of length L. The initial condition for the scalar field is a Gaussian pulse. The governing equation for this can be written as follows:

$$\frac{\partial \phi(\boldsymbol{x},t)}{\partial t} + \boldsymbol{u}\cdot\boldsymbol{\nabla}\phi(\boldsymbol{x},t) = 0, \tag{7.17}$$

$$\text{Initial condition:} \quad \phi(\boldsymbol{x},0) = \frac{1}{\sqrt{2\pi}}e^{-\frac{\boldsymbol{x}^2}{2}}, \tag{7.18}$$

$$\text{Boundary condition:} \quad \phi(0,t) = \phi(L,t). \tag{7.19}$$

Here, (7.17) is numerically solved using a second order time accurate predictor-corrector method on a BCC grid, based on lattice operators, and which may be written as:

$$\phi^* = \phi^n - \delta t\boldsymbol{u}\cdot\tilde{\boldsymbol{\nabla}}^{\text{iso}}\phi^n, \tag{7.20}$$

$$\phi^{n+1} = \frac{1}{2}\left(\phi^n + \phi^* - \delta t\boldsymbol{u}\cdot\tilde{\boldsymbol{\nabla}}^{\text{iso}}\phi^*\right), \tag{7.21}$$

where ϕ^n represent the value of the scalar field at time instance n and δt is the time step. The results are benchmarked with the solution of the same obtained through a Mac-Cormack scheme on an SC grid. Figure 7.4 shows an instance of the evolution of the Gaussian pulse of the scalar field in time, and it is quite apparent that the scheme with BCC lattice operators preserves the structure of the Gaussian pulse during advection, whereas, the one for the Mac-Cormack, the pulse gets distorted over time. Figure 7.5 shows the projected contours of the pulse on the $X-Y$-plane, computed using grids with increasing resolutions viz. 50(a,d), 100(b,e) and 150(c,f), and it is observed that the accuracy of the results are

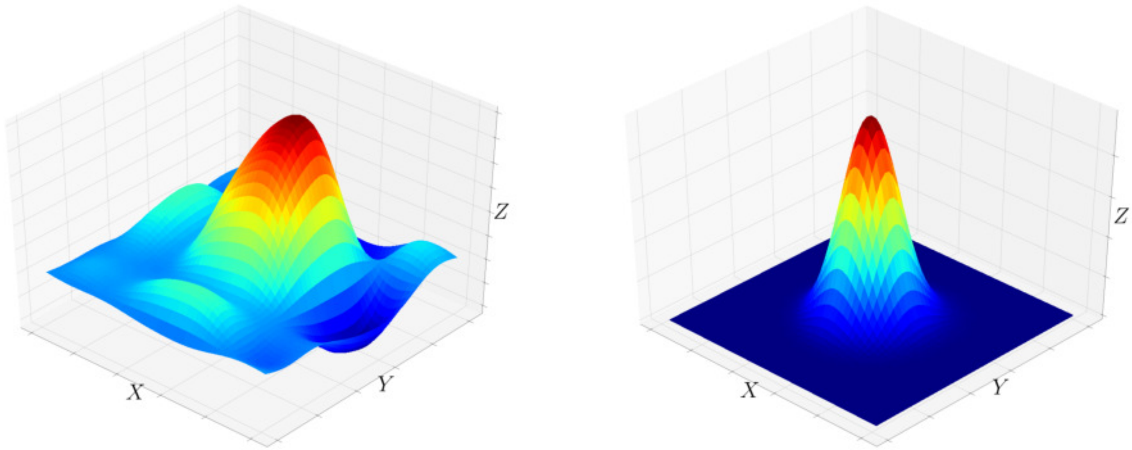

(a) (b)

Fig. 7.4 Instantaneous form of the Gaussian pulse at a 50 × 50 grid: Mac-Cormack(a) and BCC(b)

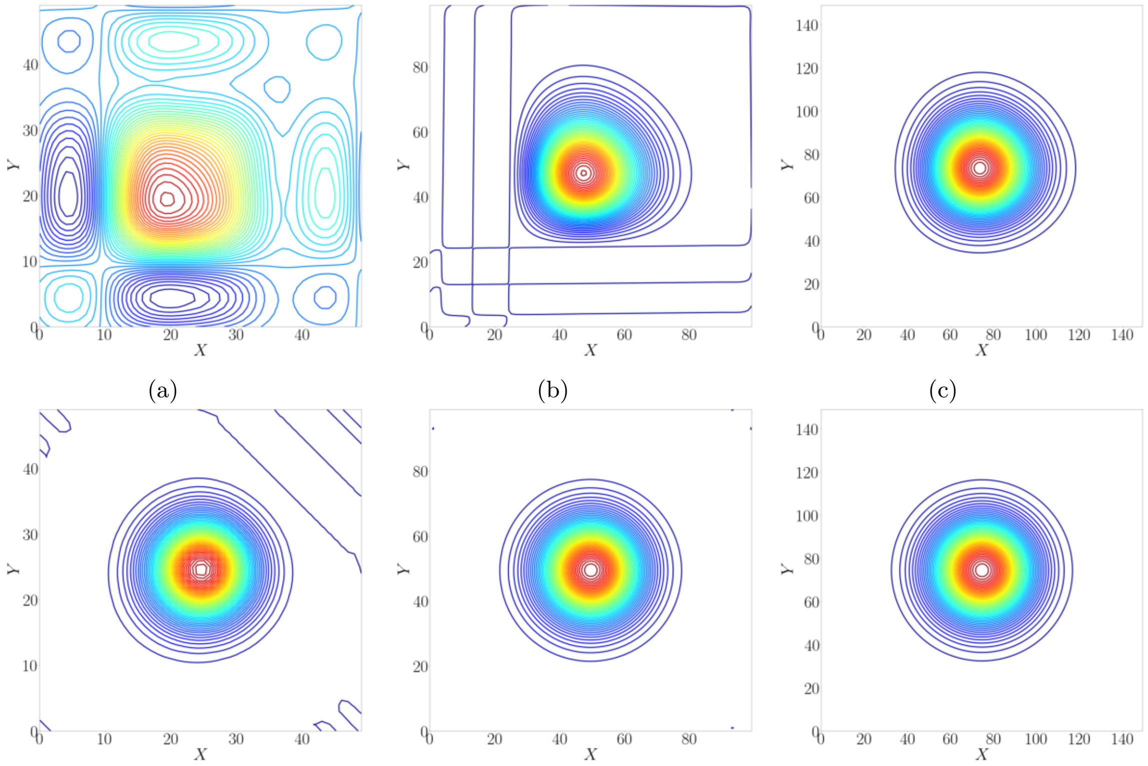

(a) (b) (c)

(d) (e) (f)

Fig. 7.5 Contour of the Gaussian pulse for different grid resolutions of 50(a,d), 100(b,e) and 150(c,f). The top panel shows results for Mac-Cormack and the bottom panel is for BCC

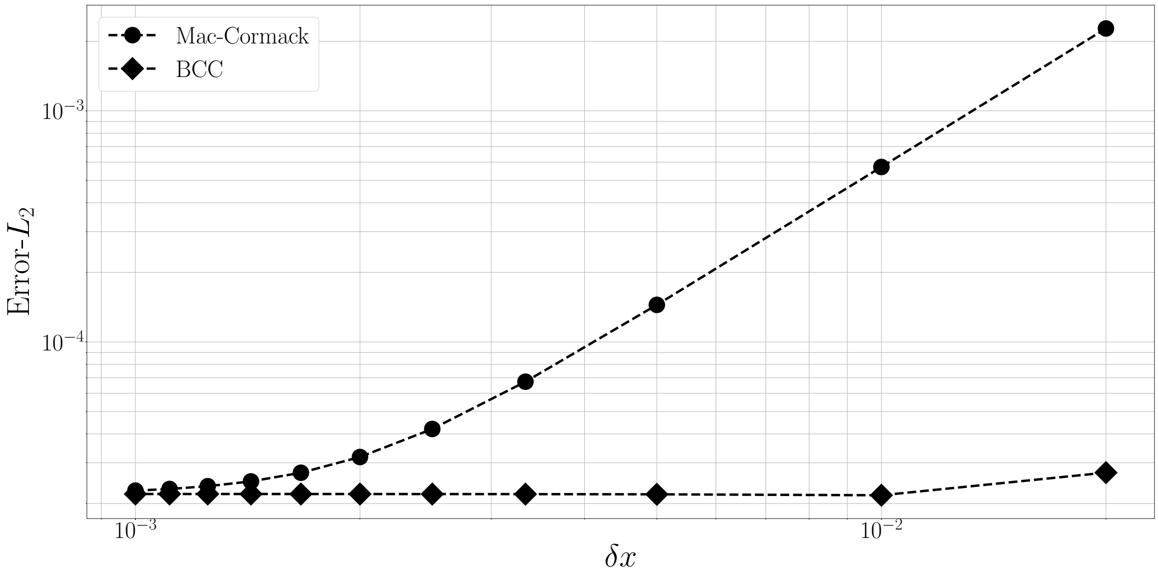

Fig. 7.6 L_2 norm of error between Mac-Cormack and BCC

much higher in the case of BCC operators than that of the Mac-Cormack and also the isotropy of the Gaussian pulse is preserved for the former, as the BCC lattice operators are isotropic. To quantify the difference in error between the Mac-Cormack and BCC shown in Figure 7.5, we present the L_2 norm of the error as function of the grid-resolution for BCC and Mac-Cormack in Figure 7.6, where it is readily evident that the superior accuracy and the isotropy of the BCC operators over Mac-Cormack lead to remarkably higher accuracy even at the lower resolution.

Chapter 8

Application of isotropic lattice operators

In this chapter we consider the following test cases, showing the time evolution of scalar or vector fields, where the computational domain is represented by an SC or a BCC lattice-grid and the isotropic lattice difference operators are used to compute the spatial discretization of the derivatives.

8.1 Isotropic operators on an SC lattice

First we consider the two-dimensional generalization of the stochastic diffusion problem discussed in the Chapter 6 where the preservation of the FDT at the discrrete level is discussed for a one dimensional stochastic diffusion equation. In this section we consider the two dimensional model B dynamics[23, 26] discretized on an SC lattice using the isotropic lattice differential operators and compared the obtained results to that of the CD2.

8.1.1 Model B: Harmonic fluctuations

For the sake of simplicity and without loss of generality, we first consider the following simplified case of model B, describing the dynamics of a non-interacting order parameter in single phase equilibrium,

$$\phi_i^{n+1} = \phi_i^n + \delta t\, D\, \tilde{\Delta}^{\mathrm{iso}} \phi_i^{n-1} + \sqrt{\delta t} \tilde{\nabla}^{\mathrm{iso}} \cdot \boldsymbol{\xi}, \tag{8.1}$$

with $D = A\,M$ being the diffusion coefficient. We contrast the present approach with the traditional discretization schemes, by performing a long time integration for this setup where the steady state probability distribution can be compared with the Gaussian distribution expected from the continuous model B dynamics. The superiority of the present work is apparent in the Fig.8.1, where the probability distribution of the order parameter $\phi(\boldsymbol{x}, t)$ is plotted. It should be noted that, with a considerably larger($\alpha = 0.22$) time step than that of the conventional CD2, current scheme shows much better agreement with the Gaussian. We also compare the spectra of the normalized energy distribution(equilibrium ratio) in Fig.8.2 for the CD2 and present scheme with the analytical one, from which the break down of FDT at discrete level for CD2 is quite apparent.

To highlight the quantitative improvements due to the present work, we present the polar plots of the normalized energy distribution(equilibrium ratio) at different wave numbers in Fig.8.3. We remind that for model B with non-interacting single well Landau-Ginzburg Hamiltonian of the order parameter, energy in any wave number is $0.5k_BT$ irrespective of the wave number, thus the normalized energy at any wave number should be one. As expected, result from current scheme is quite close to the analytical result, while central discretization shows violation of FDT even with the use of a time step which is four times smaller than that of the present scheme.

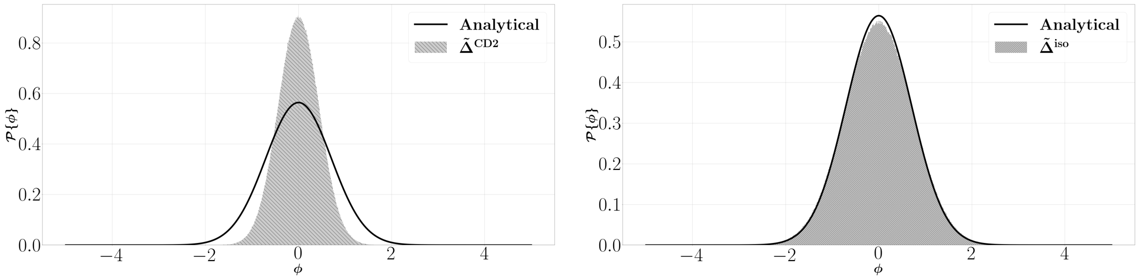

(a) CD2

(b) Isotropic

Fig. 8.1 Probability distribution of the order parameter filed for (a) CD2 ($\alpha = 0.05$) and (b) Isotropic schemes ($\alpha = 0.22$), computed by numerically integrating Eq.6.9 for a grid size of 128×128.

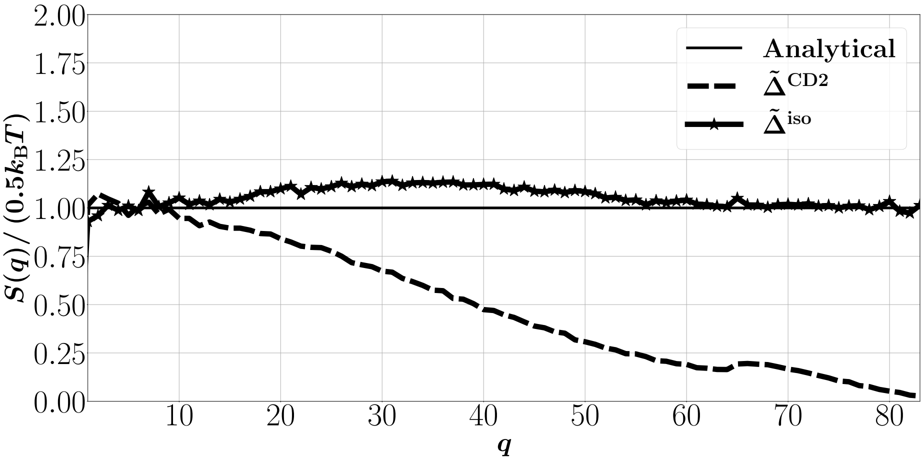

Fig. 8.2 Spectra of the equilibrium ratio ($S(\boldsymbol{q})/(0.5k_{\mathrm{B}}T))$) for CD2 ($\alpha = 0.05$) and Isotropic schemes ($\alpha = 0.22$), computed by numerically integrating Eq.6.9 for a grid size of 128×128.

8.1.2 Model B: Anharmonic fluctuations

In this section, we extend our treatment to the case of a inhomogeneous system, where different regions are coupled via free-energy gradients of the order parameter entering in the Landau-Ginzburg Hamiltonian $\mathcal{F}$. Using the isotropic operators and delayed discretization, the discrete model B assumes the following form, with $f(\phi_i^n)$ denoting the value of the respective discrete free energy density at lattice site i and time step n.

$$\phi_i^{n+1} = \phi_i^n + \delta t\, M\tilde{\Delta}^{\mathrm{iso}}\left[f(\phi_i^{n-1}) - K\tilde{\Delta}^{\mathrm{iso}}\phi_i^{n-1}\right] + \sqrt{\delta t}\tilde{\nabla}^{\mathrm{iso}} \cdot \boldsymbol{\xi}.$$

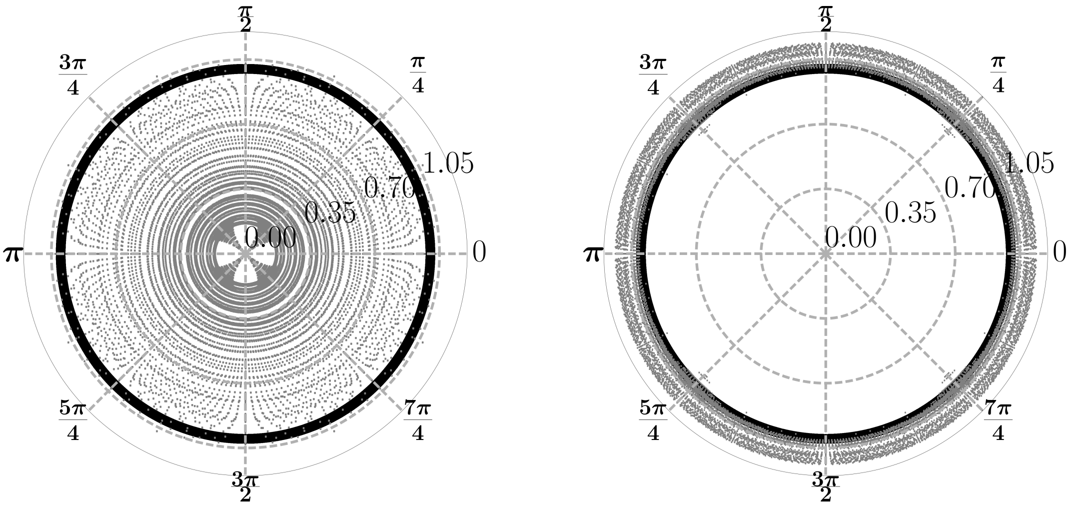

(a) CD2 (b) Isotropic

Fig. 8.3 Polar plot of the equilibrium ratio $(S(\boldsymbol{q})/(0.5k_\mathrm{B}T)))$ at different wave numbers. (a) $\tilde{\Delta}^{\mathrm{CD2}}$ with $\alpha = 0.05$, (b) $\tilde{\Delta}^{\mathrm{iso}}$ with $\alpha = 0.22$, Black circle: Analytical, computed by numerically integrating Eq.6.9 for a grid size of 128×128.

To establish the consistency of the present work over the usual central difference type operators, we compare the spectra of the structure factors obtained from three different discrete formulation of model B, viz. isotropic, central difference and Fourier pseudo spectral in Fig.8.4. Here free energy densities for both single phase $f(\phi) = \frac{1}{2}A\phi^2$ and two phase equilibrium $f(\phi) = \frac{1}{2}A\phi^2 + \frac{1}{4}B\phi^4$ are considered. The pseudo spectral, ensuring exact space derivatives, preserve the FDT at discrete level but the computation is much more expensive than the other two counterparts viz. CD2 and isotropic. On the other hand it is evident here that the failure of preserving FDT at the lattice level leads to an energy loss at the higher wave numbers for the case of CD2 as compared to that of the pseudo spectral result. The isotropic formulation does not show any such energy loss at the higher wave numbers, instead its energy spectra is very close to that of the pseudo spectral. To illustrate the quantitative aspect of the present formulation over the traditional schemes we also present the polar spectra in Fig.8.5 and Fig.8.6 for the structure factors of these three cases, which clearly bring out the anisotropy and breakdown of FDT at the discrete level for the traditional CD2 schemes as opposed to the isotropic discretization. It should be stressed here that in all these cases the isotropic scheme operates at a time step four times larger than that of the CD2 scheme.

To characterize the diffusive behaviour of the central difference scheme over the present formulation, we investigate the dynamics of the order parameter ϕ through its instantaneous distribution. In Fig.8.7 three consecutive instantaneous states of the order parameter evolution are compared for three different cases, namely CD2, isotropic and pseudo-spectral. It is evident from this plot Fig.8.7 that, for CD2, the system is in a little more quenched state than that of the isotropic or pseudo-spectral methods. This is indicative of the fact that the CD2 has more diffusive behaviour at higher wave numbers, which is also observed in Fig.8.4.

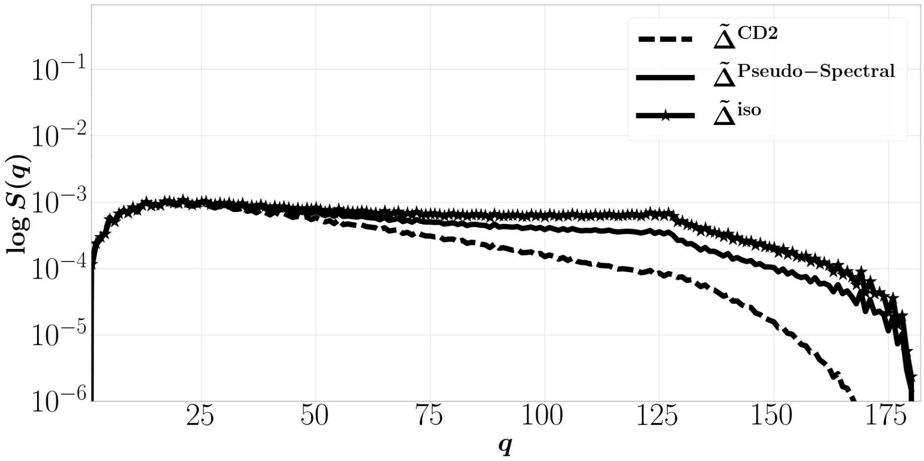

(a) Single well

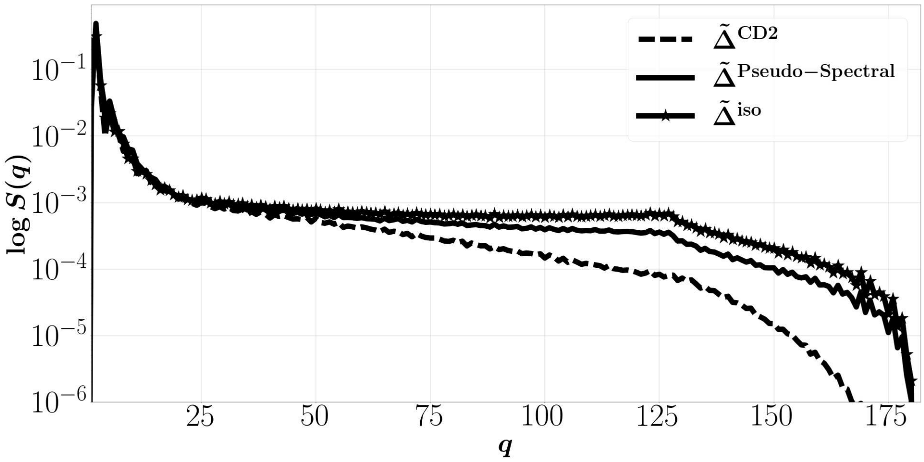

(b) Double well

Fig. 8.4 Time averaged spectra of the (a) single well and (b) double well structure factor $S(\boldsymbol{q})$ for, CD2($\alpha = 0.01$), Isotropic($\alpha = 0.04$) and Pseudo-Spectral($\alpha = 0.005$), computed by numerically integrating Eq.8.2 for a grid size of 256×256.

8.2 Isotropic operators on a BCC lattice

So far we have discussed the numerical solution of the model B dynamics using isotropic operators on an SC lattice. In this section we consider the Fluctuating Navier Stokes(FNS)[64] as the benchmark problem and discretized it on a BCC lattice using the BCC lattice operators.

8.2.1 Fluctuating hydrodynamics

There have been several attempts on the formulation of effective numerical schemes in simulating stochastic hydrodynamics over the years. [32, 36] used finite-volume based discretizations in the compressible isothermal fluctuating hydrodynamics and for the chemical master equation for reacting and diffusing species, respectively. [107] furnished both spectral and finite-volume formulations for the order parameter dynamics in model H. [33] formulated a finite-element discretization for the non-linear diffusion equation with thermal fluctuations. In recent years, [71–73, 70] introduced *peridynamic*

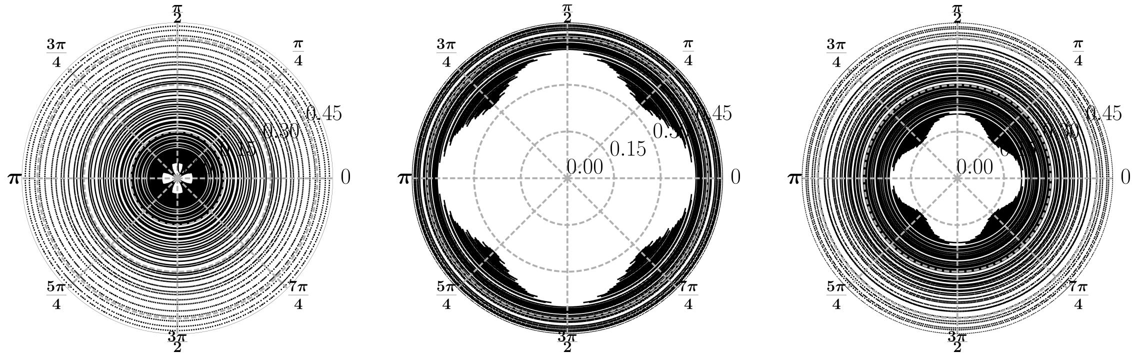

(a) CD2 (b) Isotropic (c) Pseudo-Spectral

Fig. 8.5 Polar plot of the single well structure factor $S(\boldsymbol{q})$ at different wave numbers. (a) $\tilde{\Delta}^{\mathrm{CD2}}(\alpha = 0.01)$, (b) $\tilde{\Delta}^{\mathrm{iso}}(\alpha = 0.04)$, (c) Pseudo-Spectral$(\alpha = 0.005)$, computed by numerically integrating Eq.8.2 for a grid size of 256×256.

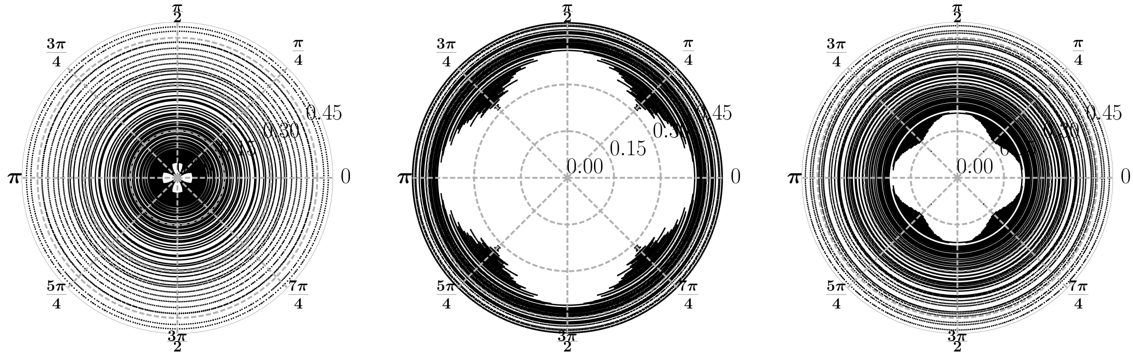

(a) CD2 (b) Isotropic (c) Pseudo-Spectral

Fig. 8.6 Polar plot of the double well structure factor $S(\boldsymbol{q})$ at different wave numbers. (a) $\tilde{\Delta}^{\mathrm{CD2}}(\alpha = 0.01)$, (b) $\tilde{\Delta}^{\mathrm{iso}}(\alpha = 0.04)$, (c) Pseudo-Spectral$(\alpha = 0.005)$, computed by numerically integrating Eq.8.2 for a grid size of 256×256.

differential operator for the numerical solution of complex field equations through allowing non-local form of local differentiation. The fluctuating hydrodynamics is described by the Fluctuating Navier-Stokes(FNS)[64] equations where the stochasticity originates in the thermal fluctuations which manifest through the stochastic stress and heat flux. The FNS are:

$$\partial_t \rho + \boldsymbol{\nabla} \cdot (\rho \boldsymbol{u}) = 0, \tag{8.2}$$

$$\partial_t (\rho \boldsymbol{u}) + \boldsymbol{\nabla} \cdot (\rho \boldsymbol{u} \boldsymbol{u}) = -\nabla p + \boldsymbol{\nabla} \cdot (\boldsymbol{\tau} + \tilde{\boldsymbol{\tau}}), \tag{8.3}$$

$$\partial_t (\rho E) + \boldsymbol{\nabla} \cdot (\rho E \boldsymbol{u}) = -\nabla p \cdot \boldsymbol{u} + \boldsymbol{\nabla} \cdot ((\boldsymbol{\tau} + \tilde{\boldsymbol{\tau}}) \cdot \boldsymbol{u}) + \boldsymbol{\nabla} \cdot (\boldsymbol{Q} + \tilde{\boldsymbol{Q}}), \tag{8.4}$$

where, ρ is the density of the fluid p is the thermodynamic pressure, $\boldsymbol{u}$ is the flow velocity and E is the total energy of the system. $\boldsymbol{\tau}$ and $\boldsymbol{Q}$ are the stress-tensor and the heat flux, respectively. The stochastic

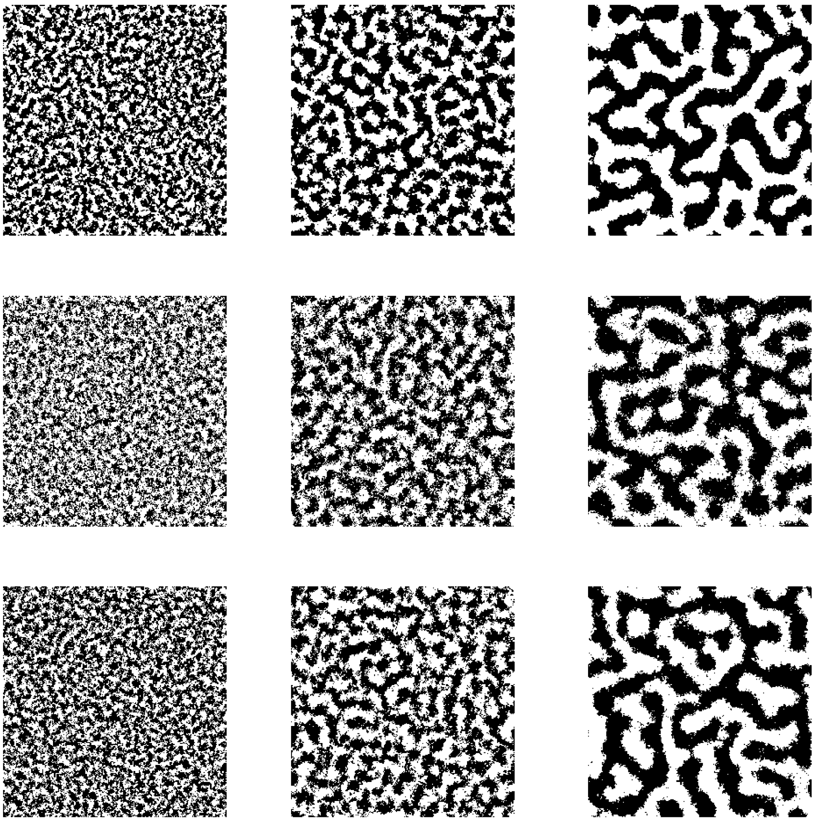

Fig. 8.7 Order parameter dynamics at three different instances for CD2(top panel), Isotropic and Pseudo-Spectral(bottom panel). Each panel shows three different instances, viz. $t = 10, 100, 1000$. Here, CD2 seems to be more quenched than the other two.

stress($\tilde{\boldsymbol{\tau}}$) and heat flux($\tilde{\boldsymbol{Q}}$) have Dirac-delta correlated Gaussian statistics in space and time:

$$\langle \tilde{\boldsymbol{\tau}}_{ij}(\boldsymbol{x},t)\tilde{\boldsymbol{\tau}}_{kl}(\boldsymbol{x}',t')\rangle = 2k_BT\mu\left(\delta_{ik}\delta_{jl} + \delta_{il}\delta_{jk} - \frac{2}{3}\delta_{ij}\delta_{kl}\right)\delta(t-t')\delta(\boldsymbol{x}-\boldsymbol{x}'), \tag{8.5}$$

$$\left\langle \tilde{\boldsymbol{Q}}(\boldsymbol{x},t)\tilde{\boldsymbol{Q}}(\boldsymbol{x}',t')\right\rangle = 2k_BT^2\kappa\,\boldsymbol{I}\,\delta(t-t')\delta(\boldsymbol{x}-\boldsymbol{x}'). \tag{8.6}$$

Here, μ, κ and T are the viscosity, thermal diffusivity and temperature of the fluid respectively, and k_B is the Boltzmann constant.

In the present context we have adopted the “kinetically reduced local Navier-Stokes"(KRLNS) formulation[5] of the (8.2), (8.3) and (8.4), where the evolution equation of energy(E)(8.4) is replaced by the evolution equation of the grand potential, $\mathcal{G}(= p - u^2/2)$ and thus the KRLNS with stochastic stress and heat flux may be written as :

$$\partial_t \rho + \boldsymbol{\nabla} \cdot (\rho \boldsymbol{u}) = 0, \tag{8.7}$$

$$\partial_t(\rho \boldsymbol{u}) + \boldsymbol{\nabla} \cdot (\rho \boldsymbol{u}\boldsymbol{u}) = -\boldsymbol{\nabla}\left(\mathcal{G} + \frac{u^2}{2}\right) + \boldsymbol{\nabla} \cdot (\boldsymbol{\tau} + \tilde{\boldsymbol{\tau}}), \tag{8.8}$$

$$\partial_t \mathcal{G} = -\rho \left.\frac{\partial p}{\partial \rho}\right|_S \boldsymbol{\nabla} \cdot \boldsymbol{u} + \frac{1}{2}(\boldsymbol{\nabla} \cdot \boldsymbol{u})u^2 - \boldsymbol{\nabla} \cdot ((\boldsymbol{\tau} + \tilde{\boldsymbol{\tau}}) \cdot \boldsymbol{u}) \tag{8.9}$$

$$+ \frac{1}{\rho C_v} \left.\frac{\partial p}{\partial T}\right|_\rho (\boldsymbol{\nabla} \boldsymbol{u} : (\boldsymbol{\tau} + \tilde{\boldsymbol{\tau}} + \boldsymbol{\nabla} \cdot (\boldsymbol{Q} + \tilde{\boldsymbol{Q}})),$$

where C_v is the specific heat at constant volume and S denotes entropy. It is readily evident that (8.10) is local as compared to (8.4) due to the absence of any convective term of $\mathcal{G}$. In the low Mach number regime($Ma \ll 1$), which is required at the incompressible limit[18], the KRLNS equations along with the stochastic stress and heat flux may be written in the following non-dimensional form:

$$\partial_t u_i + \partial_j u_i u_j = -\partial_i p + \frac{1}{Re} \partial_j \partial_j u_i + \partial_j \tilde{\tau}_{ij}, \tag{8.10}$$

$$\partial_t \mathcal{G} = -\frac{1}{Ma^2} \partial_i u_i + \frac{1}{Re} \partial_i \partial_i \mathcal{G} + \partial_j \tilde{Q}_j, \tag{8.11}$$

where Ma=u/c and Re=$\rho u L/\mu$ are the Mach and Reynolds number of the flow, respectively, with c and L being the speed of sound and the characteristic length scale, respectively.

As discussed in section 7.2.1 we again apply the predictor-corrector based algorithm equipped with BCC operators on the stochastic KRLNS equations((8.10) and (8.11)) in two fluctuating hydrodynamic problems, namely, the stochastic channel flow and the stochastic lead driven cavity(stochastic LDC) and analyze the instantaneous and time-averaged behaviour of the flow field.

Stochastic channel flow

We first consider a rectangular channel having no-slip walls at the top and at the bottom, i.e. $\boldsymbol{u}(x, 0, t) = \boldsymbol{u}(x, L_y, t) = 0$ and a Neumann boundary condition on pressure, $\partial_y p(x, y, t)|_{y=0,L_y} = 0$, is imposed; periodic boundary conditions are imposed at the left and right ends of of the channel, i.e. $(\boldsymbol{u}, p)(0, y, t) = (\boldsymbol{u}, p)(L_x, y, t)$, where L_x and L_y are the length and width of the channel, respectively. An axial force term, mimicking a favourable axial pressure gradient, is considered in the flow field to maintain the flow. Figure 8.8 shows the implementation of calculation of the flux near a boundary, where we show that the computation of the gradient operator near the wall(shown by the thick solid line with hash lines above it) at the grid point (i, j) would require the value of the field(ϕ) at the off-grid point $(i, j + 1)$ while using a BCC scheme, which is approximated as the average of the values of the field at points $(i - 1/2, j + 1/2)$ and $(i + 1/2, j + 1/2)$ as:

$$\phi_{i,j+1} = \frac{1}{2}\left(\phi_{i-1/2,j+1/2} + \phi_{i+1/2,j+1/2}\right) \tag{8.12}$$

Figure 8.9a shows the comparison between the instantaneous axial velocity field obtained through BCC finite difference and theory for Re = 1 and Ma = 0.01. Next we consider the same channel but having slip boundary conditions at the wall, having the form $u_x|_{y=0,L_y} = \mathrm{Kn}\,\mathcal{C}\,\partial u_x/\partial y|_{y=0,L_y}$ and $u_y(x, 0, t) = u_y(x, L_y, t) = 0$, where Kn is the Knudsen number and the pre-factor $\mathcal{C}$=0.8297[113]. The

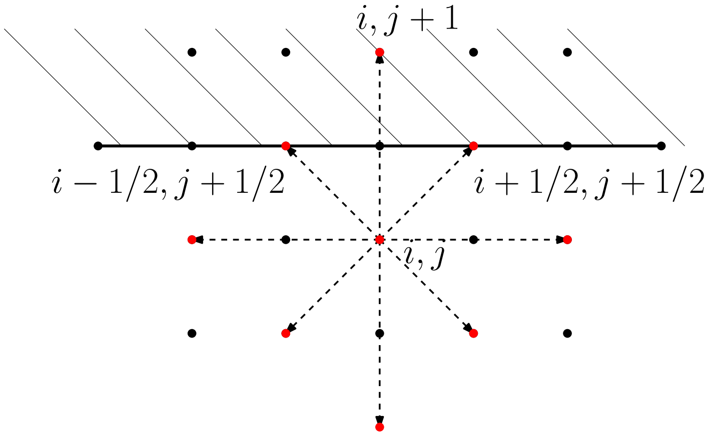

Fig. 8.8 Implementation of the flux boundary in BCC

results are shown in the Figure 8.9b, benchmarked with the results obtained from a Direct Simulation Monte Carlo (DSMC) computation and theory. It is observed in all these plots that the velocity profile is parabolic and bears excellent agreement with both theoretical result and DSMC.

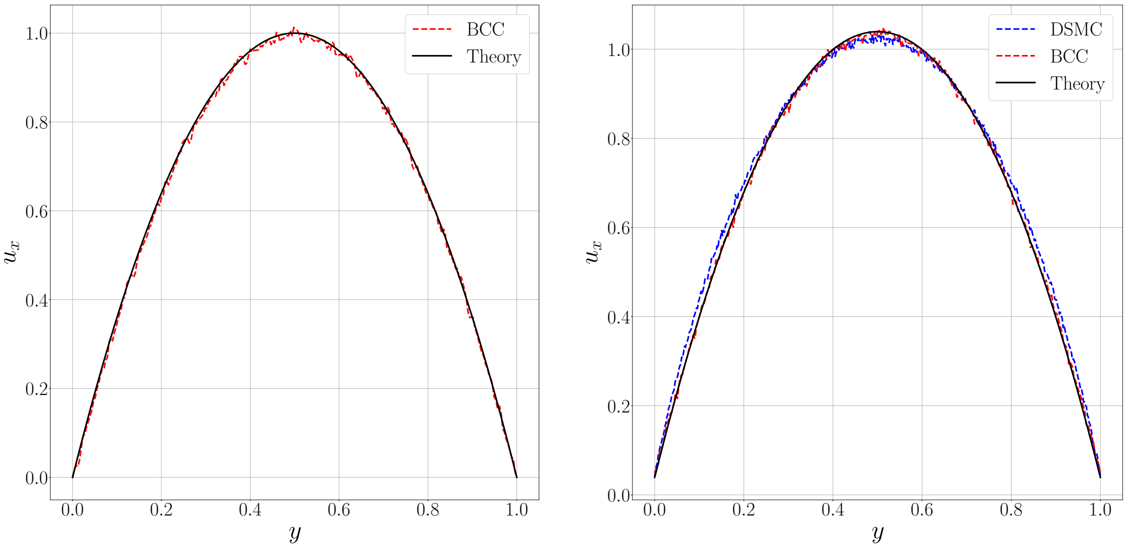

(a) (b)

Fig. 8.9 Instantaneous axial velocity profile for the stochastic flow in a channel for Re = 1 and Ma = 0.01 having (a) no-slip and (b) slip walls on a 512 × 512 grid. I thank **Mr. Akshay Chandran** (EMU, JNCASR) for providing the results of the DSMC computation.

Stochastic lid driven cavity

We consider flow in a 2D-cavity having fixed left, right and the bottom walls and the top wall is moving with a velocity in the x-direction($u_x = 1$), and no slip boundary conditions are considered at all the walls i.e. $u_x(x, L, t) = 1$, $u_y(x, L, t) = 0$ and $\boldsymbol{u}(x, 0, t) = \boldsymbol{u}(0, y, t) = \boldsymbol{u}(L, y, t) = 0$. Neumann boundary conditions on pressure, $\partial_x p(x, y, t)|_{x=0,L} = \partial_y p(x, y, t)|_{y=0,L} = 0$, are imposed on all four walls, with L

being the dimension of the cavity. Figure 8.10 shows the instantaneous and averaged velocity distribution in the cavity at Re $= 5000$ and Ma $= 0.1$, and it is observed that the averaged velocity profiles depicts good agreements with the same for the non-fluctuating 2D-LDC problem[42]. Figure 8.11 shows the centre-line distribution of the instantaneous and averaged velocities in x and y directions and it is again observed that the averaged profiles bear good agreement with that of the standard 2D-LDC simulation of [42, 19, 50, 95]. Figure 8.12 and 8.13 show the instantaneous and time averaged vorticity distributions in the domain for flow with Kn $= 0.1$(Re $= 1$ and Ma $= 0.1$) and Kn $= 1$(Re $= 0.1$ and Ma $= 0.1$), respectively where Kn $=$ Ma/Re is the Knudsen number. Here the appearance of the corner vortices at the top right and left corners is evident. In Figure 8.14 we also present the centerline averaged velocity distribution in the x and y directions for Kn $= 0.1$ and Kn $= 1$.

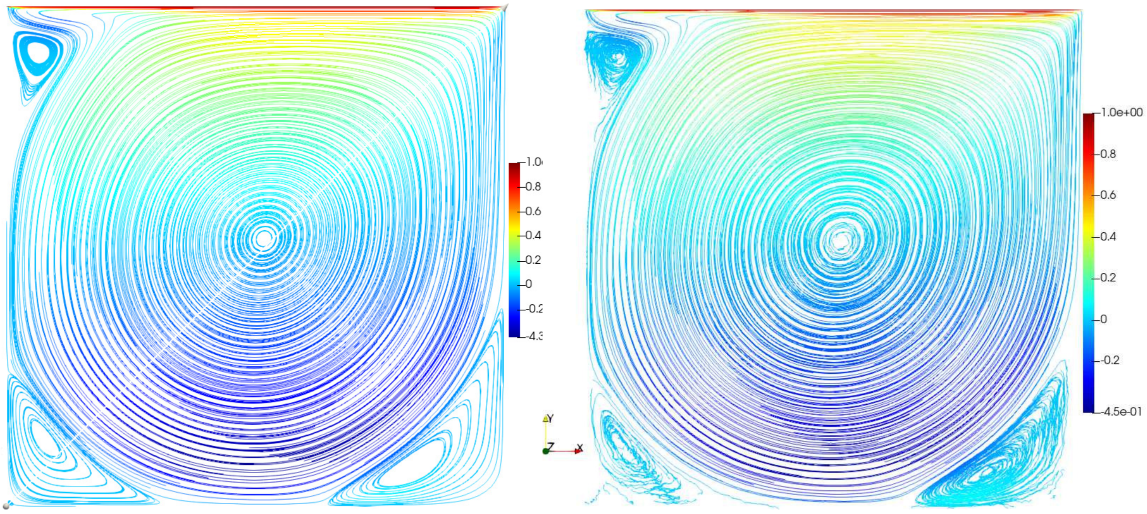

(a) Time averaged (b) Instantaneous

Fig. 8.10 Streamlines of the (a) time averaged and (b) instantaneous velocity fields for the lid driven cavity at Re $= 5000$ and Ma $= 0.1$ using BCC for 512×512 grid.

Flow past a circular cylinder

Here we present some of the preliminary results showing the flow past a circular cylinder lying inside a rectangular region having length $16D$ and width $8D$, with D being the diameter of the cylinder, and the co-ordinates of the center of the cylinder is at $(4D, 4D)$. The left boundary of the region is an inlet$(u_x(0, y, t) = 1, u_y(0, y, t) = 0)$, the top and bottom are no slip walls$(\boldsymbol{u}(x, 0, t) = \boldsymbol{u}(x, 8D, t) = 0)$, and the right side has outflow boundary$(\partial_x u_x(16D, y, t) = \partial_x u_y(16D, y, t) = 0)$ conditions. Neumann boundary conditions on pressure, $\partial_x p(x, y, t)|_{x=0,16D} = \partial_y p(x, y, t)|_{y=0,8D} = 0$, are imposed on all four sides of the domain. Figure 8.15,8.16 and 8.17 shows the streamlines of the velocity field and the vorticity contours for three different Re viz. Re =20,100 and 500, respectively. One may observe the periodic shedding of the trailing vortices for higher Re(=100), and for Re=500 the von-Karman vortex street is evident.

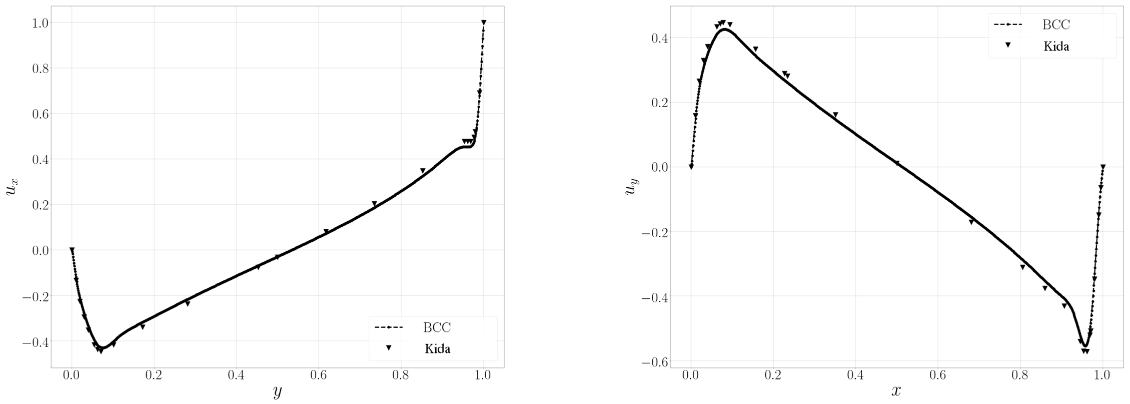

(a) Averaged u_x (b) Averaged u_y

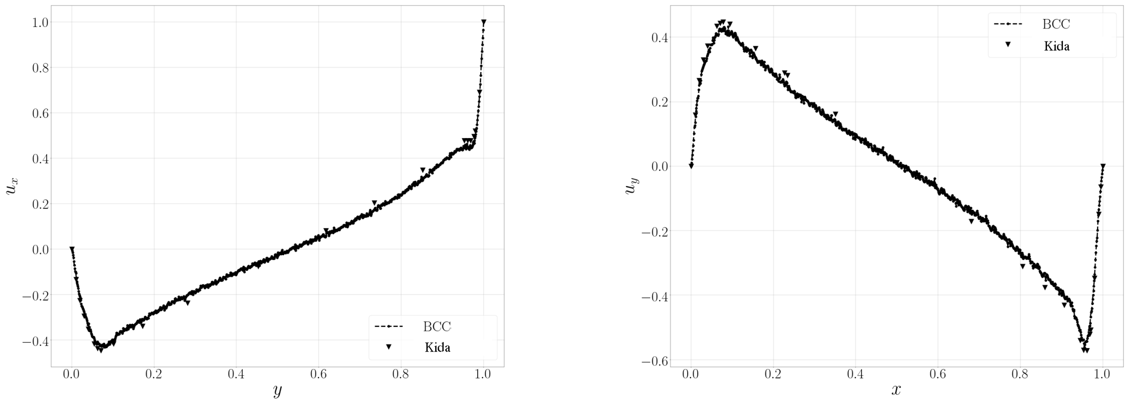

(c) Instantaneous u_x (d) Instantaneous u_y

Fig. 8.11 The centreline distribution of the averaged and instantaneous $u_x(x = 0.5)$(a,c) and $u_y(y = 0.5)$(b,d) for lid driven cavity at Re = 5000 and Ma = 0.1 using BCC for 512 × 512 grid.

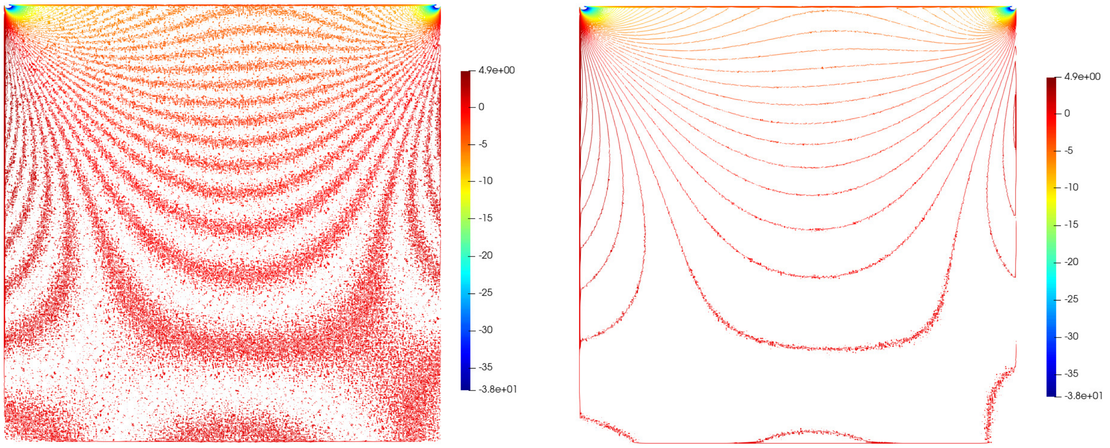

(a) Instantaneous vorticity field (b) Time averaged vorticity field

Fig. 8.12 The instantaneous(a) and averaged(b) vorticity fields for lid driven cavity at Kn = 0.1 using BCC for 512 × 512 grid.

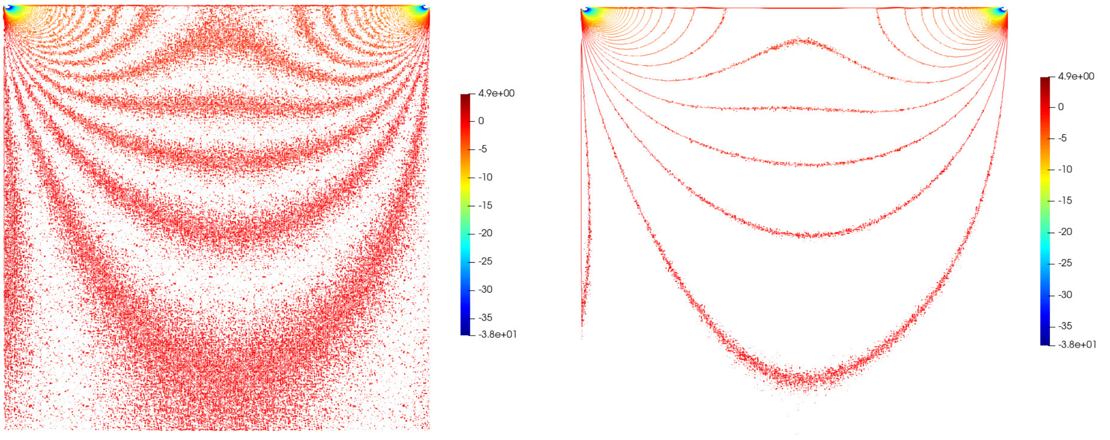

(a) Instantaneous vorticity field

(b) Time averaged vorticity field

Fig. 8.13 The instantaneous(a) and averaged(b) vorticity fields for lid driven cavity at Kn = 1.0 using BCC for 512 × 512 grid.

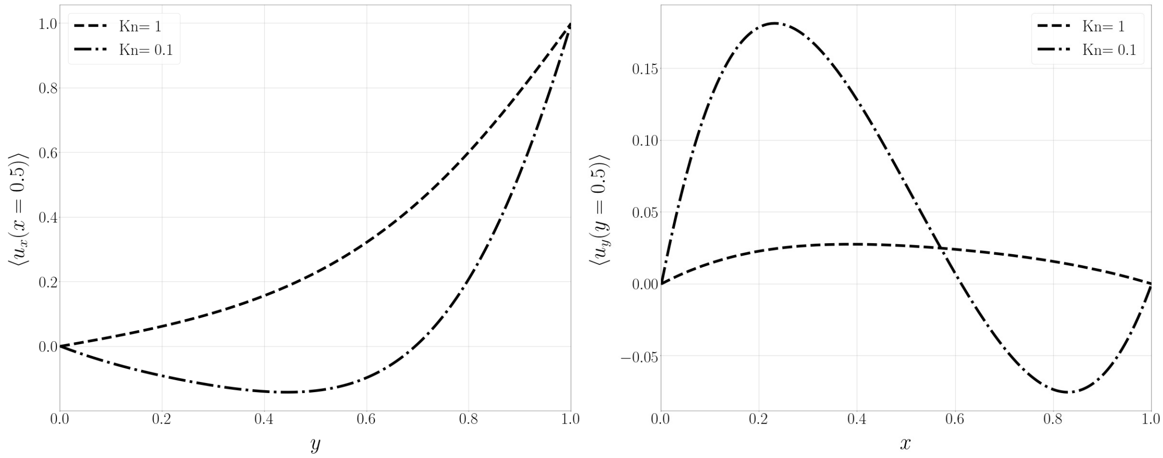

(a)

(b)

Fig. 8.14 The centreline distribution of the time averaged velocity components $u_x(x = 0.5)$(a) and $u_y(y = 0.5)$(b) for lid driven cavity at Kn = 0.1 and Kn = 1.0 using BCC for 512 × 512 grid.

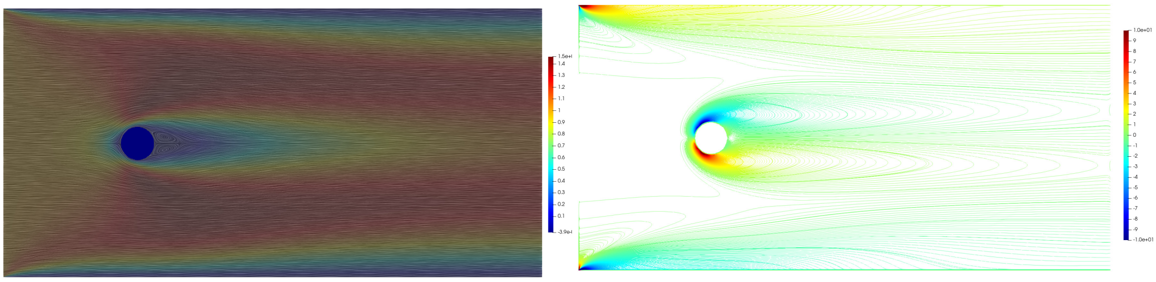

(a) Streamlines of the velocity field (b) Vorticity field

Fig. 8.15 The steady state (a) streamlines and (b) vorticity fields for flow past a circular cylinder at Re = 20 using BCC for 1024 × 512 grid.

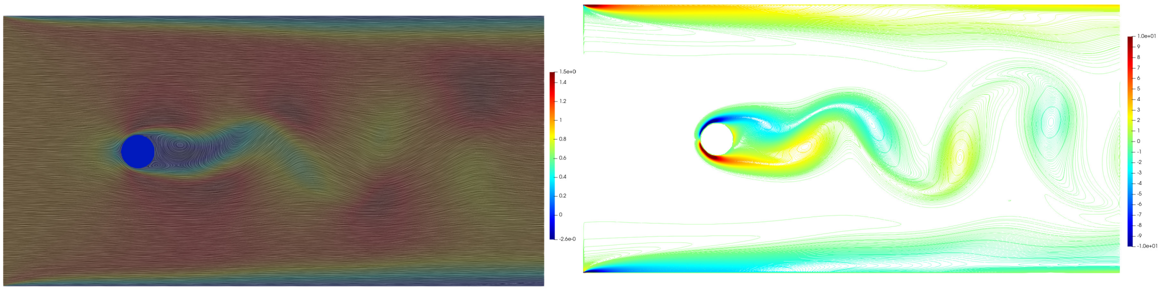

(a) Instantaneous streamlines of the velocity field (b) Instantaneous vorticity field

Fig. 8.16 The (a) streamlines and (b) vorticity fields for flow past a circular cylinder at Re = 100 using BCC for 1024 × 512 grid.

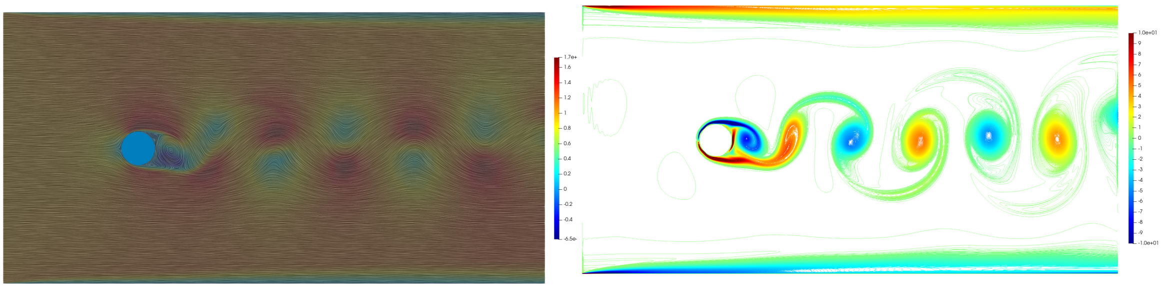

(a) Instantaneous streamlines of the velocity field (b) Instantaneous vorticity field

Fig. 8.17 The (a) streamlines and (b) vorticity fields for flow past a circular cylinder at Re = 500 using BCC for 1024 × 512 grid.

Chapter 9

Outlook

We have presented a discrete framework where the essence of phase separation dynamics in terms of fluctuation-dissipation relation is preserved. Thus, similar to the cell dynamical method, a fully self-consistent framework at discrete level is obtained. The present approach also allows the discrete framework to inherit transport properties and free energies known from PDE based formulation. It should also be pointed out that, the present formulation can easily be extended to three dimensions(3D), as all of these aforementioned isotropic operators can also be derived in 3D. For a detailed formulation of these operators in higher dimensions one might refer to [107, 90].

Also in order to contrast these isotropic difference operators with cell dynamics, we write Eq.8.1 in a form analogous to Eq.(2.7,2.8) of [84] as:

$$\phi_i^{n+1} = \phi_i^n + D\,\delta t\left[\langle\langle\phi_i^{n-1}\rangle\rangle - \phi_i^{n-1}\right] + \sqrt{dt}\tilde{\nabla}^{\text{iso}}\cdot\boldsymbol{\xi}, \tag{9.1}$$

where,

$$\tilde{\nabla}^{\text{iso}}\phi(\boldsymbol{x},t) = \frac{1}{3\delta x}\sum_{i=1}^{N_i}\phi_i + \frac{1}{12\delta x}\sum_{j=1}^{N_j}\phi_j, \tag{9.2}$$

$$\langle\langle\phi(\boldsymbol{x},t)\rangle\rangle = -\frac{1}{9}\sum_{i=1}^{N_i}\phi_i + \frac{1}{9}\sum_{j=1}^{N_j}\phi_j + \frac{1}{18}\sum_{k=1}^{N_k}\phi_k + \frac{1}{72}\sum_{l=1}^{N_l}\phi_l + \frac{1}{2}\phi(\boldsymbol{x},t). \tag{9.3}$$

Here, N_i, N_j, N_k, N_l are the nearest and next nearest neighbours and so on. It can be observed that the discrete form of the model B in Eq.9.1 and the discrete operators Eq.9.2 and Eq.9.3 preserve the same structure of a Cell Dynamical System(CDS)[84]. Though the form is similar, two key differences, wider stencil and use of past data are must be noted. These two differences allow us to formulate a cell dynamical system where FDT is preserved even at the discrete level and the connection with the PDE is also apparent.

We have also shown that the formalism of lattice differential operators can be extended to a BCC grid without the loss of any key properties such as isotropy. It is observed that in lattice kinetic models, the BCC grid enables one to represent solid or interfacial irregular boundaries with better accuracy as compared to an SC grid. Therefore, this property improves the overall accuracy of the BCC lattice differential operators to a great extent. The BCC lattice operators have been implemented to discretize the advection equation and also the fluctuating Navier-Stokes, and the results show good agreement with the standard literature.

References

[1] Acrivos, A. (1971). Heat transfer at high péclet number from a small sphere freely rotating in a simple shear field. *Journal of Fluid Mechanics*, 46(2):233–240.

[2] Acrivos, A. and Goddard, J. D. (1965). Asymptotic expansions for laminar forced-convection heat and mass transfer. *Journal of Fluid Mechanics*, 23(2):273–291.

[3] Amini, H., Lee, W., and Di Carlo, D. (2014). Inertial microfluidic physics. *Lab Chip*, 14:2739–2761.

[4] Angilella, J.-R., Vilela, R. D., and Motter, A. E. (2014). Inertial particle trapping in an open vortical flow. *Journal of Fluid Mechanics*, 744:183–216.

[5] Ansumali, S., Karlin, I. V., and Öttinger, H. C. (2005). Thermodynamic theory of incompressible hydrodynamics. *Phys. Rev. Lett.*, 94:080602.

[6] Aref, H. (1983). Integrable, chaotic, and turbulent vortex motion in two-dimensional flows. *Annual Review of Fluid Mechanics*, 15:345–389.

[7] Aref, H. and Pomphrey, N. (1980). Integrable and chaotic motions of four vortices. *Physics Letters A*, 78:297 – 300.

[8] Aref, H. and Pomphrey, N. (1982). Integrable and chaotic motions of four vortices. i. the case of identical vortices. *Proceedings of the Royal Society of London A: Mathematical, Physical and Engineering Sciences*, 380:359–387.

[9] Aref, H. and Stremler, M. A. (1999). Four-vortex motion with zero total circulation and impulse. *Physics of Fluids*, 11:3704–3715.

[10] Banerjee, M. R., Succi, S., Ansumali, S., and Adhikari, R. (2017). Isotropic finite-difference discretization of stochastic conservation laws preserving detailed balance. *Journal of Statistical Mechanics: Theory and Experiment*, 2017(10):103202.

[11] Batchelor, G. K. (1970). Slender-body theory for particles of arbitrary cross-section in stokes flow. *Journal of Fluid Mechanics*, 44(3):419–440.

[12] Batchelor, G. K. (1977). The effect of brownian motion on the bulk stress in a suspension of spherical particles. *J. Fluid Mech.*, 83(01):97–117.

[13] Batchelor, G. K. and Green, J. T. (1972a). The determination of the bulk stress in a suspension of spherical particles to order c2. *Journal of Fluid Mechanics*, 56:401–427.

[14] Batchelor, G. K. and Green, J. T. (1972b). The hydrodynamic interaction of two small freely-moving spheres in a linear flow field. *Journal of Fluid Mechanics*, 56(2):375–400.

[15] Bleher, S., Grebogi, C., and Ott, E. (1990). Bifurcation to chaotic scattering. *Physica D: Nonlinear Phenomena*, 46:87 – 121.

[16] Bleher, S., Ott, E., and Grebogi, C. (1989). Routes to chaotic scattering. *Phys. Rev. Lett.*, 63:919–922.

[17] Bochev, P. B. and Hyman, J. M. (2006). Principles of mimetic discretizations of differential operators. pages 89–119. Springer New York.

[18] Borok, S., Ansumali, S., and Karlin, I. V. (2007). Kinetically reduced local navier-stokes equations for simulation of incompressible viscous flows. *Phys. Rev. E*, 76:066704.

[19] Botella, O. and Peyret, R. (1998). Benchmark spectral results on the lid-driven cavity flow. *Computers & Fluids*, 27(4):421 – 433.

[20] Brenner, H. (1964a). The stokes resistance of an arbitrary particle—iii: Shear fields. *Chemical Engineering Science*, 19(9):631 – 651.

[21] Brenner, H. (1964b). The stokes resistance of an arbitrary particle—iv arbitrary fields of flow. *Chemical Engineering Science*, 19(10):703 – 727.

[22] Brenner, H. (1966). The stokes resistance of an arbitrary particle—part v.: Symbolic operator representation of intrinsic resistance. *Chemical Engineering Science*, 21(1):97 – 109.

[23] Cahn, J. W. and Hilliard, J. E. (1971). Spinodal decomposition: A reprise. *Acta Metall.*, 19(2):151–161.

[24] Chaudhri, A., Bell, J. B., Garcia, A. L., and Donev, A. (2014). Modeling multiphase flow using fluctuating hydrodynamics. *Phys. Rev. E*, 90(3):033014.

[25] Conway, J. H. and Sloane, N. J. A. (2013). *Sphere packings, lattices and groups*, volume 290. Springer Science & Business Media.

[26] Cook, H. E. (1970). Brownian motion in spinodal decomposition. *Acta Metall.*, 18(3):297–306.

[27] Cox, R., Zia, I., and Mason, S. (1968). Particle motions in sheared suspensions xxv. streamlines around cylinders and spheres. *Journal of Colloid and Interface Science*, 27(1):7 – 18.

[28] Cross, M. C. and Hohenberg, P. C. (1993). Pattern formation outside of equilibrium. *Rev. Mod. Phys.*, 65(3):851.

[29] Dabade, V., Marath, N. K., and Subramanian, G. (2015). Effects of inertia and viscoelasticity on sedimenting anisotropic particles. *Journal of Fluid Mechanics*, 778:133–188.

[30] Dabade, V., Marath, N. K., and Subramanian, G. (2016). The effect of inertia on the orientation dynamics of anisotropic particles in simple shear flow. *Journal of Fluid Mechanics*, 791:631–703.

[31] Davidovitch, B., Moro, E., and Stone, H. A. (2005). Spreading of viscous fluid drops on a solid substrate assisted by thermal fluctuations. *Phys. Rev. Lett.*, 95(24):244505.

[32] De Fabritiis, G., Serrano, M., Delgado-Buscalioni, R., and Coveney, P. V. (2007). Fluctuating hydrodynamic modeling of fluids at the nanoscale. *Phys. Rev. E*, 75:026307.

[33] de la Torre, J. A., Espanol, P., and Donev, A. (2015). Finite element discretization of non-linear diffusion equations with thermal fluctuations. *The Journal of Chemical Phy sics*, 142(9).

[34] Debye, P. (1959). Angular dissymmetry of the critical opalescence in liquid mixtures. *J. Chem. Phys.*, 31(3):680–687.

[35] Debye, P., Chu, B., and Kaufmann, H. (1962). Critical opalescence of binary liquid mixtures: Methanol—cyclohexane; aniline—cyclohexane. *J. Chem. Phys.*, 36(12):3378–3381.

[36] Donev, A., Vanden Eijnden, E., Garcia, A. L., and Bell, J. B. (2010). On the accuracy of explicit finite-volume schemes for fluctuating hydrodynamics. *Communications in Applied Mathematics and Computational Science*, 5(2):149–197.

[37] Eckhardt, B. (1988). Irregular scattering of vortex pairs. *EPL (Europhysics Letters)*, 5:107.

[38] Eckhardt, B. and Aref, H. (1988). Integrable and chaotic motions of four vortices ii. collision dynamics of vortex pairs. *Philosophical Transactions of the Royal Society of London A: Mathematical, Physical and Engineering Sciences*, 326:655–696.

[39] Eckhardt, B., Schneider, T. M., Hof, B., and Westerweel, J. (2007). Turbulence transition in pipe flow. *Annual Review of Fluid Mechanics*, 39:447–468.

[40] Evans, R. (1981). The role of capillary wave fluctuations in determining the liquid-vapour interface: Analysis of the van der waals model. *Mol. Phys.*, 42(5):1169–1196.

[41] Faisst, H. and Eckhardt, B. (2004). Sensitive dependence on initial conditions in transition to turbulence in pipe flow. *Journal of Fluid Mechanics*, 504:343–352.

[42] Ghia, U., Ghia, K., and Shin, C. (1982). High-re solutions for incompressible flow using the navier-stokes equations and a multigrid method. *Journal of Computational Physics*, 48(3):387 – 411.

[43] Gottdiener, L. (1975). The multiple-collision region in non-reactive atom-diatom collisions. *Molecular Physics*, 29(5):1585–1595.

[44] Gouillart, E., Dauchot, O., Thiffeault, J.-L., and Roux, S. (2009). Open-flow mixing: Experimental evidence for strange eigenmodes. *Physics of Fluids*, 21(2):023603.

[45] Harlen, O. G. and Koch, D. L. (1993). Simple shear flow of a suspension of fibres in a dilute polymer solution at high deborah number. *Journal of Fluid Mechanics*, 252:187–207.

[46] Helfand, E. and Fredrickson, G. H. (1989). Large fluctuations in polymer solutions under shear. *Phys. Rev. Lett.*, 62(21):2468.

[47] Ho, B. P. and Leal, L. G. (1974). Inertial migration of rigid spheres in two-dimensional unidirectional flows. *Journal of Fluid Mechanics*, 65(2):365–400.

[48] Ho, B. P. and Leal, L. G. (1976). Migration of rigid spheres in a two-dimensional unidirectional shear flow of a second-order fluid. *Journal of Fluid Mechanics*, 76(4):783–799.

[49] Hohenberg, P. C. and Halperin, B. I. (1977). Theory of dynamic critical phenomena. *Rev. Mod. Phys.*, 49:435–479.

[50] Hyman, J. M. and Shashkov, M. (1999). Mimetic discretizations for maxwell's equations. *Journal of Computational Physics*, 151(2):881 – 909.

[51] Ibanes, M., García-Ojalvo, J., Toral, R., and Sancho, J. M. (2000). Dynamics and scaling of noise-induced domain growth. *The European Physical Journal B-Condensed Matter and Complex Systems*, 18(4):663–673.

[52] Jánosi, I. M., Tél, T., Wolf, D. E., and Gallas, J. A. C. (1997). Chaotic particle dynamics in viscous flows: The three-particle stokeslet problem. *Phys. Rev. E*, 56:2858–2868.

[53] Jeffery, G. B. (1922). The motion of ellipsoidal particles immersed in a viscous fluid. *Proceedings of the Royal Society of London A: Mathematical, Physical and Engineering Sciences*, 102:161–179.

[54] Jung, C., Tél, T., and Ziemniak, E. (1993). Application of scattering chaos to particle transport in a hydrodynamical flow. *Chaos: An Interdisciplinary Journal of Nonlinear Science*, 3:555–568.

[55] Jung, C. and Ziemniak, E. (1992). Hamiltonian scattering chaos in a hydrodynamical system. *Journal of Physics A: Mathematical and General*, 25:3929.

[56] Kao, S., Cox, R., and Mason, S. (1977). Streamlines around single spheres and trajectories of pairs of spheres in two-dimensional creeping flows. *Chemical Engineering Science*, 32(12):1505 – 1515.

[57] Kawakami, A. and Funakoshi, M. (1999). Chaotic motion of fluid particles around a rotating elliptic vortex in a linear shear flow. *Fluid Dynamics Research*, 25(4):167–193.

[58] Krishnamurthy, D. and Subramanian, G. (2018a). Heat or mass transport from drops in shearing flows. part 1. the open-streamline regime. *Journal of Fluid Mechanics*, 850:439–483.

[59] Krishnamurthy, D. and Subramanian, G. (2018b). Heat or mass transport from drops in shearing flows. part 2. inertial effects on transport. *Journal of Fluid Mechanics*, 850:484–524.

[60] Kumar, A. (2004). Isotropic finite-differences. *Journal of Computational Physics*, 201(1):109–118.

[61] Kushch, V. (1997). Microstresses and effective elastic moduli of a solid reinforced by periodically distributed spheroidal particles. *International Journal of Solids and Structures*, 34(11):1353 – 1366.

[62] Kushch, V. (1998). Elastic equilibrium of a medium containing a finite number of arbitrarily oriented spheroidal inclusions. *International Journal of Solids and Structures*, 35(12):1187 – 1198.

[63] Kushch, V. (2013). *Micromechanics of Composites: Multipole Expansion Approach.* Elsevier Science.

[64] Landau, L. D. and Lifshits, E. M. (1959). *Fluid Mechanics: Transl. from the Russian by JB Sykes and WH Reid.* Addison-Wesley.

[65] Lau, Y.-T., Finn, J. M., and Ott, E. (1991). Fractal dimension in nonhyperbolic chaotic scattering. *Phys. Rev. Lett.*, 66:978–981.

[66] Lauricella, M., Pontrelli, G., Pisignano, D., and Succi, S. (2015). Nonlinear langevin model for the early-stage dynamics of electrospinning jets. *Molecular Physics*, 113(17-18):2435–2441.

[67] Leal, L. G. and Hinch, E. J. (1971). The effect of weak brownian rotations on particles in shear flow. *Journal of Fluid Mechanics*, 46(4):685–703.

[68] Li, C., Thomases, B., and Guy, R. D. (2019). Orientation dependent elastic stress concentration at tips of slender objects translating in viscoelastic fluids. *Phys. Rev. Fluids*, 4:031301.

[69] Liszka, T. (1984). An interpolation method for an irregular net of nodes. *International Journal for Numerical Methods in Engineering*, 20(9):1599–1612.

[70] Madenci, E., Barut, A., and Dorduncu, M. (2019a). *Peridynamic differential operator for numerical analysis.* Springer.

[71] Madenci, E., Barut, A., and Futch, M. (2016). Peridynamic differential operator and its applications. *Computer Methods in Applied Mechanics and Engineering*, 304:408–451.

[72] Madenci, E., Dorduncu, M., Barut, A., and Futch, M. (2017). Numerical solution of linear and nonlinear partial differential equations using the peridynamic differential operator. *Numerical Methods for Partial Differential Equations*, 33(5):1726–1753.

[73] Madenci, E., Dorduncu, M., and Gu, X. (2019b). Peridynamic least squares minimization. *Computer Methods in Applied Mechanics and Engineering*, 348:846 – 874.

[74] Mahan Raj Banerjee, R. R. and Ansumali, S. (2020). Discrete differential operators on a class of lattices. *Journal of Computational Science*, 44:101172.

[75] Marath, N. K., Dwivedi, R., and Subramanian, G. (2017). An orientational order transition in a sheared suspension of anisotropic particles. *Journal of Fluid Mechanics*, 811:R3.

[76] Marath, N. K. and Subramanian, G. (2017). The effect of inertia on the time period of rotation of an anisotropic particle in simple shear flow. *Journal of Fluid Mechanics*, 830:165–210.

[77] Marath, N. K. and Subramanian, G. (2018). The inertial orientation dynamics of anisotropic particles in planar linear flows. *Journal of Fluid Mechanics*, 844:357–402.

[78] Milner, S. T. (1993). Dynamical theory of concentration fluctuations in polymer solutions under shear. *Phys. Rev. E*, 48(5):3674.

[79] Mishra, S., Baskaran, A., and Marchetti, M. C. (2010). Fluctuations and pattern formation in self-propelled particles. *Phys. Rev. E*, 81(6):061916.

[80] Mudigere, D., Sherlekar, S. D., and Ansumali, S. (2014). Delayed difference scheme for large scale scientific simulations. *Phys. Rev. Lett.*, 113:218701.

[81] Namburi, M., Krithivasan, S., and Ansumali, S. (2016). Crystallographic lattice boltzmann method. *Scientific reports*, 6:27172.

[82] Noid, D. W., Gray, S. K., and Rice, S. A. (1986). Fractal behavior in classical collisional energy transfer. *The Journal of Chemical Physics*, 84(5):2649–2652.

[83] Oono, Y. and Puri, S. (1987). Computationally efficient modeling of ordering of quenched phases. *Phys. Rev. Lett.*, 58(8):836–839.

[84] Oono, Y. and Puri, S. (1988). Study of phase-separation dynamics by use of cell dynamical systems. i. modeling. *Phys. Rev. A*, 38(1):434.

[85] Petersen, D. P. and Middleton, D. (1962). Sampling and reconstruction of wave-number-limited functions in n-dimensional euclidean spaces. *Information and Control*, 5(4):279 – 323.

[86] Petschek, R. G. and Metiu, H. (1983). A computer simulation of the time-dependent ginzburg–landau model for spinodal decomposition. *The Journal of chemical physics*, 79(7):3443–3456.

[87] Poe, G. and Acrivos, A. (1976). Closed streamline flows past small rotating particles: Heat transfer at high péclet numbers. *International Journal of Multiphase Flow*, 2(4):365 – 377.

[88] Powell, R. (1983). External and internal streamlines and deformation of drops in linear two-dimensional flows. *Journal of Colloid and Interface Science*, 95(1):148 – 162.

[89] Privman, V. (1992). Fluctuating interfaces, surface tension, and capillary waves: an introduction. *Int. J. Mod. Phys. C*, 3(05):857–877.

[90] Ramadugu, R., Thampi, S. P., Adhikari, R., Succi, S., and Ansumali, S. (2013). Lattice differential operators for computational physics. *Europhys. Lett.*, 101(5):50006.

[91] Rogers, T. M., Elder, K. R., and Desai, R. C. (1988). Numerical study of the late stages of spinodal decomposition. *Phys. Rev. B*, 37(16):9638.

[92] Rom-Kedar, V., Leonard, A., and Wiggins, S. (1990). An analytical study of transport, mixing and chaos in an unsteady vortical flow. *Journal of Fluid Mechanics*, 214:347–394.

[93] Schneider, T. M., Eckhardt, B., and Yorke, J. A. (2007). Turbulence transition and the edge of chaos in pipe flow. *Phys. Rev. Lett.*, 99:034502.

[94] Segrè, P. N., Behrend, O. P., and Pusey, P. N. (1995). Short-time brownian motion in colloidal suspensions: Experiment and simulation. *Phys. Rev. E*, 52(5):5070.

[95] Shapeev, A. and Lin, P. (2009). An asymptotic fitting finite element method with exponential mesh refinement for accurate computation of corner eddies in viscous flows. *SIAM Journal on Scientific Computing*, 31(3):1874–1900.

[96] Shinozaki, A. and Oono, Y. (1993). Spinodal decomposition in 3-space. *Phys. Rev. E*, 48(4):2622.

[97] Sides, S. W., Grest, G. S., and Lacasse, M. D. (1999). Capillary waves at liquid-vapor interfaces: A molecular dynamics simulation. *Phys. Rev. E*, 60(6):6708.

[98] Skufca, J. D., Yorke, J. A., and Eckhardt, B. (2006). Edge of chaos in a parallel shear flow. *Phys. Rev. Lett.*, 96:174101.

[99] Stone, H. A. and Kim, S. (2001). Microfluidics: basic issues, applications, and challenges. *AIChE J.*, 47(6):1250–1254.

[100] Subramanian, G. and Brady, J. F. (2006). Trajectory analysis for non-brownian inertial suspensions in simple shear flow. *Journal of Fluid Mechanics*, 559:151–203.

[101] Subramanian, G. and Koch, D. L. (2005). Inertial effects on fibre motion in simple shear flow. *Journal of Fluid Mechanics*, 535:383–414.

[102] Subramanian, G. and Koch, D. L. (2006a). Centrifugal forces alter streamline topology and greatly enhance the rate of heat and mass transfer from neutrally buoyant particles to a shear flow. *Phys. Rev. Lett.*, 96:134503.

[103] Subramanian, G. and Koch, D. L. (2006b). Inertial effects on the orientation of nearly spherical particles in simple shear flow. *Journal of Fluid Mechanics*, 557:257–296.

[104] Subramanian, G. and Koch, D. L. (2006c). Inertial effects on the transfer of heat or mass from neutrally buoyant spheres in a steady linear velocity field. *Physics of Fluids*, 18(7):073302.

[105] Tanaka, H. and Araki, T. (1998). Spontaneous double phase separation induced by rapid hydrodynamic coarsening in two-dimensional fluid mixtures. *Phys. Rev. Lett.*, 81(2):389.

[106] Thampi, S. P., Ansumali, S., Adhikari, R., and Succi, S. (2013). Isotropic discrete laplacian operators from lattice hydrodynamics. *J. Comput. Phys.*, 234:1–7.

[107] Thampi, S. P., Pagonabarraga, I., and Adhikari, R. (2011). Lattice-boltzmann-langevin simulations of binary mixtures. *Phys. Rev. E*, 84(4):046709.

[108] Torza, S., Henry, C., Cox, R., and Mason, S. (1971). Particle motions in sheared suspensions. xxvi. streamlines in and around liquid drops. *Journal of Colloid and Interface Science*, 35(4):529 – 543.

[109] Wiggins, S. (2003). *Introduction to applied nonlinear dynamical systems and chaos*, volume 2. Springer Science & Business Media.

[110] Wignall, G. D. and Egelstaff, P. A. (1968). Critical opalescence in binary liquid metal mixtures i. temperature dependence. *J. Phys. C: Solid State Phys.*, 1(4):1088.

[111] Wu, X. L., Pine, D. J., and Dixon, P. K. (1991). Enhanced concentration fluctuations in polymer solutions under shear flow. *Phys. Rev. Lett.*, 66(18):2408.

[112] Yang, S., Kim, J. Y., Lee, S. J., Lee, S. S., and Kim, J. M. (2011). Sheathless elasto-inertial particle focusing and continuous separation in a straight rectangular microchannel. *Lab Chip*, 11:266–273.

[113] Yudistiawan, W. P., Ansumali, S., and Karlin, I. V. (2008). Hydrodynamics beyond navier-stokes: The slip flow model. *Phys. Rev. E*, 78:016705.

[114] Ziemniak, E., Jung, C., and Tél, T. (1994). Tracer dynamics in open hydrodynamical flows as chaotic scattering. *Physica D: Nonlinear Phenomena*, 76:123 – 146.

[115] Zwanzig, R. (2001). *Nonequilibrium statistical mechanics.* Oxford University Press.

Appendix A

Structure factor of the Cahn-Hilliard-Cook equation

The CHC equation (6.9) through the Fourier-Laplace transform may be represented as:

$$\begin{aligned} I\,\omega\phi(\boldsymbol{q}) &= -q^2\,M(A+q^2\,K)\phi(\boldsymbol{q}) + I\,\boldsymbol{q}\cdot\boldsymbol{\xi}(\boldsymbol{q}) \qquad \text{(A.1)} \\ \Rightarrow \phi(\boldsymbol{q}) &= \frac{I\,\boldsymbol{q}\cdot\boldsymbol{\xi}(\boldsymbol{q})}{I\,\omega + q^2\,M(A+q^2\,K)}. \qquad \text{(A.2)} \end{aligned}$$

The structure factor can be obtained as,

$$\begin{aligned} \langle\phi(\boldsymbol{q})\phi^*(\boldsymbol{q})\rangle &= \frac{1}{2\pi}\int_{-\infty}^{\infty}\frac{q^2}{\omega^2+q^4\,M^2(A+q^2\,K)^2}\boldsymbol{\xi}\boldsymbol{\xi}^*\,d\omega \qquad \text{(A.3)} \\ &= \frac{k_BT}{A+q^2\,K}, \qquad \text{(A.4)} \end{aligned}$$

where, we have made use of the Gaussian statistics if the noise term, i.e. in Fourier space $\langle\boldsymbol{\xi}\boldsymbol{\xi}^*\rangle = 2\,k_BT\,M$. Similarly, in the discrete Fourier space one could write the analog of (A.1) as,

$$\begin{aligned} I\omega\phi(\boldsymbol{q}) &= \tilde{\nabla}^2_{\boldsymbol{q}}\,M(A+\tilde{\nabla}^2_{\boldsymbol{q}}\,K)\phi(\boldsymbol{q}) + \tilde{\boldsymbol{\nabla}}_{\boldsymbol{q}}\cdot\boldsymbol{\xi}(\boldsymbol{q}) \qquad \text{(A.5)} \\ \Rightarrow \phi(\boldsymbol{q}) &= \frac{\tilde{\boldsymbol{\nabla}}_{\boldsymbol{q}}\cdot\boldsymbol{\xi}(\boldsymbol{q})}{I\,\omega+\tilde{\nabla}^2_{\boldsymbol{q}}\,M(A+\tilde{\nabla}^2_{\boldsymbol{q}}\,K)}, \qquad \text{(A.6)} \end{aligned}$$

where, $\tilde{\boldsymbol{\nabla}}_{\boldsymbol{q}}$ represents the discrete Fourier presentation of the discrete gradient operator. Following the definition (A.3), one could show that the discrete structure factor may be obtained in the following form:

$$\langle\phi(\boldsymbol{q})\phi^*(\boldsymbol{q})\rangle = \left(\frac{\tilde{\boldsymbol{\nabla}}_{\boldsymbol{q}}\cdot\tilde{\boldsymbol{\nabla}}_{\boldsymbol{q}}}{\tilde{\nabla}^2_{\boldsymbol{q}}}\right)\frac{k_BT}{A-K\tilde{\nabla}^2_{\boldsymbol{q}}}, \qquad \text{(A.7)}$$

Appendix B

BCC lattice operators

The BCC scheme for derivative in the x-direction may be written on a RD2Q9 grid with $\delta x = \delta y$, following Table- 7.2 as:

$$\begin{aligned}\tilde{\partial}_x \phi_{i,j} = \quad & \tfrac{1}{4\delta x}\left[\tfrac{1}{6}\left(\phi_{i+1,j} - \phi_{i-1,j}\right) - \tfrac{1}{4}\left(\phi_{i+1,j+1} + \phi_{i+1,j-1} - \phi_{i-1,j+1} - \phi_{i-1,j-1}\right)\right. \\ & \left. + \tfrac{7}{3}\left(\phi_{i+1/2,j+1/2} + \phi_{i+1/2,j-1/2} - \phi_{i-1/2,j+1/2} - \phi_{i-1/2,j-1/2}\right)\right]\end{aligned} \tag{B.1}$$

The scalar field ϕ can be represented in the discrete Fourier space as $\phi_{i,j} = \hat{\phi}\exp[I\delta x(i\,q_x + j\,q_y)]$, where q_x and q_y are the wave vectors in the x and y directions, respectively. Then (B.1) can be written in the discrete Fourier space as,

$$\tilde{\partial}_x \hat{\phi} = \frac{1}{\delta x}\left[\frac{7}{3} I \sin\left(\frac{\delta x q_x}{2}\right)\cos\left(\frac{\delta x q_y}{2}\right) - \frac{1}{4} I \sin(\delta x q_x)\cos(\delta x q_y) + \frac{1}{12} I \sin(\delta x q_x)\right]\hat{\phi}. \tag{B.2}$$

Similarly, for the y-derivative it can be shown that,

$$\tilde{\partial}_y \hat{\phi} = \frac{1}{\delta x}\left[\frac{7}{3} I \sin\left(\frac{\delta x q_y}{2}\right)\cos\left(\frac{\delta x q_x}{2}\right) - \frac{1}{4} I \sin(\delta x q_y)\cos(\delta x q_x) + \frac{1}{12} I \sin(\delta x q_y)\right]\hat{\phi}. \tag{B.3}$$

Using (B.2) and (B.3) one may write the Laplacian in the discrete Fourier space in the following form,

$$\begin{aligned}\tilde{\Delta}^{\text{iso}}\hat{\phi} = \quad & \frac{1}{288\delta x^2}\left\{112\cos\left(\frac{\delta x q_x}{2}\right)\left(\cos(\delta x q_x)\cos\left(\frac{\delta x q_y}{2}\right)\right.\right. \\ & \left. + (2 - 3\cos(\delta x q_x))\cos\left(\frac{3\delta x q_y}{2}\right)\right) \\ & + \cos(2\delta x q_x)(9\cos(2\delta x q_y) + 1) + 12\cos(\delta x q_x)\sin^2(\delta x q_y) \\ & \left. + 4\cos(\delta x q_y)\left(3\sin^2(\delta x q_x) + 196\cos(\delta x q_x)\right) + \cos(2\delta x q_y) - 795\right\}\hat{\phi}.\end{aligned} \tag{B.4}$$

Then, the leading order error in (B.4) would be,

$$\tilde{\Delta}^{\text{iso}}(q_x, q_y) = -q^2 + \frac{1}{24} q^4 \delta x^2 + \mathcal{O}(\delta x^4). \tag{B.5}$$